

SWISS FEDERAL INSTITUTE OF TECHNOLOGY ZURICH

# Geomagnetic Secular Variation during the 19th Century

Bryan Grob

**Master Thesis**

Supervisor: Dr. Christopher C. Finlay

Institute of Geophysics  
Department of Earth Sciences

Zurich, December 2011

SWISS FEDERAL INSTITUTE OF TECHNOLOGY ZURICH

## *Abstract*

Institute of Geophysics  
Department of Earth Sciences

The Earth's magnetic field strength was first measured by Carl Friedrich Gauss in 1832 and has been repeatedly measured since then, showing a relative decay of about 10% over the last 150 years. In this thesis new time-dependent models of the geomagnetic field spanning the epoch 1790 – 1910 are constructed. Data sets previously not included in time-dependent geomagnetic field models, in particular the Maury Collection and the London/Paris declination/inclination time series are considered. The major novel aspect is the use of relative intensity data in a self – consistent manner. Relative intensity data sets are collated and checked in detail. It was found that the data in the RHF data set (relative horizontal intensity data measured in French units, as given by Jonkers *et al.* [2003]) are not relative horizontal but relative total intensity data instead. The theory for including this type of data is developed, implemented and the new software successfully benchmarked. A series of new field models including relative intensity data are presented. The decay of the axial dipole prior to 1840 is reconsidered using the new models. It is concluded that a hypothesis involving no change of the axial dipole between 1790 and 1840 is preferred to continued rapid decay both by the relative intensity data and also an independent archeomagnetic data set.

## *Acknowledgements*

I am indebted to Chris Finlay, my supervisor. With his enthusiasm and broad knowledge he was an inspiring supervisor, always having time for spontaneous discussions, exchange of ideas or tedious debugging sessions. His guidance and his many suggestions added much value to the present thesis. His efforts in proof reading are particularly appreciated.

Further I want to thank Sanja Panovska for interesting discussions and René Lobsiger for his generous technical support and sharing of his knowledge about databases.

Last but not least, many thanks to Stefan Alig for his friendship and my to fiancé Caroline for her continuous encouragement, support and love.

# Contents

<b>Abstract</b>	<b>i</b>
<b>Acknowledgements</b>	<b>ii</b>
<b>1 Introduction</b>	<b>1</b>
1.1 Observation of the geomagnetic field . . . . .	1
1.2 Spatial structure of the geomagnetic field . . . . .	2
1.3 Relative intensity observations . . . . .	3
1.4 Temporal changes and origin of the geomagnetic field . . . . .	4
1.5 State of research and the evolution of geomagnetic axial dipole component $g_1^0$ . .	5
1.6 Statement of thesis aims . . . . .	7
<b>2 Data</b>	<b>8</b>
2.1 Data sets . . . . .	8
2.1.1 Absolute observations from previous studies . . . . .	8
2.1.1.1 Maritime data sets . . . . .	8
2.1.1.2 Observatory data sets . . . . .	11
2.1.1.3 Magnetic survey data sets . . . . .	12
2.1.1.4 Archeomagnetic data set . . . . .	13
2.1.2 Relative intensity data sets . . . . .	13
2.1.2.1 Analysis methodology . . . . .	14
2.1.2.2 Relative horizontal intensity in French units (RHF) . . . . .	15
2.1.2.3 Relative total intensity in French units (RTF) . . . . .	17
2.1.2.4 Relative total intensity in Erman units (RTE) . . . . .	18
2.1.2.5 Relative total intensity in London units (RTL) . . . . .	20
2.1.2.6 Relative total intensity in De Rossel units (RTR) . . . . .	22
2.1.2.7 Relative total intensity in Humboldt units (RTH) . . . . .	23
2.2 Error assignment . . . . .	25
2.2.1 Errors assignment to $D$ , $I$ , $H$ and $F$ . . . . .	25
2.2.2 Errors assignment to relative intensity observations . . . . .	26
2.2.3 Summary of recommendations concerning use of relative intensity data . .	29
<b>3 Methodology</b>	<b>31</b>
3.1 Core field modeling . . . . .	31
3.1.1 Governing equations . . . . .	31
3.1.2 Representation of the time-dependence: B-Splines . . . . .	32

3.1.3	Geomagnetic observables . . . . .	34
3.2	Regularised inversion . . . . .	35
3.2.1	General considerations . . . . .	35
3.2.2	Inverse methodology . . . . .	36
3.3	Extension of the standard formalism . . . . .	38
3.3.1	Implementation of relative intensity observations . . . . .	38
3.4	Modelling assumptions . . . . .	39
<b>4</b>	<b>Results</b>	<b>40</b>
4.1	19th century models not including relative intensity observations in inversions . .	41
4.1.1	Basic model without Maury Collection . . . . .	41
4.1.2	Basic model with Maury Collection . . . . .	46
4.2	Further analysis of the Maury Collection . . . . .	47
4.2.1	Comparisons with <i>gufm1</i> . . . . .	47
4.2.2	Effect of Maury Collection on secular variation time series . . . . .	49
4.3	19th century models including relative intensity observations in inversions . . . .	51
4.3.1	Models with linear constraint on the evolution of $g_1^0(t)$ . . . . .	51
4.3.2	Models without linear constraint on the evolution of $g_1^0(t)$ . . . . .	52
4.3.3	Comparison of models to data sets included in inversions . . . . .	55
<b>5</b>	<b>Discussion and Conclusions</b>	<b>56</b>
5.1	New 19th century field models . . . . .	56
5.2	Inclusion of relative intensity observations . . . . .	59
5.2.1	Data sets . . . . .	59
5.2.2	Comparisons to previous models of $g_1^0(t)$ . . . . .	60
5.2.3	Comparison with the independent archeomagnetic data set of Donadini <i>et al.</i> [2006] . . . . .	62
5.3	Conclusions . . . . .	64
5.4	Recommendations for future historical field models . . . . .	65
	<b>Bibliography</b>	<b>66</b>

# Chapter 1

## Introduction

### 1.1 Observation of the geomagnetic field

Observations of the geomagnetic field extend back thousands of years and are strongly linked to mans exploration of the Earth. The earliest known compass surfaced in China by at least the first century and the first documented observations date back to 720 and were made by Yi-Xing, using a spoon-shaped device made out of loadstone (i.e. magnetite) [Needham, 1962]. As pointed out by Backus *et al.* [1996], the use of the magnetic field for navigation cannot be unambiguously identified until 1088 in China and nearly 100 years later in Europe.

In 1600 William Gilbert published *De Magnete*, the first comprehensive work on geomagnetism, in which he declared "*Magnus magnes ipse est globus terrestris*" (i.e. the whole Earth itself is a great magnet). Interestingly, the publication date coincides with the time the English were preparing to meet the Spanish Armada, reinforcing the importance of geomagnetic studies navigational purposes. By the year 1701 the first magnetic chart, covering the Atlantic Ocean, was produced by Edmund Halley [Halley, 1701]. This was derived from measurements he made during voyages in the Atlantic ocean; inclination measurements were recorded a short time afterward. The 18th century was a time of great discoveries in geomagnetism as James Cook and especially Alexander von Humboldt, made extensive magnetic observations of declination, inclination, and relative intensity (see section 1.3 and Chapter 2 for a detailed discussion) during their geographically diverse expeditions.

It was not until 1832, when Carl Friedrich Gauss devised a extension of the relative intensity measurement procedure, that it became possible to record the field's total intensity (cf. Garland [1979], Malin [1982] or Malin & Bullard [1982]). In addition, Gauss led efforts to set up a global system of magnetic observatories, the descendants of which run up to the present day. In the same year, Gauss developed spherical harmonic analysis, a powerful mathematical tool enabling the separation of internal and external parts of the geomagnetic field. See Garland [1979] for a comprehensive summary of Gauss' contributions to geomagnetism.

Geomagnetic observations consist of one of seven possible components typically used to describe Earth's magnetic field. These are illustrated in Figure 1.1. Considering a local Cartesian coordinate system, the geomagnetic vector field  $\mathbf{B}$  can be decomposed into its three orthogonal components  $X = -B_\theta$ , in the direction of geographic north  $N$ ,  $Y = B_\phi$ , in the direction of geographic east  $E$ , and  $Z = -B_r$ , in the vertical direction. When combined together these yield the total intensity  $F = \sqrt{X^2 + Y^2 + Z^2}$ . The combination of  $X$  and  $Y$  also describes a quantity called horizontal intensity  $H = \sqrt{X^2 + Y^2}$ . The angle between the horizontal intensity  $H$  and true geographic north  $N$  is called declination ( $D$ ), where  $D = \arctan(Y/X)$ . The angular difference between total intensity  $F$  and  $H$  is referred to as inclination ( $I$ ) with  $I = \arctan(Z/H)$ .

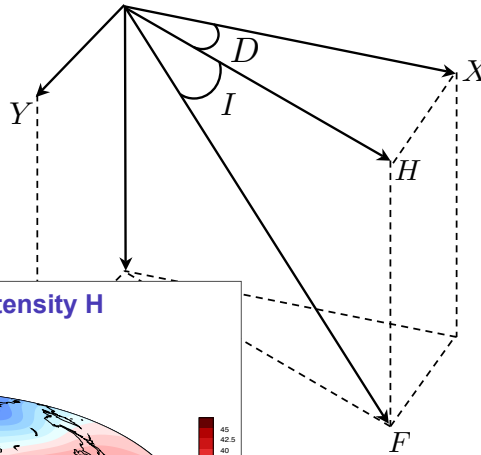


Figure 1.1: Geomagnetic components as defined on a local Cartesian coordinates system

## 1.2 Spatial structure of the geomagnetic field

The spatial structure of the geomagnetic main field (i.e. the core generated field) at the Earth's surface is characterised by very distinct features. Figure 1.2 shows maps of the total (left) and horizontal intensity (right) for the epoch 2010 as given by the IGRF-11 model. The morphology

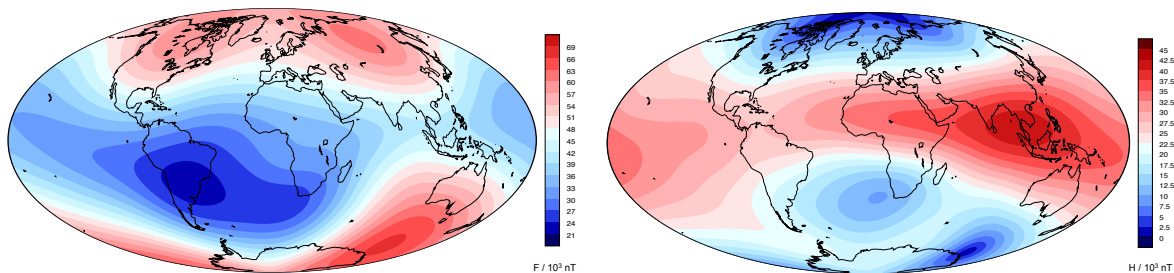


Figure 1.2: Scalar field intensity  $F$  (left) and scalar field intensity  $H$  (right) at Earth's surface in 2010.0 as given by the IGRF-11 model. Contour interval  $2.5 \mu\text{T}$

differs very much from that expected from a simple axial dipole as such a field would imply maxima at the geographic poles. In particular, the total intensity increases towards the poles

and shows flux lobes of high intensity at high latitudes in the northern as well as in the southern hemisphere. A further remarkable feature is the region of distinct low intensity in the South-Atlantic, known as the South-Atlantic Anomaly. The horizontal field is generally weaker than the total intensity and decreases towards the poles. A region of particular high horizontal intensity is located in South-East Asia.

### 1.3 Relative intensity observations

One possible method of obtaining fresh insight into the pre-1840 evolution of the geomagnetic dipole is by using direct relative intensity measurements. The period of oscillation of a magnetic needle swinging in the horizontal plane in an instrument known as dip-circle (see Figure 1.3) was known to be inversely proportional to the square root of the intensity of the magnetic field (the mathematical details are given in the next subsection). Therefore measuring the oscillation

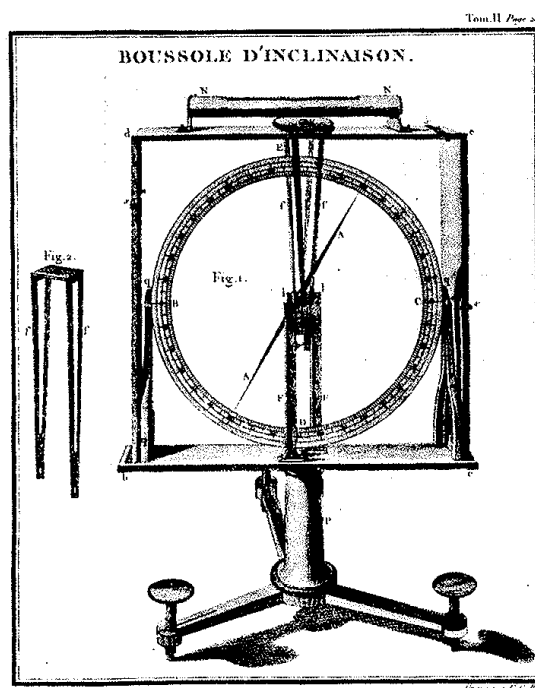


Figure 1.3: Illustration of the dip-circle used on the expedition under Bunny Dentrecasteaux (1791 – 1794), as reported by De Rossel [1808]. This instrument was used for observations of relative intensity. Reproduced from De Rossel [1808]

time and comparing it to that measured at a fixed reference site, the relative change in intensity with respect to the reference site could be calculated. An intensity value of  $F = 1.0$  and  $H = 1.0$ , respectively, was assumed for the reference site. This method was extensively used by Alexander von Humboldt and his collaborators on various expeditions around the globe in the late 18th and early 19th century.

The relation between the period  $T$  and intensity  $F$  is given by

$$T(r, \theta, \phi, t) = 2\pi \sqrt{\frac{I}{mF(r, \theta, \phi, t) + C}}, \quad (1.1)$$

where  $I$  is the moment of inertia of the suspended system about its axis,  $m$  is the magnetic moment of the magnet, and  $C$  is the restoring couple due to the elastic suspension. If the suspending fibre is sufficiently fine,  $C$  may be made arbitrarily small. In this case

$$mF = 4\pi^2 \frac{I}{T^2}. \quad (1.2)$$

All of the measurements made with such needles, before 1832, were relative, rather than absolute, since the quantity  $F$  could not be isolated from magnetic moment  $m$  [Garland, 1979].

By taking the ratio of the period  $T_i$  observed at location  $P(r, \theta, \phi, t)$  and  $T_{ref}$ , taken at the reference site  $P_{ref}(r', \theta', \phi', t')$ , the magnetic moment of the magnet cancels and the intensity at location  $P(r, \theta, \phi, t)$  can be expressed relative to the intensity at the reference location  $P_{ref}(r', \theta', \phi', t')$ :

$$\frac{t_{ref}}{t_i} = \frac{2\pi \sqrt{\frac{I}{mF_{ref}}}}{2\pi \sqrt{\frac{I}{mF_i}}} = \sqrt{\frac{F_i}{F_{ref}}}, \quad (1.3)$$

from which the definition of a relative intensity follows

$$\left(\frac{T_{ref}}{T_i}\right)^2 = \frac{F_i}{F_{ref}} := F_i^{r,k}, \quad (1.4)$$

where  $k$  denotes the unit in which the relative intensity is measured (see section 2.1.2).

Any relative intensity observation can thus be related to its corresponding absolute intensity  $F(r, \theta, \phi, t)$  by the relation

$$F^{r,k}(r, \theta, \phi, t) = C \cdot F(r, \theta, \phi, t), \quad (1.5)$$

and likewise for relative horizontal intensity.

## 1.4 Temporal changes and origin of the geomagnetic field

Although the geomagnetic field appears to have existed for a very long period of time, it is anything but static. Short scale temporal changes in direction and intensity of the main field (i.e. the field of internal origin) with periods of years to tens of centuries, are collectively referred

to as secular variation. William Gellibrand first discovered the change in declination with time. He achieved this by comparing measurements he took in Deptford with similar ones taken by Edmund Gunter twelve years earlier, noticing a systematic decrease in magnetic declination between 1580 and 1634 [Gellibrand, 1635]. On the basis of this study Halley produced a model for the variation in terms of dipole moving generally westward, deep within the earth, making a circuit every 700 years [Halley, 1693]. Figure 1.4 illustrates the secular variation of declination and inclination together with the model predictions of *gufm1* by Jackson *et al.* [2000].

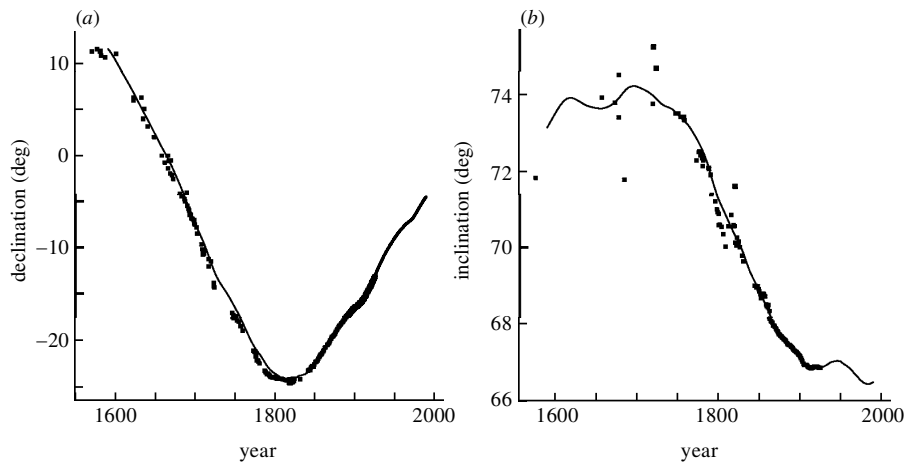


Figure 1.4: Changes of (a) declination and (b) inclination in London compared to *gufm1* of Jackson *et al.* [2000]. Figure reproduced from Jackson *et al.* [2000]

Today, secular variation is thought to be caused by distortion of toroidal and poloidal magnetic field lines, when the magnetic field is rearranged by motions at the core surface. Roberts & Scott [1965] proposed that on time scales much shorter than the magnetic diffusion time scale ( $\approx 10,000$  years for Earth's core), field evolution is primarily the result of advection. This approximation is usually referred to as the Frozen Flux Hypothesis.

## 1.5 State of research and the evolution of geomagnetic axial dipole component $g_1^0$

The earliest models were compiled in the mid-1980's, and these were not time-dependent but reduced to discrete epochs (Bloxham & Gubbins [1985]; Bloxham [1986]; Bloxham *et al.* [1989]). In 1989, Bloxham & Jackson [1989] introduced the first time-dependent model (*ufm1*). Soon afterwards a more sophisticated model (*ufm2*) followed using a larger database and in 2000 Jackson *et al.* [2000] presented *gufm1*, a state-of-the-art model for secular variation modelling at the CMB. Spanning 400 years (1590 – 1990), *gufm1* comprises data from a variety of sources, such as maritime observations, magnetic surveys, observatory measurements, and satellite data. Presently *gufm2*, an extended version of *gufm1*, is in work which uses an even larger database that includes satellite data (C. Finlay, *pers. comm.*).

Although *gufm1* is the currently most sophisticated historical field model, a serious shortcoming is that it relies only on directional observations prior to 1840. As proven by Hulot *et al.* [1997], directional observations alone provide enough information to constrain the core field morphology, but not its absolute magnitude. To overcome this problem, Bloxham & Jackson [1989], Bloxham & Jackson [1992] and Jackson *et al.* [2000] constrained the axial dipole (and thereby defined the effective magnitude of the field) by a linear extrapolation, with its starting point at 1840, using the relation

$$g_1^0(t) = g_1^0(1840) + \beta(t - 1840). \quad (1.6)$$

Employing the results of Barraclough [1974], the slope of the straight line  $\beta$  was set to  $\beta = 15.46$  nTyr<sup>-1</sup>. This value was inferred by a linear regression of 170 axial dipole values taken from single epoch models within the time interval 1829 – 1970 [Barraclough, 1974]. The assumptions made are nevertheless rather arbitrary as, firstly, there are no physical reason why the axial dipole should obey (1.6), and secondly the free parameter  $\beta$  is not well constrained prior to 1840.

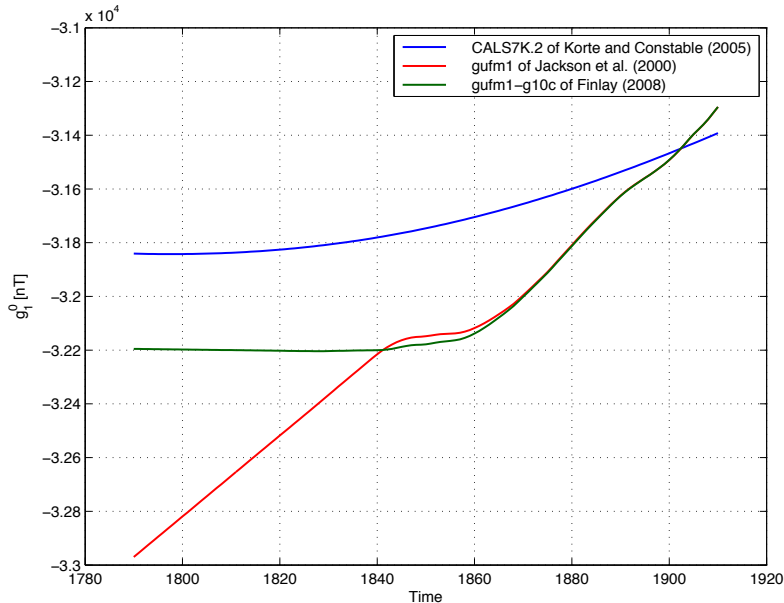


Figure 1.5: Evolution of  $g_1^0(t)$  derived from previous studies by Jackson *et al.* [2000] ( $\beta = 15$  nT/yr), Korte & Constable [2005a] and Finlay [2008] ( $\beta = 0$  nT/yr). Courtesy of C. Finlay

The Earth’s magnetic field strength was first measured by Gauss in 1832 and has been repeatedly measured since then, showing a relative decay of about 10% over the last 150 years. This decay is most apparent in the geomagnetic axial dipole component  $g_1^0(t)$ , the first Gauss coefficient, which is also the largest component of Earth’s magnetic field. Its magnitude also determines the morphology of solar-terrestrial electrical current systems [Finlay, 2008].

Recently, Gubbins *et al.* [2006] have inferred the  $g_1^0(t)$  for the period 1590 – 1840 from directional data and paleomagnetic intensity measurements. They found that the decay of the axial dipole was only approximately 15% of the value derived by Barraclough [1974]. Finlay [2008], examining a variety of possible axial dipole models, found, using Bayesian model comparison

techniques, a slope of  $\beta = 0$  to provide the most probable model. CALKS7K.2 is a geomagnetic field model by Korte & Constable [2005a] and is constructed from paleointensity and paleodirection data only and covers the past seven millennia from 5000 B.C. to 1950 A.D. The decay of  $g_1^0(t)$  according to *CALS7K.2* is much slower compared to the other field models as it lacks high resolution recent historical data.

A summary of different values of  $\beta$  used in recent studies is found in Table 1.1. The inherent problem of all mentioned studies is the lack of direct intensity observations prior to 1840.

Author(s)	Model	$\beta$ [nTyr <sup>-1</sup> ]
Jackson <i>et al.</i> [2000]	<i>gufm1</i>	15.0
Gubbins <i>et al.</i> [2006]	modified <i>gufm1</i>	2.28
Finlay [2008]	<i>gufm1-g10c</i>	0.0

Table 1.1: Summary of different slopes  $\beta$  derived from recent studies describing the decay of the axial dipole  $g_0^1(t)$  between 1590 and 1840 according to equation (1.6)

## 1.6 Statement of thesis aims

The aims of the thesis are:

- (i) Derivation of a time-dependent model of the 19th century of the geomagnetic field at the core surface
- (ii) Assessment of the Maury Collection (a large data set, consisting of more than 78,000 declination measurements) for time-dependent field modelling
- (iii) Collation and quality control of relative intensity data sets
- (iv) Development of a theory for using relative intensity data for time-dependent field modelling
- (v) Derivation of a time-dependent model of the 19th century of the geomagnetic field at the core surface including the relative intensity data sets
- (vi) Assessment of the merits of the two hypothesis concerning the rate of change of the axial dipole prior to 1840: (i) 15 nT/yr, (ii) 0 nT/yr

The thesis includes four chapters additional to this introduction. Chapter 2 describes and presents a new analysis of the relative intensity data sets, explaining how the data were selected and evaluated. The methodological approach to modelling and inverting the data is given in chapter 3. Chapter 4 presents results from the modelling and inversion, and the final chapter discusses the interpretations of the results and summarises the main findings.

# Chapter 2

## Data

### 2.1 Data sets

#### 2.1.1 Absolute observations from previous studies

The data sets carrying the data have all come from previously published sources. However, the Maury Collection and the London/Paris declination/inclination time series data sets have not previously been used in publications on time-dependent geomagnetic field modelling. Only brief comments are made here on each data set and their provenance. For more detailed information, see the cited references. 4-digit ID codes, for example 3102, refer to the ID codes of Jonkers *et al.* [2003]. Figures 2.1 and 2.2 illustrate spatial and temporal data distributions, respectively. A summary of all absolute data sets used in this thesis is given in Table 2.5, which provides information on the frequency of data type, time span, and error estimates of the particular data set.

##### 2.1.1.1 Maritime data sets

###### (a) `arch_all.cut.uniq.red` / `bn_after_rmv.uniq.red`

These data set originates from the publication of Jackson *et al.* [2003], containing solely declination measurements, predominantly between 1820 and 1850 (`arch_all.cut.uniq.red`: 1719 – 1840; `bn_after_rmv.uniq.red`: 1694 – 1867). These data originate from logbooks entries recorded by the French Navy, French trading ships and the French Hydrographic Service. Positions in the `arch_all.cut.uniq.red` data set are arranged in a  $1^\circ \times 1^\circ$  grid, those of `bn_after_rmv.uniq.red` on a  $10 \text{ min} \times 10 \text{ min}$  grid that has been transformed to geographical coordinates, introducing an additional discretisation error. Both data sets provide a good global coverage, imaging the well known trading routes around the Cape of Good Hope to the India. For more detailed information, see Jackson *et al.* [2003] and Table 2.5.

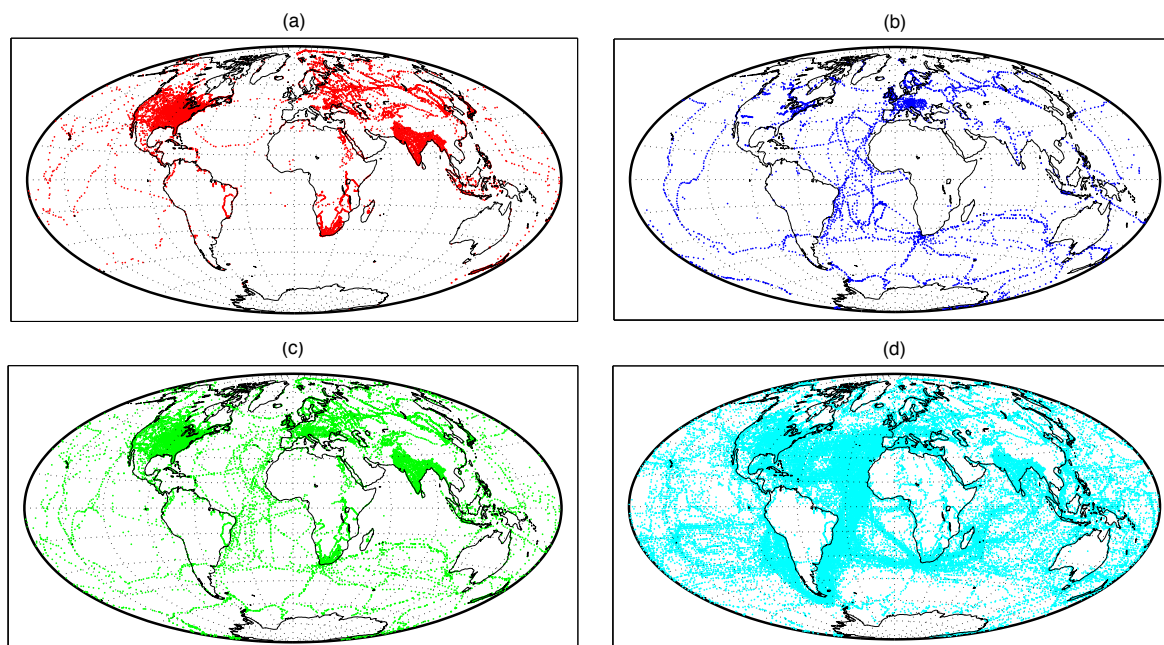


Figure 2.1: Plots of the spatial data distribution of the supplementary data sets. Note that data coverage is particularly reduced in the Atlantic ocean, South America, Africa, Australia and Antarctica. Also it is evident that the Arctic region is much better covered than the Antarctic. The majority of horizontal intensity and inclination observations are restricted to land surveys, whereas declination measurements originate mostly from maritime sources. (a) Horizontal intensity, (b) Total intensity, (c) Inclination, (d) Declination

### (b) `incl_extra.dat`

This small data set of early 68 inclination observations from (1791.5 – 1804.5) is a compilation from sources Dentrecaesteaux (3140), Vancouver (3141), Krusenstern (3158), and Finders (3202) as described in Jonkers *et al.* [2003]. Geographically the data is most abundant in the Pacific around Australia with a few data points near the west coast of the United States. For more detailed information, see Jonkers *et al.* [2003] and Table 2.5.

### (c) **Maury Collection (MC)**

This data set was compiled by Lt. Matthew Fontaine Maury (1806 – 1873). Maury, a U.S. Navy veteran, was highly interested in oceanographic parameters and let the data be recorded on abstract logs. These abstract logs were separate log sheets and were placed in front of the first page of the logbooks. Next to various parameters related to oceanography, such as temperature, pressure, currents, declination was also among the required parameters. Maury distributed logbooks with preceding abstract logs free of charge if the mariners returned the filled out abstract log. The cycle would continue as long as logs were returned.

The MC data set contains a total of 72,810 declination observations, measured both in degrees and points. The latter originates from the ships main compass, which was mounted to the ship and was not portable. There a full circle was divided into 32 regular points, making 1 point corresponding to  $11.25^\circ$ . The data originates from many areas of the world's oceans,

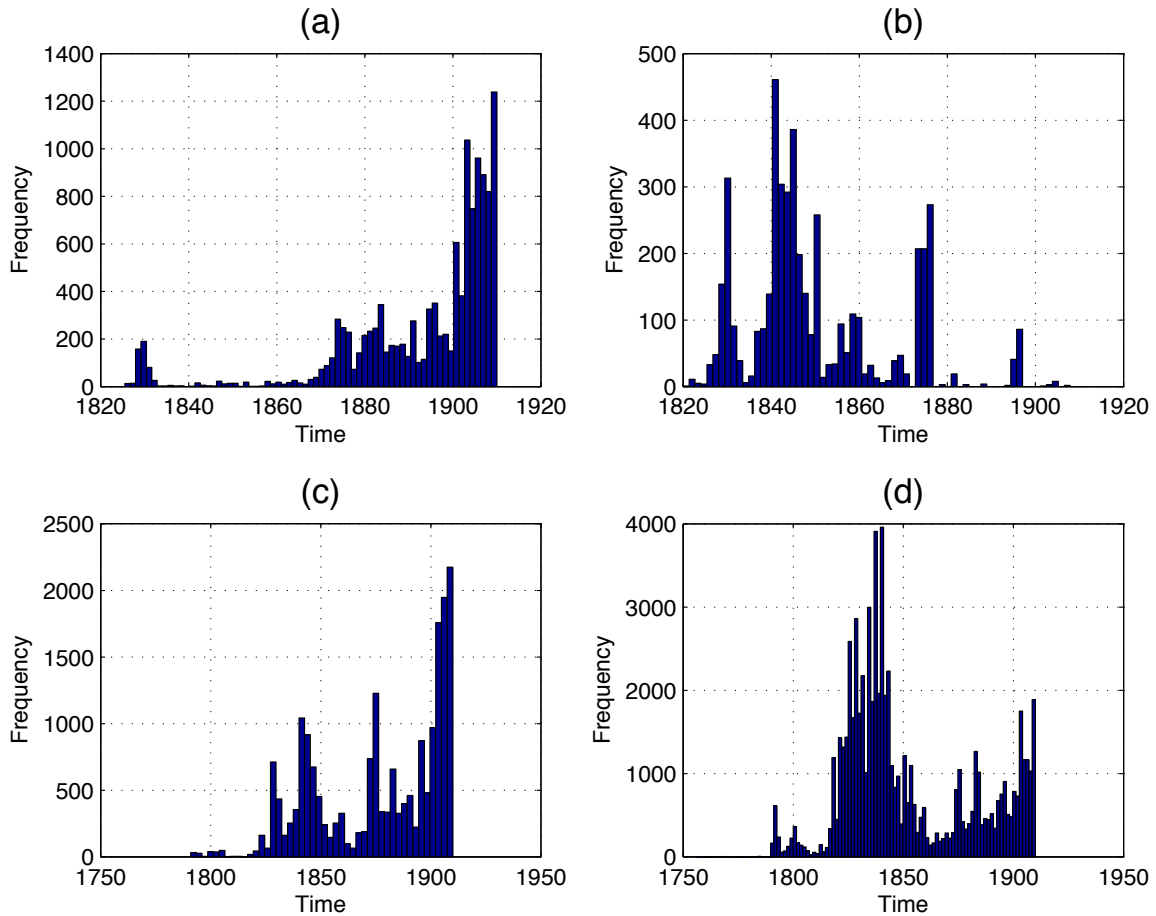


Figure 2.2: Histograms showing the temporal data distribution of (a) Horizontal intensity, (b) Total intensity, (c) Inclination, (d) Declination. Note that the pre-1840 data appearing in (a) and (b) are not relative intensity observations. Instead they are intensity data expressed in British units (an early absolute scale; cf. [Sabine, 1877] and Jonkers *et al.* [2003]), originating from the three compilations Sabine [1872], Sabine [1875] and Sabine [1877]

although confined mostly to the major trade routes, allowing the combined analysis to cover most of the globe with the exception of the polar regions. Logs were made from 1792 to 1910. Many maritime nations made contributions to the MC, although the United States, United Kingdom, Netherlands, Germany, Japan and France were the major contributors.

The source data of the MC was published and digitised by the U.S. *National Oceanic and Atmospheric Administration* (NOAA) and the *National Marine Data Information Service of the State Oceanic Administration of China* in 1993, and is part of the *Comprehensive Ocean-Atmosphere Data Set* (COADS) (> 100,000,000 records) [NOAA, 1998]. For more detailed information, see NOAA [1998] and Table 2.5.

### 2.1.1.2 Observatory data sets

#### (a) Observatory data set: `oams_2011.dif`

This data set contains annual mean data ( $X$ ,  $Y$  and  $Z$ ) coming from eleven geomagnetic observatories (operating in the 19th century) obtained from the World Data Center for Geomagnetism, Edinburgh (see Figure 2.3). The operation time of the observatories differ, mainly due to urbanisation starting in the 19th century. Observatory data are particularly useful because of the high data quality and the possibility to monitor precisely secular variation. Observatory annual means are treated using, e.g.

$$\frac{dX}{dt} = X(t) - X(t - 1). \quad (2.1)$$

This also eliminates the bias due to the unknown crustal magnetic field, because the crustal signal is assumed to be the same for both dates  $t$  and  $t - 1$  and therefore should cancel. For more detailed information, see Table 2.1.

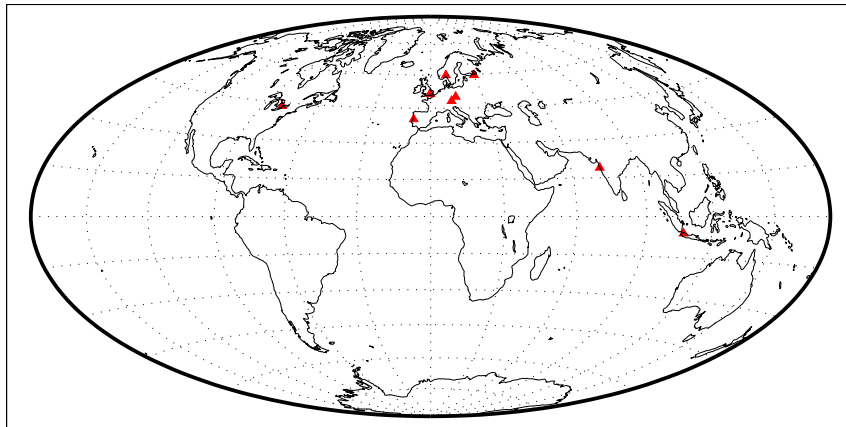


Figure 2.3: Global chart showing the locations of the magnetic observatories

#### (b) London/Paris declination/inclination time series

These four data sets represent the longest declination and inclination time series available, and are thus valuable for describing the temporal change of the geomagnetic field.

##### (i) *London declination/inclination time series:*

The times series of declination and inclination measurements from London (hereafter referred to as ‘London data set’) was compiled and published by Malin & Bullard [1982]. Originating from more than 50 observatories around London (all sites are located in a circle with radius of less than 40 km), the data set spans over 400 years of observations. The data have been reduced to a single observatory location (i.e. the observatory contributing most of the observations and having the best temporal data distribution) in order to alleviate site differences. For reasons of homogeneity, data recorded in Julian calendar have been converted to Gregorian format, and longitudes relative to Paris have been corrected to Greenwich.

Code	Name	Time span	X		Y		Z	
			$N$	$\sigma_x[nT]$	$N$	$\sigma_y[nT]$	$N$	$\sigma_z[nT]$
BTV	Jakarta	1884.5 – 1885.5	21	12.8	21	5.5	21	13.7
CLA1	Colaba 1	1846.5 – 1864.5	18	32.7	18	3.2	18	83.6
CLA2	Colaba 2	1865.5 – 1905.5	41	8.3	41	2.5	41	18.9
COI	Coimbra	1867.5 – 1909.5	42	7.1	42	4.9	43	10.0
GRW	Greenwich	1847.5 – 1909.5	61	18.2	61	8.3	47	21.3
KEW	Kew	1858.5 – 1909.5	51	5.1	51	4.0	51	13.6
MNH	Munich	1842.5 – 1909.5	45	8.1	45	3.7	42	17.3
OSL	Oslo	1844.5 – 1909.5	66	4.5	66	3.7	56	27.3
PRA	Prague	1871.5 – 1904.5	28	17.9	28	4.1	3	35.6
SLU	Slutsk	1878.5 – 1909.5	31	2.7	31	1.1	31	6.0
TOR	Toronto	1842.5 – 1898.5	51	17.8	51	3.2	52	99.1

Table 2.1: Magnetic observatories used in this thesis

*(ii) Paris declination/inclination time series:*

The data set spans over 450 years of declination and 320 years of inclination observations. The data have been reduced to the current site of Chambon-la-Forêt. However, early observations are made by many different observers at several different sites in the vicinity of Paris. The time series of declination and inclination measurements from Paris (hereafter referred to as 'Paris data set') was compiled and published by Alexandrescu *et al.* [1996].

For more detailed information, see Malin & Bullard [1982] for the London time series, Alexandrescu *et al.* [1996] for the Paris time series, Alexandrescu *et al.* [1997] for a comprehensive comparison of the London and Paris time series, and Table 2.5.

**2.1.1.3 Magnetic survey data sets****(a) survey.norpts / survh.norpts**

These two large data sets (survh.norpts (1790.5 – 1839.5), 10,514 observations; survey.norpts (1840.0 – 1910.0), 57,646 observations) have been compiled and previously used in Bloxham *et al.* [1989]. The data set survh.norpts contains pre-1840 horizontal and total intensity data, which are not relative intensity observations. Instead they are intensity data expressed in British units (an early absolute scale; cf. [Sabine, 1877] and Jonkers *et al.* [2003]), originating from the three compilations Sabine [1872], Sabine [1875] and Sabine [1877]. A large amount of the component  $F$ ,  $I$  and  $D$  data in the interval 1860 – 1900 (i.e. in data set survey.norpts) originated from two voyages of *HMS Challenger* and *SMS Gazelle*, both measuring  $F$ ,  $I$  and  $D$ . The total intensity data reported by the *SMS Gazelle*, however, may be systematically biased. According to Bloxham *et al.* [1989] the reason for this phenomenon lies in the nature of the vessel: the *SMS Gazelle* was a warship and its iron construction caused the systematic deviations. Following the

recommendation of Bloxham *et al.* [1989] the  $F$  data was therefore removed. For more detailed information, see Bloxham *et al.* [1989] and Table 2.5.

#### (b) **Vaq\_Af1880\_jb.dat**

This comprises a set of declination, inclination and intensity readings (144 in total) made in central Africa by two Portuguese scientists from 1877-1885. These observations have been previously compiled and studied by Vaquero & Trigo [2006] but were not included in the *gufm1* model (Jackson *et al.* [2000]). Note that the 49 pre-1832 horizontal intensity data are not direct observations but have been converted from relative to absolute horizontal intensity by Vaquero & Trigo [2006], assuming a proportionality constant  $\alpha = 21690$  nT. These data are of special interest as they provide data for an otherwise very poorly covered region. For more detailed information, see Vaquero & Trigo [2006] and Table 2.5.

#### 2.1.1.4 Archeomagnetic data set

##### **archeo\_int\_1550\_1850\_CONST.dat**

This data set was obtained from the archeo-magnetic data base GEOMAGIA50, set up by Donadini *et al.* [2006]. The selection was focused on absolute intensity data having as small error bars as possible. In total 16 absolute intensity measurements from 1795 – 1850 were extracted. This data set serves as an independent diagnostic data set against which the final models will be tested, and is thus not included in the inversion. For more detailed information see Donadini *et al.* [2006].

#### 2.1.2 Relative intensity data sets

As mentioned in (section 1.3), prior to Gauss' invention of a method to measure total intensity in 1832, only oscillation periods of a suspended needle could be measured. These observations were compared to a reference value. In the 19th century, however, global communication between scientists was not easily possible nor wished. Thus, depending on the scientist, different reference sites were chosen. For example, Alexander von Humboldt referred his observations to a location called Micuipampa (Cajamarca region) in Peru, since on his voyages, he noticed that at that particular point was a zone of very few oscillations [Jonkers *et al.*, 2003]. He suspected this to be the magnetic equator. In contrast, Edward Sabine, a very active Anglo-Irish researcher in geomagnetism, referenced his readings to the oscillation period in London.

The relative intensity data sets investigated come in six different units. These units refer to the intensity at each their own specific reference sites, where a value of  $F = 1.0$  or  $H = 1.0$  was assumed. Depending on the time and heritage of the observers, different reference sites were used. Alexander von Humboldt chose his reference point to be Micuipampa (Cajamarca region)

in Peru, Scandinavian researchers used Oslo and the Russians measured intensity with reference to St. Petersburg. These units were later standardised to the French unit shortly after 1800 [Jonkers *et al.*, 2003]. The different units studied here together with their reference sites and time spans are summarised in Table 2.2.

Unit	Reference site	Period applied
De Rossel	Brest	1791 – 1794
Humboldt	Micupampa	1798 – 1805
French	Paris	1798 – 1839
London	London	1826 – 1845
Erman	Portsmouth	1838 – 1846

Table 2.2: Summary of relative intensity units, their reference locations and time span

The relative intensity data aimed to use mostly originates from Jonkers *et al.* [2003] and has not been used in any previous studies. A recent single epoch study (for epoch 1835) by King [2010] used relative intensity data between 1830 and 1840, published in von Humboldt [1850] and von Humboldt [1858]. In this thesis all data from the two mentioned publications by von Humboldt are used. Relative intensity data acquisition is not yet exhaustive. A new data source is Sabine [1838], as suggested by R. Holme (*pers. comm.*). Becquerel [1840] (cf. page 320) mentions a letter from Paul de Lamanon, in which a considerable amount of additional observations from the Dentrecasteaux voyage are stated.

The difficulties that occur when dealing with different units of relative intensity are threefold:

- (i) exact location of reference point not always specified
- (ii) no information on date on which reference value was defined
- (iii) non-trivial error assignment due to lack of instrument specific information

### 2.1.2.1 Analysis methodology

In order to carry out a preliminary assessment of the relative intensity data sets, comparisons with the *gufm1* field model were carried out. Each datum of type  $q \in \{H, F\}$  was normalised by an other observation of the same data set, thereby obtaining the non-dimensional ratio  $R_o^q$ . In the same way, the ratios of relative intensities  $R_g^q$  were calculated from *gufm1*. Using these two ratios, comparisons can be made between the model and the data.

The ratios are defined as follows:

$$R_o^F = \frac{F_i^{r,k}}{F_{ref}^{r,k}}, \quad R_o^H = \frac{H_i^{r,k}}{H_{ref}^{r,k}}, \quad (2.2)$$

and

$$R_g^F = \frac{F_i^g}{F_{ref}^g}, \quad R_g^H = \frac{H_i^g}{H_{ref}^g}, \quad (2.3)$$

where  $F_i^{r,k}$  is a relative total intensity datum measured in units of  $k$ , and is  $F_{ref}^{r,k}$  an other relative total intensity datum acting as a reference value (different possibilities for choosing and calculating  $F_{ref}^{r,k}$  are discussed below).  $F_i^g$ ,  $F_{ref}^g$ ,  $H_i^g$  and  $H_{ref}^g$  denote the corresponding total and horizontal intensity predictions by *gufm1*.

Any datum (from one specific data set) can in principle act as a reference datum in equation (2.2). Choosing one specific datum (e.g. the latest observation in a data set), the accuracy of the ratios is highly dependent on the quality of that specific datum, and is thus made very susceptible to errors. Instead, summary ratios were computed by considering each relative intensity observation in turn as a reference point for all other data, i.e. the ratio of  $F_i^{r,k}$  and all remaining observations within the data set are calculated then a final ratio is then obtained by taking the average thereof. Note that the ratio of any observation to itself is set to zero. Synthetic tests have revealed this algorithm to be the robust against outliers. The summary ratios are calculated according to the following scheme:

$$R_o^F = \frac{1}{N-1} \sum_{\substack{j=1 \\ i \neq j}}^N \frac{F_i^{r,k}}{F_j^{r,k}}, \quad R_o^H = \frac{1}{N-1} \sum_{\substack{j=1 \\ i \neq j}}^N \frac{H_i^{r,k}}{H_j^{r,k}} \quad (2.4)$$

and

$$R_g^F = \frac{1}{N-1} \sum_{\substack{j=1 \\ i \neq j}}^N \frac{F_i^g}{F_j^g}, \quad R_g^H = \frac{1}{N-1} \sum_{\substack{j=1 \\ i \neq j}}^N \frac{H_i^g}{H_j^g}. \quad (2.5)$$

In order to assess the quality of the relative intensity data sets, the dimensionless residuals  $\Delta_R$  were calculated as follows:

$$\Delta_R = R_o^q - R_g^q, \quad (2.6)$$

in which  $R_r^q$  and  $R_g^q$  is the dimensionless relative intensity and absolute intensity ratio, respectively, as calculated by the equations (2.4) and (2.5).

### 2.1.2.2 Relative horizontal intensity in French units (RHF)

This data set consists of relative horizontal intensity measured in French units. The observations were made and published by Auguste-Nicolas Vaillant, captain of the ship ‘La Bonite’ (see Vaillant [1840 - 1852]), spanning 1835.5 – 1838.5 (Figure 2.4 (f)). Further details concerning the sources contributing to this data set are found in Jonkers *et al.* [2003] under the ID code 4481. The voyage started in France, circumnavigating South America, continuing across the Pacific to Manila, China, India and back to France (Figure 2.4 (a)). The relative intensity data sets are checked for biases in both space and time. In Figure 2.4 (a) the spatial distribution of the raw

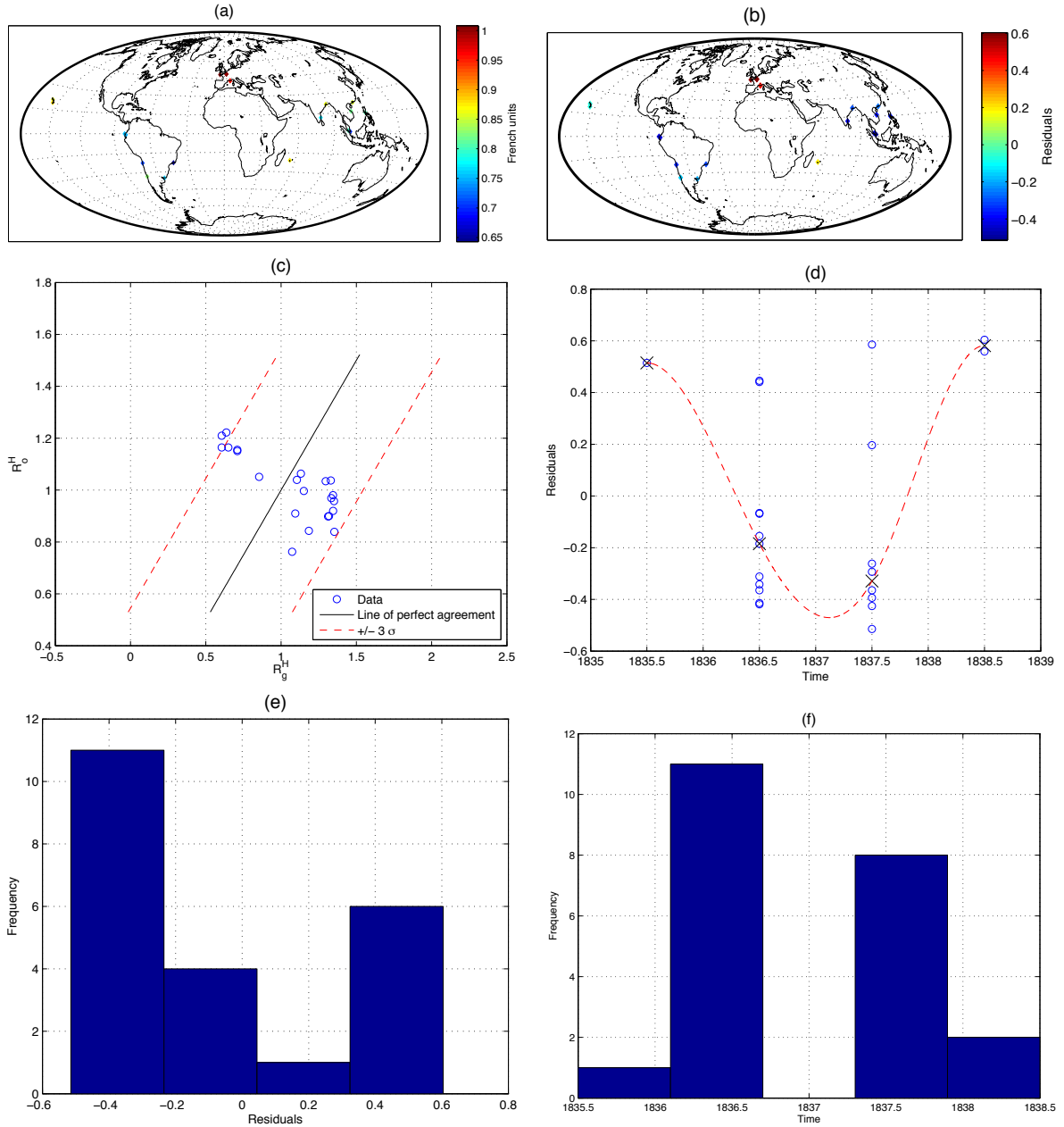


Figure 2.4: Plots of the RHF data set. (a) Spatial distribution of raw data, (b) Spatial distribution of residuals  $\Delta_R$ , (c) ratios  $R_g^H$  against  $R_o^H$ , (d) Temporal distribution of residuals  $\Delta_R$ . The X marks the median of residuals, interpolated by a least-squares fitted cubic spline (red dashed line), (e) Histogram of residuals  $\Delta_R$ , (f) Histogram showing data distribution in time

data is plotted. Note that the residuals in Figures 2.4 (b), (d) and (e) refer to the residuals as calculated by equation (2.6) and are thus dimensionless. The red dashed lines in Figure 2.4 (a) represent the interval of 3 standard deviations  $\sigma$ , whereas the the red dashed line in Figure 2.4 (d) is a least-squares fitted cubic spline, interpolating the median of residuals (marked as X).

The ratios calculated from the relative intensities show poor agreement with the ratios predicted by *gufm1* but exhibit a trend orthogonal to the linear trend in the plot of  $R_g^H$  against

$R_r^H$  - see Figure 2.4 (c). The histogram of residuals (Figure 2.4 (d)) shows a distinct left-skewed distribution with also a considerable amount of positive residuals. Positive residuals in space seem to increase towards the poles whereas an accumulation of negative residuals is noticed in the area of SE-Asia (Figure 2.4 (b) and (d)). These observations suggest that the RHF data set suffers from a systematic error in both space and time.

### 2.1.2.3 Relative total intensity in French units (RTF)

In this largest subset of relative intensity data set, the majority of the data (488 observations) were compiled and published by Henri Becquerel in 1840 (cf. Becquerel [1840]). A further 13 entries come from Sabine [1846], and the remaining readings were taken by see Vaillant [1840 - 1852]. Nine further readings by Alexander von Humboldt are in the compilation by Jonkers *et al.* [2003]. The temporal distribution of the data is shown in (Figure 2.9 (f)). As the latter observations are not reported in London units but as frequencies (see discussion of von Humboldt's data in section 2.1.2.7), the data has been added to the RTH data set. Further details concerning the sources contributing to this data set are found in Jonkers *et al.* [2003] under the ID codes 4481, 4107, 4482, 4484 and 4488. As for the above described RHF set, the reference point of these relative intensity observations is Paris, but this covers the interval 1798.09 – 1837.5. The RTF data set shows rather a good global coverage (see Figure 2.5 (a)) with dense data clusters predominantly in Europe. Further, observations along the coast of South America, the Atlantic, Pacific, the west coast of Africa and even Greenland have been made.

Among others, Christopher Hansteen, a renowned norwegian researcher in the field of geomagnetism, together with Alexander von Humboldt had noticed that intensity increased when moving from the equator to the poles. In 1707 Leonhard Euler had published a declination model, based on the assumption of a dipolar field configuration and built from maritime data collected in the Atlantic and Indian ocean, using a polynomial expansion. Using Euler's model, Hansteen failed to fit the observations he had made earlier in the Pacific, and instead found Halley's quadrupole configuration to do a good job. In 1828, Hansteen arranged a two year lasting expedition to Siberia and China with the primary goal to find the pole in Siberia [Brekke & Egeland, 2000]. On his expedition Hansteen was accompanied by Lt. Due and G. Erman. As reported by Hansteen & Due [1863], temperature corrections were applied and great attention paid to the correct determination of position.

As the readings were taken in a roughly longitudinal transect (Figures 2.6 (a) and (b)) the data gives a good indication of the changing magnetic intensity over an east-west transverse of the continent. The histogram of residuals (Figure 2.5 (e)) has its peak frequency at 0.02, the same value as found for the RHF data set, and shows a very slight right skewed residual distribution. Also, it shows a distinct deviation from the assumed underlying normal distribution of errors. Figure 2.5 (e) illustrates the accurate alignment of the data with the linear fit suggesting high quality observations. For more detailed information see Table 2.6.

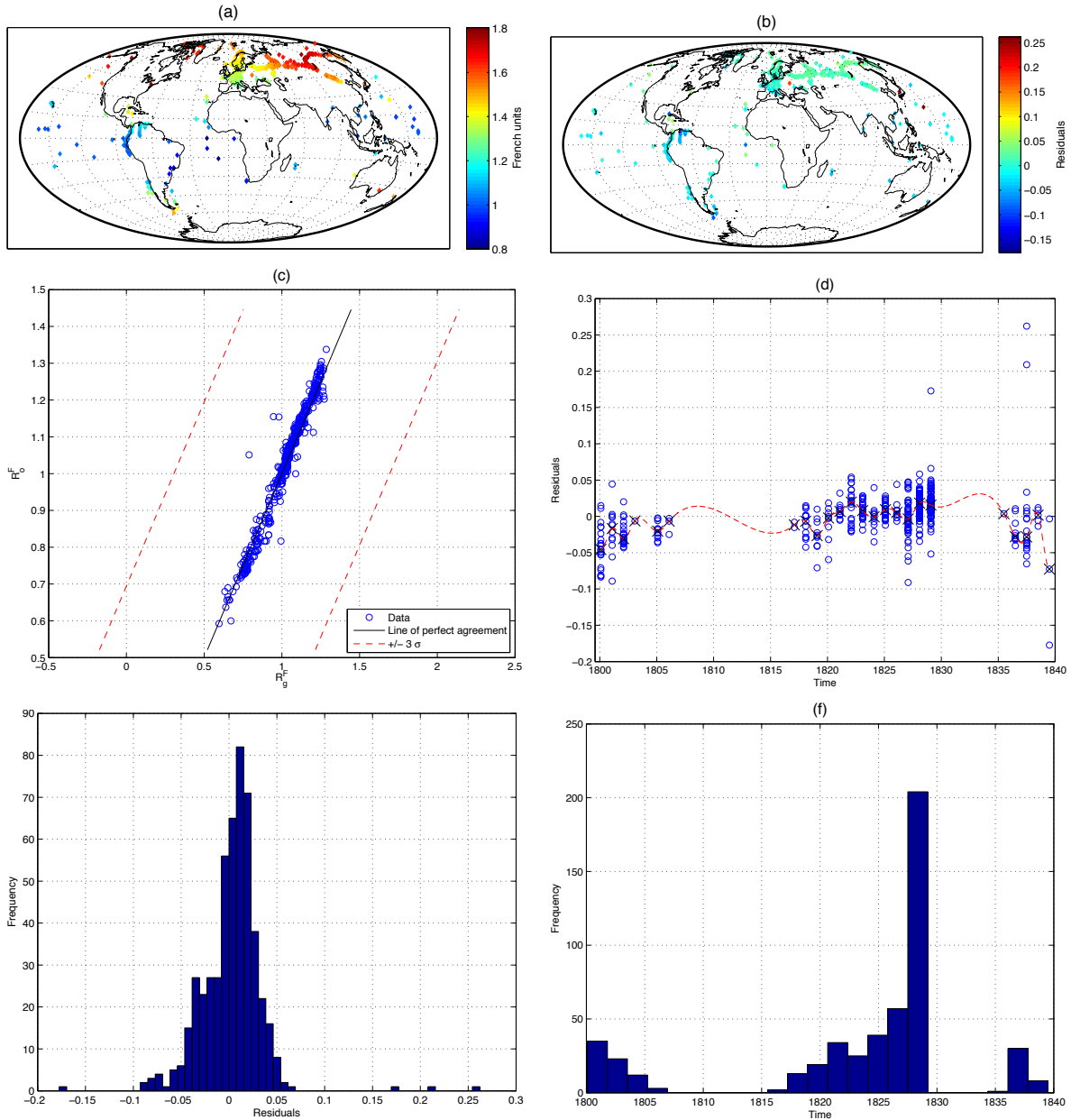


Figure 2.5: Plots of the RTF data set. (a) Spatial distribution of raw data, (b) Spatial distribution of residuals  $\Delta_R$ , (c) ratios  $R_g^H$  against  $R_o^H$ , (d) Temporal distribution of residuals  $\Delta_R$ . The X marks the median of residuals, interpolated by a least-squares fitted cubic spline (red dashed line), (e) Histogram of residuals  $\Delta_R$ , (f) Histogram showing data distribution in time

#### 2.1.2.4 Relative total intensity in Erman units (RTE)

The following data set was compiled from publications of Erman (cf. Erman [1835] and Erman [1841]), as well as of E. Sabine (cf. Sabine [1849], Sabine [1872], Sabine [1875], and Sabine [1877]). Further details concerning the sources contributing to this data set are found in Jonkers *et al.* [2003] under the ID code 4277. Referenced to the intensity measured at Portsmouth, only 17 relative intensity observations recorded in Erman units (all date to 1830.5) are available in

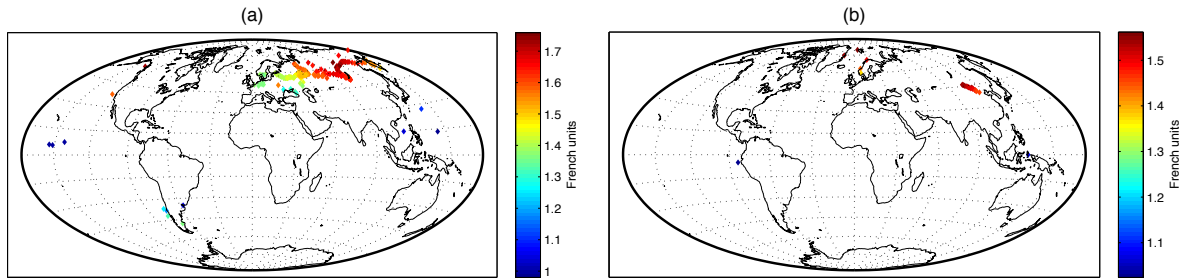


Figure 2.6: Plots of journeys: (a) observations made by Hansteen & Due and Erman on their East Siberia expedition (1828 – 1830), (b) observations made by Fuss on an expedition in 1823 to Beijing.

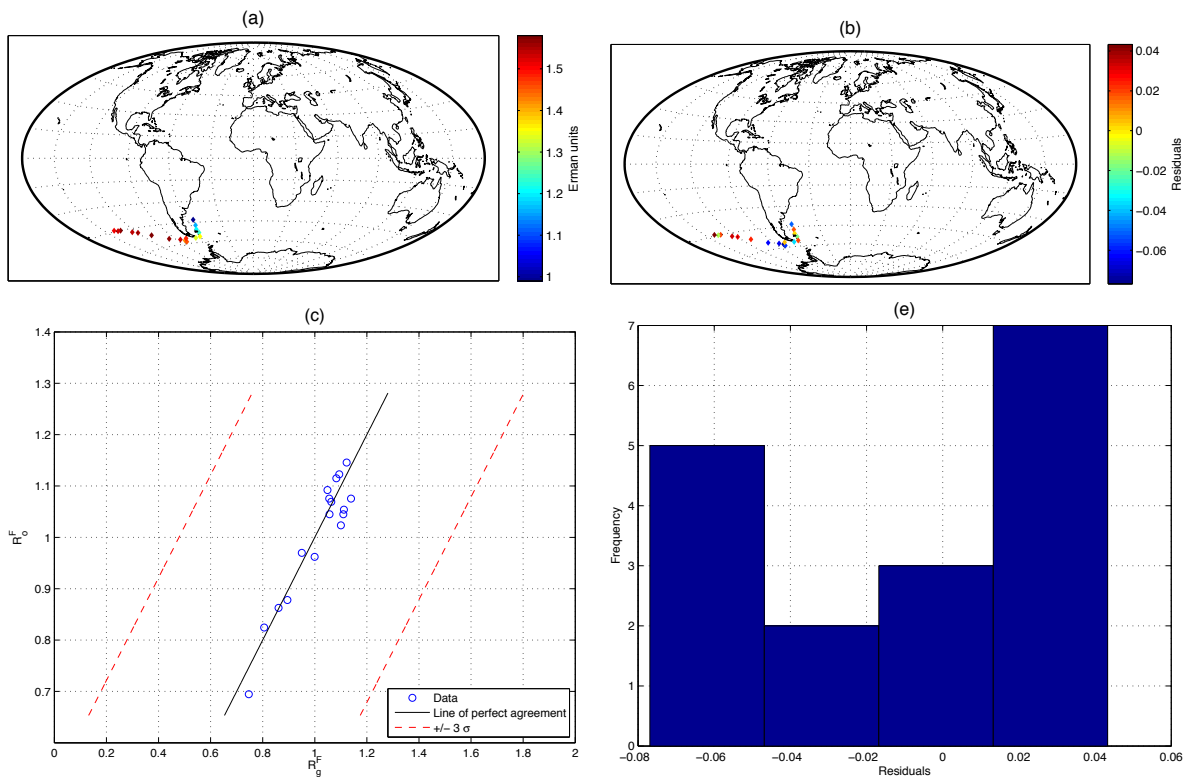


Figure 2.7: Plots of the RTE data set. (a) Spatial distribution of raw data, (b) Spatial distribution of residuals  $\Delta_R$ , (c) ratios  $R_g^H$  against  $R_o^H$ , (d) Histogram of residuals  $\Delta_R$ . No time plots are shown as all data are from the same year.

the historic geomagnetic database of Jonkers *et al.* [2003]. These data are additional data from the East Siberia/China expedition carried out in collaboration with Hansteen and Lt. Due, which supplement those appearing in the RTF data set (see previous section). Erman joined Hansteen and Lt. Due in St. Petersburg and together continued their voyage through Siberia. Later, Erman continued traveling through China, across the Atlantic, circumnavigating South America and back to Berlin.

The South Atlantic anomaly (cf. Figure 2.7 (a) and 1.2) is nicely imaged by this data whichh

show low intensity at the East coast of South America, decreasing while the voyage is heading eastwards (Figure 2.7 (a) and (b)). The linear trend shown in Figure 2.7 (c) suggests, the observations match well with the predicted values by *gufm1* (also see Figure 2.7 (b)). Due to the small amount of data, no clear interpretation of the error distribution can be made (Figure 2.7 (d)). For more detailed information see Table 2.6.

### 2.1.2.5 Relative total intensity in London units (RTL)

These data have been compiled and published by G. Erman (cf. Erman [1835] and Erman [1841]), R. Fitzroy (cf. Fitzroy [1839]) and E. Sabine (cf. Sabine [1840], Sabine [1843], Sabine [1846], Sabine [1872], Sabine [1875], and Sabine [1877]). Further details concerning the sources contributing to this data set are found in Jonkers *et al.* [2003] under the ID codes 4275, 4277, 4285, 4483, 4485, 4486 and 4487. Much of this data set (104 recordings) originates from the expeditions of the *Erebus* (1839 – 1841) and the *Krotkoi* (1828 – 1842) (Figure 2.9 (f)). Six observations of this data set were taken on the famous voyage of the *Beagle*, which was accompanied by Charles Darwin. A map showing its route is depicted in Figure 2.8.



Figure 2.8: Route of Beagle voyage. <sup>1</sup>

The expedition to the Antarctic regions (Figure 2.9 (a)) of *Erebus* was initiated by E. Sabine with the first objective given by the Admiralty: *'Whereas it has been represented to us that the science of magnetism may be essentially improved by an extensive series of observations made in high southern latitudes, and by a comparison of such observations with others made at certain fixed stations, and whereas practical navigation must eventually derive important benefits from every improvement in that science.'* Campbell [2009]. The British scientists related their intensity measurements to the value obtained in London and the state-of-the-art geomagnetic equipment (i.e. newest generation dip-circles, compasses and chronometers) on board.

The RTL data set is of special interest since data at high southern latitudes are rare. The observations nicely display the increase in intensity near the geomagnetic pole. Figures 2.9 (c) and (d) reveal four data points with stronger deviations from the line of perfect fit, but still within the  $3\sigma$  interval (these particular observations originate from the *Beagle*). As they are clearly not the result of a systematic error (e.g. demagnetisation of the needle), nor strongly

<sup>1</sup>Source: <http://george-and-dragon-pub-in-westerham.co.uk/images/Beagle-Voyage-550W.jpg> (06/22/2011)

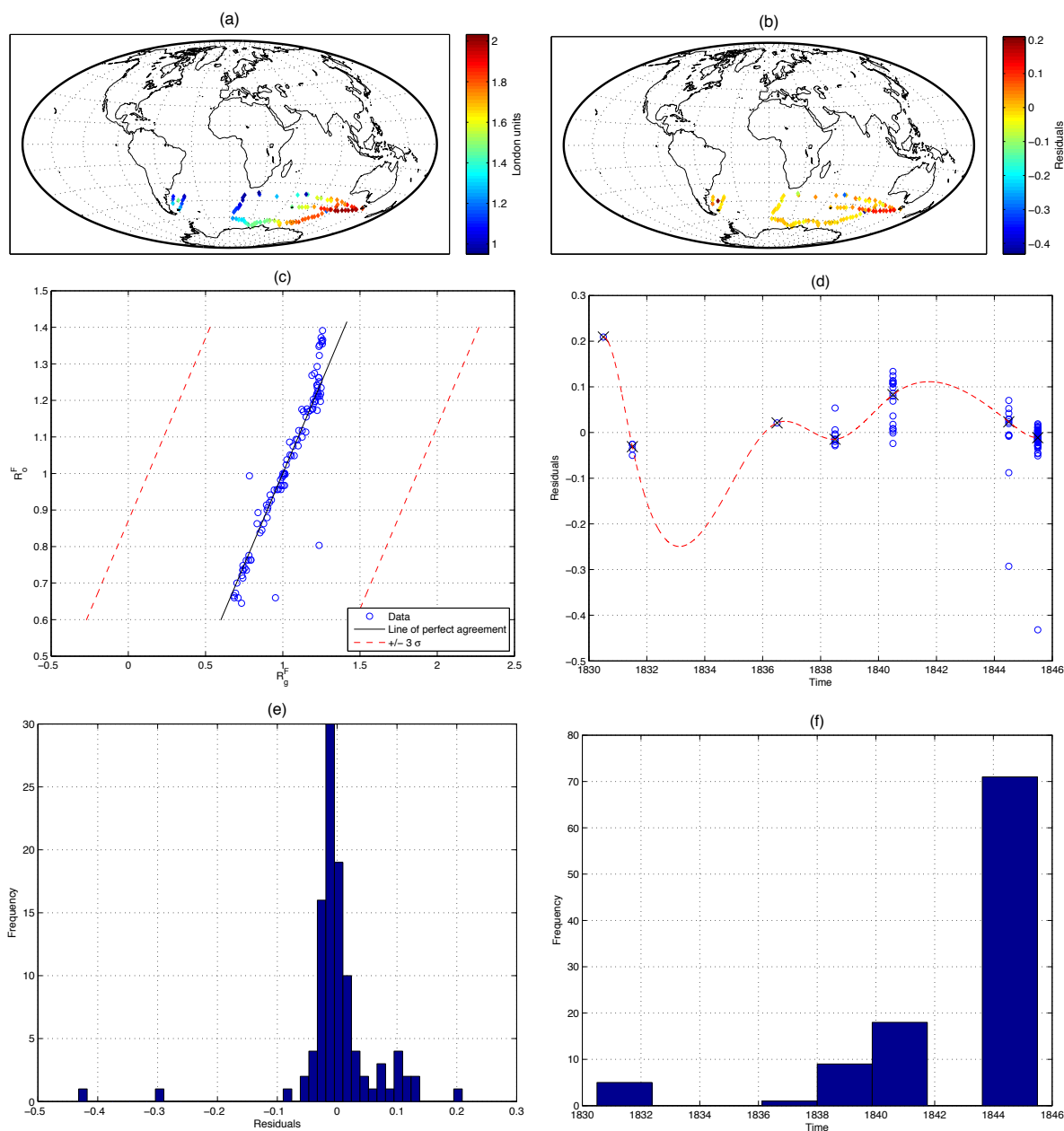


Figure 2.9: Plots of the RTL data set. (a) Spatial distribution of raw data, (b) Spatial distribution of residuals  $\Delta_R$ , (c) ratios  $R_g^H$  against  $R_o^H$ , (d) Temporal distribution of residuals  $\Delta_R$ . The X marks the median of residuals, interpolated by a least-squares fitted cubic spline (red dashed line), (e) Histogram of residuals  $\Delta_R$ , (f) Histogram showing data distribution in time

affected by the higher intensity of the low latitudes, measurement errors are the most plausible explanation. Plotting residuals against frequency (Figure 2.9 (e)) suggests an underlying Laplace probability distribution for this data set. For more detailed information see Table 2.6.

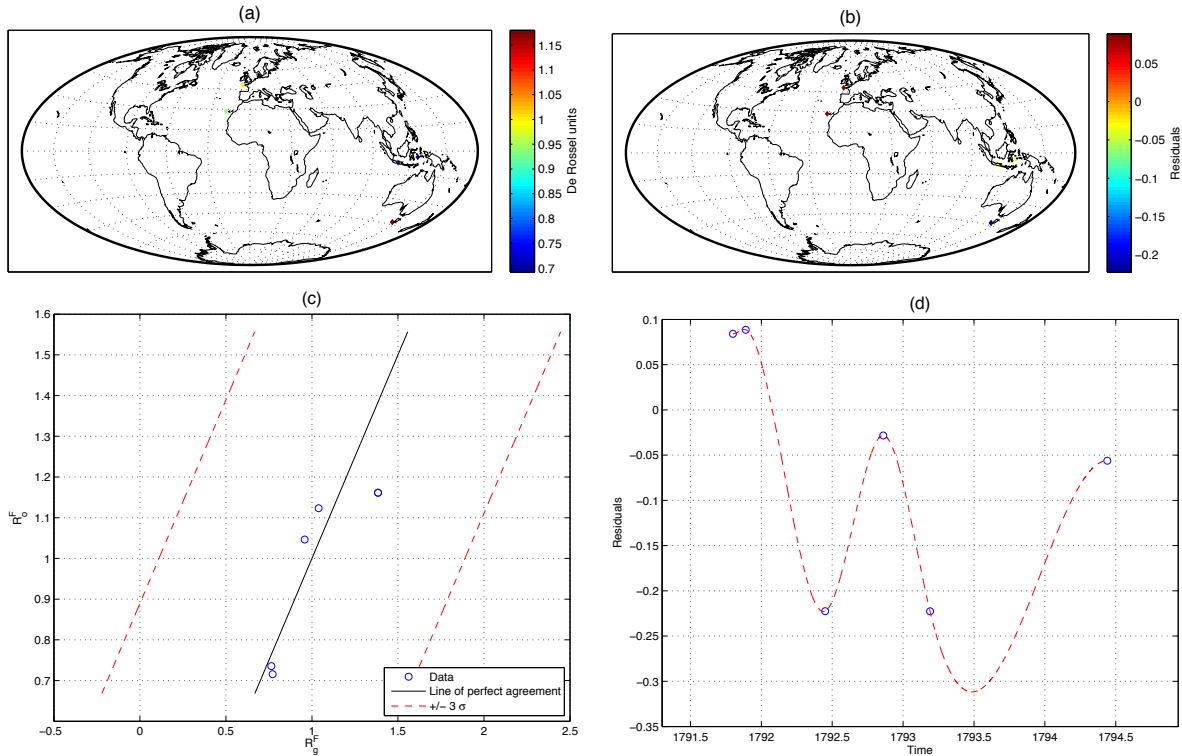


Figure 2.10: Plots of the RTR data set. (a) Spatial distribution of raw data, (b) Spatial distribution of residuals  $\Delta_R$ , (c) ratios  $R_g^H$  against  $R_o^H$ , (d) Temporal distribution of residuals  $\Delta_R$ . No histograms of data and residuals are shown due to the insufficient number of data

### 2.1.2.6 Relative total intensity in De Rossel units (RTR)

This data set was published by Walker [1866] (flocated in Jonkers *et al.* [2003] under the ID code 3500). The primary goal of this voyage (1791 – 1794) under Bunny Dentreasteaux was to find the two missing vessels commanded by Jean-François de la Pérouse. As a member of the expedition, French Admiral Jean De Rossel made relative measurements of the total magnetic intensity, which he related to the dip of his needle observed in Brest (an illustration of the dip-circle he used is shown in Figure 1.3) [Jonkers *et al.*, 2003]. The data set contains of only six measurements.

In his book on the voyage Dentreasteaux he writes: *"By comparing the experimental results obtained during the expedition with each other it is evident that the oscillations of the needle were more rapid at Paris and Van Diemens Land than at Surabaya in the isle of Java and at Amboyna; and therefore the magnetic force is greater near the poles than at the equator."*

In fact, De Rossel was the first scientist to publish the observation that the intensity of the geomagnetic field is stronger at the poles than at the equator, an observation often attributed to Alexander von Humboldt.

The data appears to be of comparable accuracy to the other data sets (see Figure 2.10 (b) and (c)). Oscillations from positive to negative residuals are found, but given the small amount

of data, no reliable trends nor interpretations can be made. For more detailed information see Table 2.6.

### 2.1.2.7 Relative total intensity in Humboldt units (RTH)

The data contributing to this subset was collected by baron Alexander von Humboldt (1769 – 1859), one of the pioneers of geomagnetic science. He provides a comprehensive dataset from various parts of the world over a range of  $115^\circ$  in latitude. The data is published in von Humboldt [1858] and von Humboldt [1850] and contains 112 additional observations to those previously collected in Jonkers *et al.* [2003].

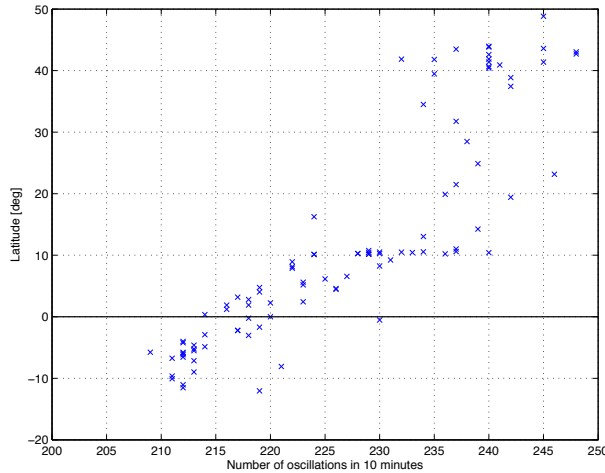


Figure 2.11: Plots of von Humboldt’s original observations [von Humboldt, 1850] against latitude. The solid black line denotes the equator. The increasing number of oscillations towards higher latitudes identifies the observations as total intensities. Note this plot shows the distribution of the raw data (i.e. before multiple entries in the three datasets have been removed).

Alexander von Humboldt references his observations to Micuipampa, a location near Cajamarca (Peru) where he found inclination to be zero (therefore lying on the geomagnetic equator). Unlike the relative intensities reported in the other data sets described, von Humboldt’s data are usually reported in terms of number of oscillations per ten minutes (i.e. frequency) of the magnetic needle, not as a ratio of intensity. These observations can be easily converted to comparable quantities using the fact that in von Humboldt [1858] both the frequency and relative intensity are reported for the locations. Using these data, the period at the reference location can be deduced and is found to be approximately  $t_{ref} = 211$  s. Having  $t_{ref}$ , equation (1.4) can be used to calculate the relative intensity. Further, latitudes recorded relative to Paris have been corrected to Greenwich.

Figure 2.12 (a) shows the geographical distribution of the data, revealing the two expeditions from which the data originate: Towards the end of 1798 von Humboldt started out on his expedition to South America. Not long after his return from South America, in 1805, von Humboldt together with Gay-Lussac journeyed through France, Germany, Switzerland and Italy

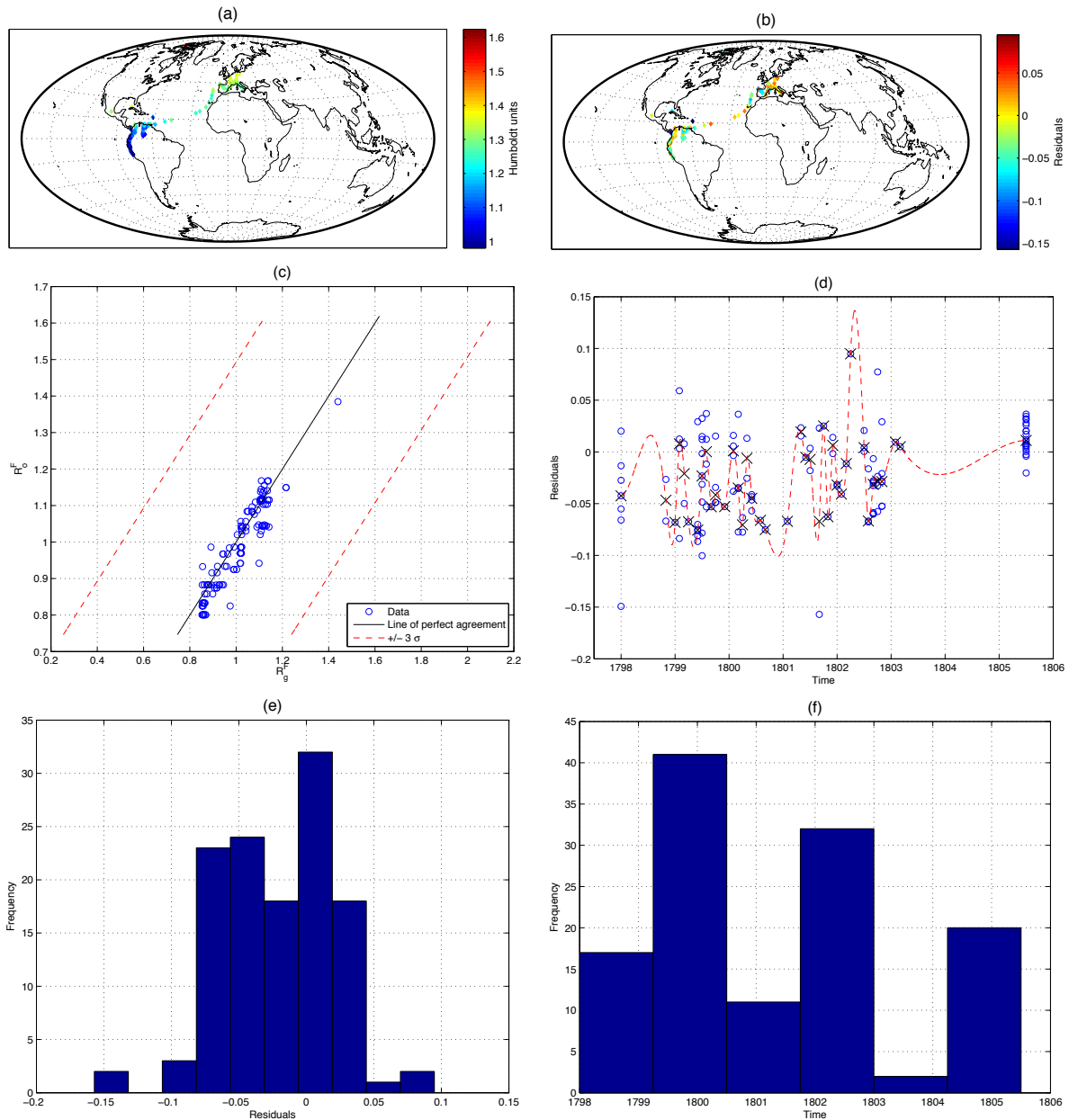


Figure 2.12: Plots of the RTH data set. (a) Spatial distribution of raw data, (b) Spatial distribution of residuals  $\Delta_R$ , (c) ratios  $R_g^H$  against  $R_o^H$ , (d) Temporal distribution of residuals  $\Delta_R$ . The X marks the median of residuals, interpolated by a least-squares fitted cubic spline (red dashed line), (e) Histogram of residuals  $\Delta_R$ , (f) Histogram showing data distribution in time

[Malin & Barraclough, 1991]. Some of the observations from the central Europe lack positional data. Fortunately, the name of the measurement location is often mentioned (e.g. ‘Hospice de St. Gotthard’) so that the missing latitude and longitude could easily be reconstructed. No information concerning the type of intensity measured by von Humboldt is explicitly reported. By plotting the frequencies against latitude (Figure 2.11) it is evident that the intensity recorded decreases towards the equator. The predominantly dipolar configuration of Earth’s magnetic field would not yield a horizontal intensity decreasing towards the equator. Thus it can be

concluded that the readings presented of von Humboldt are total intensities. Note that Figure 2.11 shows the distribution of the raw data. In a first processing step, multiple observations (i.e. observations made at equal time and position) in the three datasets have been removed. The data show good agreement with *gufm1* (Figures 2.12 (b) – (d)). The temporal data distribution (Figures 2.12 (e)) also reflects the voyages of von Humboldt (three peaks). For more detailed information see Table 2.6.

## 2.2 Error assignment

The total error of a geomagnetic observation primarily arises from three sources: navigational errors  $\sigma_n$ , caused by inaccurate determination of the geographical position, observational errors  $\sigma_o$ , comprising both imprecision in measurement and disturbances due to the increasing usage of iron in shipbuilding in time, and noise caused by interferences of the crustal magnetic field  $\sigma_c$  [Jackson *et al.*, 2000]. Since navigation was sufficiently accurate from the late 18th on, navigational errors are neglected. The final (diagonal) data covariance matrix  $\mathbf{C}_e$  is given by the sum of the crustal  $\mathbf{C}_c$  and observational covariance  $\mathbf{C}_o$  matrices with their elements  $\sigma_c^2$  and  $\sigma_o^2$ , respectively :

$$\mathbf{C}_e = \mathbf{C}_c + \mathbf{C}_o. \quad (2.7)$$

### 2.2.1 Errors assignment to $D$ , $I$ , $H$ and $F$

Jackson *et al.* [2000] showed that mariners in the 18th and 19th century were able to measure  $D$  within a standard deviation of approximately  $0.5^\circ$ . Little information, however, is available on the precision of inclination determination, hence the approach of Jackson *et al.* [2000] is adopted making use of the inverse proportionality of inclination and the total field intensity. Because the resolution in marine surveys is not sufficient, short wavelength features of the crustal field can not usually be known. Therefore statistical values for the influence of the crustal field discussed by Bloxham & Jackson [1992] are used. Error estimates were therefore assigned to  $D$  and  $I$  according to the following scheme:

$$\sigma_D = \frac{200 \text{ nT}}{H} \quad (2.8)$$

and

$$\sigma_I = \frac{300 \text{ nT}}{F} \quad (2.9)$$

with  $H$  and  $F$  values provided by an existing field model. In case of the Maury data set (only declination), tests have showed that noise contamination of the data is higher in comparison to the other declination data sets used, so a simple error of  $2.0^\circ$  is employed.

As the positional accuracy in latitude and longitude of `arch_all.cut.uniq.red` is only given to ten minutes, and that of `bn_after_rmv.uniq.red` to one degree (see section 2.1.1.1), an additional discretisation error must be considered

$$\sigma_d^2 = \left( \sigma_\phi \frac{\partial D}{\partial \phi} \right)^2 + \left( \sigma_\theta \frac{\partial D}{\partial \theta} \right)^2 \quad (2.10)$$

where  $\sigma_\phi = \sigma_\theta = (1/2\sqrt{3})^\circ$  [Jackson *et al.*, 2003].

Horizontal field intensity measurements are most commonly taken on-shore and therefore are likely to be more accurate than  $F$ , which was taken on-shore and off-shore. Following Bloxham & Jackson [1992], errors of 300 nT were assigned to observations of horizontal intensity, and 539 nT to such of total intensity. See Table 2.5 for a summary of all non-relative intensity data sets.

### 2.2.2 Errors assignment to relative intensity observations

In the case of relative intensities, an additional error has to be considered, namely random measurement errors  $\sigma_r$ , due to e.g. possible loss of magnetisation of the needle in the dip-circle or temperature variations. The total contribution to the data covariance matrix is

$$\mathbf{C}_e = \mathbf{C}_c + \mathbf{C}_o + \mathbf{C}_r \quad (2.11)$$

where  $\mathbf{C}_r$  is the random measurement covariance matrix with  $\sigma_r^2$  on its diagonal.

The error due to the crustal field was set to  $\sigma_c = 300$  nT and is converted to a relative error using the proportionality constant (= of 34,941 nT) for conversion of relative horizontal intensity in French units given by Jonkers *et al.* [2003]. The relative crustal error  $\sigma_c$  then reads 0.0085.

Furthermore temperature has an influence on the oscillation period (and therefore on the relative intensity observation itself). Figure 2.13 presents the results of an experiment conducted by Charles-Augustin de Coulomb. Although the temperature range at the observation locations is much smaller than presented in Figure 2.13 (it may range from  $-40^\circ$  C to maximally  $+40^\circ$  C), the change in period within this temperature is 31%.

To account for the change of period due to temperature variations, Sabine [1827] deduced the following expression, supposing the time of  $n$  oscillations is  $T$  [s] at temperature  $\Theta$  [ $^\circ$ F], and  $T'$  [s] at temperature  $\Theta'$  [ $^\circ$ F] [King, 2010] :

$$T = T' \left( 1 - \alpha(\Theta' - \Theta) \right), \quad \text{where } \alpha = 0.000165 \text{ [}^\circ\text{Fs}^{-1}\text{]} \quad (2.12)$$

Sabine [1827] reports a considerable increase in accuracy after applying equation (2.12), noting that in principle the coefficient  $\alpha$  is unique to each needle, and thus the temperature correction should be recalculated for each needle. Unfortunately, in most cases the temperature correction proposed by Sabine is not specifically mentioned and is therefore difficult to apply.

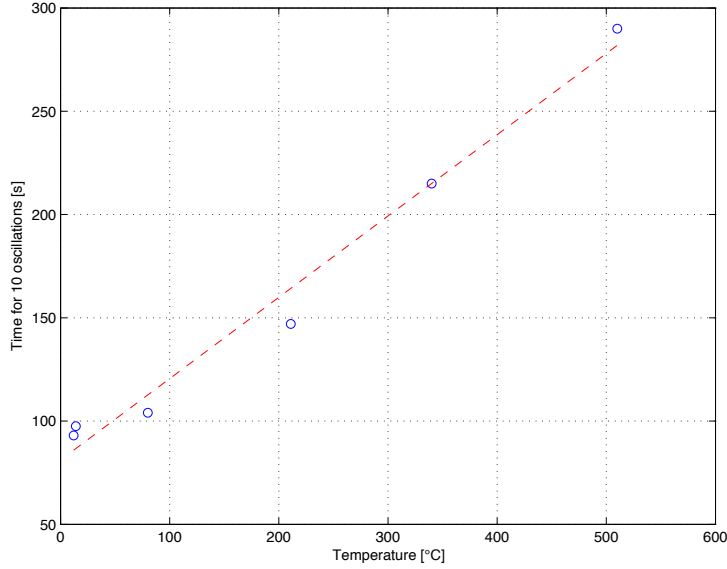


Figure 2.13: The results of an experiment conducted by Charles-Augustin de Coulomb (*blue*) showing the dependence of measured period on temperature, fit by a linear function (*magenta*)

The measurement of relative intensity has the caveat that the measurement of the period ((1.1)) is dependent on the magnetic moment of the needle. Thus, if magnetisation of the needle changed over time, it would not be possible to distinguish between loss of magnetisation and effects of secular variation. Sabine [1827] reports the results of an experiment measuring the relative horizontal intensity in Paris using six different needles. The standard deviation calculated from these repeated readings is assigned to  $\sigma_r$ , yielding  $\sigma_r = 0.0021$  London units, which corresponds to 73 nT (using the conversion factor of 34,514 nT given by Jonkers *et al.* [2003]).

Repeated observations, ideally made within one day, can be used to determine the observational error. 94 repeated observations (2 – 4 observations) were found in the RTF data set (see figure 2.14 (a)).

Let  $D_r^p = \{d_1^p, \dots, d_N^p\}$  be a set of repeated observations made at day  $p$ , and

$$\mu^p = \frac{1}{N} \sum_{i=1}^N d_i^p \quad (2.13)$$

denote their mean. From the observations and the corresponding daily mean the set of residuals at day  $p$  can be calculated by

$$r^p = \{d_1^p - \mu^p, \dots, d_N^p - \mu^p\}. \quad (2.14)$$

The observational error is then calculated by taking the (unbiased) standard deviation

$$\sigma_o = \sqrt{\frac{1}{N-1} \sum_{i=1}^N R_i^2} \quad (2.15)$$

in which  $R = \{r^1, \dots, r^p, \dots, r^M\}$  denotes a set holding the sets residuals of repeated observations for all different days. A plot of  $R$  is given in Figure 2.14 (b). The observational error is hence  $\sigma_o = 0.016$  French units. Using the conversion coefficient of 34,941 nT for French units to nT given in Jonkers *et al.* [2003], this corresponds to 559 nT, which is compatible to the error estimates assigned to absolute total intensities.

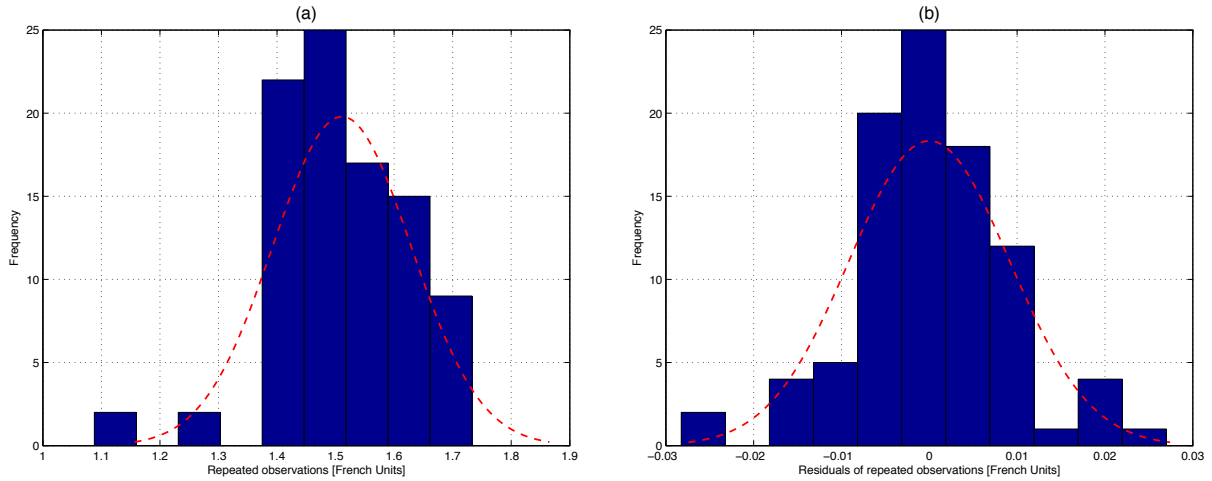


Figure 2.14: Repeated observations from RTF data set. (a) Histogram of available repeated observations with superimposed gaussian PDF. (b) Histogram of residuals from daily means obtained from repeated observations with superimposed gaussian PDF. The standard deviation of residuals is  $\sigma = 0.016$  French units (i.e. 559 nT)

For simplicity, the errors are assumed to take on the same values for all relative intensity data sets. The total error budget for the relative intensity data is summarised in Table 2.4. These fill the required diagonal elements of the error covariance matrix  $\mathbf{C}_e$ .

Needle	$\frac{H_{Paris}}{H_{London}}$
I	1.0732
II	1.0675
III	1.0726
IV	1.0723
V	1.0709
VI	1.0717

Table 2.3: Results of an experiment conducted by Sabine in 1827 (cf. Sabine [1827] and Becquerel [1840]) in which the ratio of horizontal intensity in Paris to London was calculated using a set of six different needles

	$\sigma_c$	$\sigma_o$	$\sigma_r$	Total
Relative errors:	0.0085	0.016	0.0021	0.0266
Errors in nT:	300	73	559	932

Table 2.4: Table summarising the error contributions to relative intensity observations along with their conversions to nT, using the conversion factors given in Jonkers *et al.* [2003].  $\sigma_c$  is the crustal error,  $\sigma_o$  the observational error and  $\sigma_r$  the random error. The total error is assumed to apply to hold for all relative intensities

Data set	Time span	<i>D</i>		<i>I</i>		<i>H</i>		<i>F</i>	
		<i>N</i>	$\sigma_D$ [nT]	<i>N</i>	$\sigma_I$ [nT]	<i>N</i>	$\sigma_H$ [nT]	<i>N</i>	$\sigma_F$ [nT]
arch_all.cut.uniq.red	1884.5 – 1857.5	9,578	†						
bn_after_rmv.uniq.red	1791.0 – 1893.0	31,489	†						
incl_extra.dat	1791.5 – 1804.3			68	600.0				
Maury Collection	1792.3 – 1909.5	78,314	2.0*						
London declination	1790.5 – 1906.5	119	200.0						
London inclination	1790.5 – 1909.5			90	300.0				
Paris declination	1790.5 – 1909.5	105	200.0						
Paris inclination	1790.5 – 1909.5			100	300.0				
survey.norpt	1840.0 – 1910.0	24,752	228.0	17,480	296.00	11,798	300.0	3,616	539.0
survh.norpt	1790.5 – 1839.5	4,094	228.0	2,304	480.0	500	300.0	1013	539.0
Vaq_Af1880_jb.dat	1877.9 – 1885.5	42	282.0	50	360.0	49	282.0		

Table 2.5: Table summarising the absolute data sets. † The error estimates marked with are location dependent and are calculated by equation (2.10). \* this error estimate is given in degrees

Data set	Time span	<i>H</i>		<i>F</i>	
		<i>N</i>	$\sigma_H$	<i>N</i>	$\sigma_F$
RHF	1799.5 – 1838.5	22	0.0266		
RTF	1800.1 – 1839.5			505	0.0266
RTE	1830.5 – 1830.5			17	0.0266
RTL	1831.5 – 1845.5			104	0.0266
RTR	1791.8 – 1794.4			6	0.0266
RTH	1798.0 – 1805.5			123	0.0266

Table 2.6: Table summarising the relative intensity data sets

### 2.2.3 Summary of recommendations concerning use of relative intensity data

123 new relative intensity data not previously present in the database of Jonkers *et al.* [2003] (i.e. the RTH data set) in addition to the relative intensity data from the database of Jonkers *et al.* [2003] were collated and checked for biases in space and time. Furthermore, error estimates were calculated and assigned to the relative intensity data. The RTL data originating from the Antarctic region could possibly be less accurate than the other data sets. The relative intensity data sets show generally good agreement with the predictions of *gufm1* and are thus preliminarily recommended to use, with exception of the RHF data set. A final recommendation concerning the use of relative intensity data is given in section 5.3. The RHF data set 2.1.2.2 is likely to

suffer from a systematic bias in space and time. A discussion of this problem is given in section 5.2.

# Chapter 3

## Methodology

### 3.1 Core field modeling

#### 3.1.1 Governing equations

Assuming an insulating mantle (i.e. electromagnetic vacuum), Maxwell's equations for the magnetic field  $\mathbf{B}$  outside the core reduce to

$$\nabla \times \mathbf{B} = 0 \quad (3.1)$$

and

$$\nabla \cdot \mathbf{B} = 0. \quad (3.2)$$

As is seen from equation (3.2),  $\mathbf{B}$  spans a conservative vector field, thus

$$\exists V: \mathbf{B} = -\nabla V, \quad (3.3)$$

where  $V$  is the scalar magnetic potential. Combining equations (3.2) and (3.3) yields Laplace's equation:

$$\nabla \cdot \mathbf{B} = \nabla \cdot -\nabla V = \nabla^2 V = 0. \quad (3.4)$$

The solution in spherical geometry reads

$$V = a \sum_{l=1}^{\infty} \sum_{m=0}^l \left\{ \left( \frac{r}{a} \right)^l \left[ e_l^m \cos(m\phi) + f_l^m \sin(m\phi) \right] P_l^m(\cos \theta) + \left( \frac{a}{r} \right)^{l+1} \left[ g_l^m \cos(m\phi) + h_l^m \sin(m\phi) \right] P_l^m(\cos \theta) \right\}, \quad (3.5)$$

in which  $(r, \theta, \phi)$  are the spherical polar coordinates,  $a$  the reference radius (i.e. Earth's mean radius (6371 km)). The elements of the set of coefficients  $G = \{e_k^m, f_k^m, g_l^m, h_l^m\}$  are referred to as Gauss coefficients, which have the dimensions of  $nT$ , and  $P_l^m(\cos \theta)$  the Schmidt quasi-normalised associated Legendre functions [Backus *et al.*, 1996], defined such that

$$\int_0^{2\pi} \int_0^\pi P_l^m(\cos \theta) P_{l'}^{m'}(\cos \theta) \begin{cases} \cos(m\phi) \cos(m'\phi) \\ \sin(m\phi) \sin(m'\phi) \end{cases} \sin(\theta) d\theta d\phi = \begin{cases} \frac{4\pi}{2l+1} & \text{if } l = l', m = m' \\ 0 & \text{otherwise.} \end{cases} \quad (3.6)$$

The potential equation (3.5) consists out of two parts: As  $r \rightarrow \infty$ , the terms multiplied by  $(a/r)^l$  vanish, and are thus associated with the externally generated field with respect to the Earth's surface. Terms multiplied by  $(r/a)^{l+1}$ , however, remain finite, and are therefore used to describe the magnetic field of internal origin. In this thesis, the magnetic field at the core-mantle boundary (CMB) is modelled as a potential field resulting from a purely internal source. Hence equation (3.5) reduces to

$$V = a \sum_{l=1}^{\infty} \sum_{m=0}^l \left(\frac{a}{r}\right)^{l+1} \left[ g_l^m(t) \cos(m\phi) + h_l^m(t) \sin(m\phi) \right] P_l^m(\cos \theta). \quad (3.7)$$

To diminish the infinite dimensional problem to finite dimensions, the spherical harmonic expansion is truncated at degree  $L = 14$ , below which the core field is believed to dominate the spherical harmonic expansion (see Figure 3.1, reproduced from Maus *et al.* [2008]).

### 3.1.2 Representation of the time-dependence: B-Splines

To introduce time-dependence (i.e. to account for secular variation), the Gauss coefficients are expanded in terms of cubic B-Splines:

$$g_l^m(t) = \sum_{i=1}^N {}^i g_l^m B_{i,k}(t), \quad (3.8)$$

and

$$h_l^m(t) = \sum_{i=1}^N {}^i h_l^m B_{i,k}(t). \quad (3.9)$$

The time-dependent Gauss coefficients  $\{g_l^m(t), h_l^m(t)\}$  are linear combinations of the spline coefficients  $\{{}^i g_l^m(t), {}^i h_l^m(t)\}$  and the piecewise polynomial functions  $B_{i,k}(t)$  of, generally written, order  $k$  and degree  $(k - 1)$ , where  $B_{i,k}(t) : [t_0, t_{i+1}] \rightarrow \mathbb{R}^3$ . Moreover  $B_{i,k}(t) \in C^{k-2}$  on  $[t_0, t_{i+1}]$  (i.e.  $B_{i,k}(t)$  is  $(k - 2)$  times continuously differentiable across the segments).

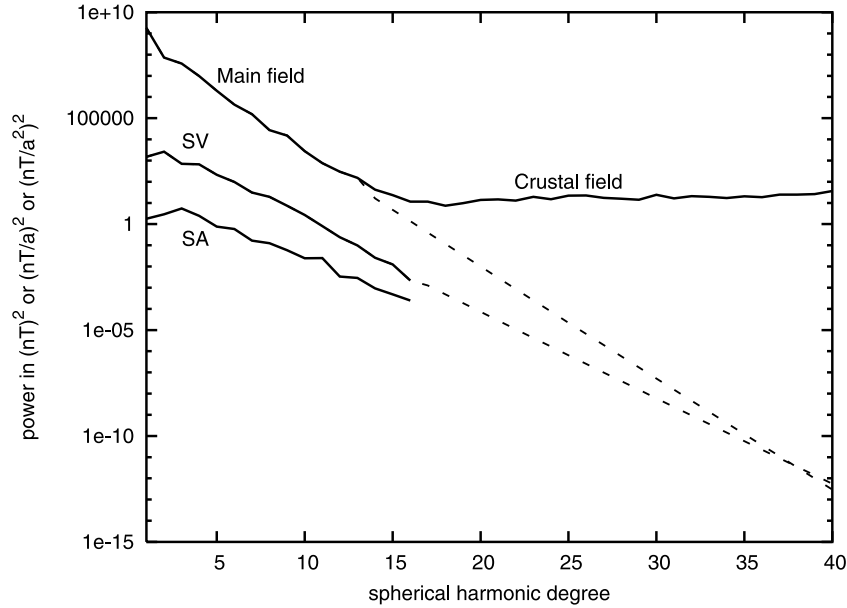


Figure 3.1: Spherical harmonic power spectrum at the Earth's surface. At degree  $L = 14$ , the crustal field overwhelms the core field, which starts to interact at approximately  $L = 11$ . Hence the spherical harmonic expansion is truncated at  $L = 14$ . Further, the figure shows the spectra for secular variation (SV) and secular acceleration (SA). Reproduced from Maus *et al.* [2008]

Let  $K$  be a set of numbers  $K = \{t_0, \dots, t_j\} \in [t_s, t_e]$ , where  $t_0 \leq t_1 \leq \dots \leq t_j$ , and  $[t_s, t_e]$  is the model time span.  $K$  is referred to as the knot vector, its elements the knot points, and the half-open interval  $[t_i, t_{i+1}[$  the  $i$ -th knot span. The knots points can be considered as division points that subdivide the interval  $[t_0, t_j]$  into knot spans De Boor [1972]. The knot points were chosen to be equally spaced with knot spacing of 2 years

$$t_{i+1} - t_i = 2, \quad (3.10)$$

resulting in 61 knots in the time interval spanned by the model. Additionally, the knot vector  $K$  has to be appended by three knot points at each end to define the basis functions at the beginning and end of the model, giving a total of 67 knot points. These correspond to  $(67 - k)$  B-Splines, thus the truncation level for the temporal basis functions is  $N = 63$ .

For evaluation of the B-Splines, the recursive *Cox-DeBoor Algorithm* is used:

$$B_{i,0}(t) := \begin{cases} 1 & \text{if } t \in [t_i, t_{i+1}[ \\ 0 & \text{otherwise} \end{cases}$$

and

$$B_{i,k}(t) := \frac{t - t_i}{t_{i+k} - t_i} B_{i,k-1}(t) + \frac{t_{i+k+1} - t}{t_{i+k+1} - t_{i+1}} B_{i+1,k-1}(t). \quad (3.11)$$

Equations (3.8) and (3.9), respectively, may be represented in a matrix equation of the form

$$\mathbf{g} = \mathbf{A} \mathbf{x}. \quad (3.12)$$

$\mathbf{A}$  is a symmetric and positive-definite matrix and  $\mathbf{x}$  contains the spline coefficients  ${}^i g_l^m$  and  ${}^i h_l^m$ . Such a system of linear positive-definite equations is efficiently solved using Cholesky decomposition, a triangular decomposition scheme which constructs a lower triangular matrix  $\mathbf{L}$  such that

$$\mathbf{L} \cdot \mathbf{L}^T = \mathbf{A}. \quad (3.13)$$

For a detailed discussion see Press *et al.* [2007] (p100, 120 – 124) .

The motivation for using B-Splines as the temporal basis functions is threefold:

1.  $B_{i,k}(t) > 0$  only for  $t \in [t_i, t_i + 4]$  and is therefore ideal for recovering localised features
2. the banded form of the normal equation matrix reduces computational storage considerably
3.  $B_{i,k}(t)$  is twice continuously differentiable across the knot points, ensuring a smooth representation and the ability to trace secular variation (first derivative)

### 3.1.3 Geomagnetic observables

Expressions for the spherical polar components ( $B_\theta, B_\phi, B_r$ ) of the magnetic field  $\mathbf{B}$  are obtained by taking the gradient of equation (3.7):

$$B_\theta = -\frac{1}{r} \frac{\partial V}{\partial \theta} = -\sum_{l=1}^{\infty} \sum_{m=0}^l \left(\frac{a}{r}\right)^{l+2} \left[ g_l^m(t) \cos(m\phi) + h_l^m(t) \sin(m\phi) \right] \frac{\partial P_l^m(\cos \theta)}{\partial \theta}, \quad (3.14)$$

$$B_\phi = \frac{1}{r \sin \phi} \frac{\partial V}{\partial \phi} = \frac{1}{\sin \theta} \sum_{l=1}^{\infty} \sum_{m=0}^l m \left(\frac{a}{r}\right)^{l+2} \left[ g_l^m(t) \sin(m\phi) + h_l^m(t) \cos(m\phi) \right] P_l^m(\cos \theta), \quad (3.15)$$

$$B_r = \frac{\partial V}{\partial r} = \sum_{l=1}^{\infty} \sum_{m=0}^l (l+1) \left(\frac{a}{r}\right)^{l+2} \left[ g_l^m(t) \cos(m\phi) + h_l^m(t) \sin(m\phi) \right] P_l^m(\cos \theta). \quad (3.16)$$

The magnetic observables ( $X, Y, Z, H, F, D, I$ ), introduced in section 1.1, are related to the spherical polar field components ( $B_\theta, B_\phi, B_r$ ), and thus the model parameters, by the following equations:

$$X = -B_\theta, \quad (3.17)$$

$$Y = B_\phi, \quad (3.18)$$

$$Z = -B_r, \quad (3.19)$$

$$H = \sqrt{B_\theta^2 + B_\phi^2}, \quad (3.20)$$

$$F = \sqrt{B_\theta^2 + B_\phi^2 + B_r^2}, \quad (3.21)$$

$$D = \arctan\left(\frac{B_\phi}{-B_\theta}\right), \quad (3.22)$$

$$I = \arctan\left(\frac{-B_r}{(B_\theta^2 + B_\phi^2)^{\frac{1}{2}}}\right), \quad (3.23)$$

where  $D \in [-\pi, \pi]$  and  $I \in \left[-\frac{\pi}{2}, \frac{\pi}{2}\right]$ .

## 3.2 Regularised inversion

### 3.2.1 General considerations

Any inverse problem is the result of an associated forward function, describing the relation between data points and model parameters:

$$\mathbf{y} = \Gamma(\mathbf{x}) \quad (3.24)$$

where  $\Gamma$  is the forward operator,  $\mathbf{x}$  a set of data points and  $\mathbf{y}$  a set of model parameters. In general, the solution to equation (3.24) can be stated as

$$\mathbf{x} = \Gamma^{-1}(\mathbf{y}) \quad (3.25)$$

where  $\Gamma^{-1}$  is an inverse operator.

There are three issues, following Parker [1994], related to the problem of finding the solution equation (3.25):

1. **Existence of a solution**

For geophysical inverse problems the existence is of minor importance since the inverse operator can generally be computed using well established discrete numerical techniques.

2. **Uniqueness of a solution**

In order to obtain a unique solution to equation (3.25), the forward operator  $\Gamma$  must be

strictly injective, implying

$$\Gamma(\mathbf{x}_1) = \Gamma(\mathbf{x}_2) \Rightarrow \mathbf{x}_1 = \mathbf{x}_2. \quad (3.26)$$

Backus & Gilbert [1970] and Parker [1994] showed that geophysical inverse problems suffer inherent non-uniqueness due to the finiteness of the number of data points available for any inversion process, the imprecision of those data points, and the infinite dimensionality of the continuum quantities to be estimated from the data.

### 3. Stability of a solution

Two types of stability have to be considered. Firstly, the physical stability of a solution. It describes how small perturbations in the data propagate into the model parameters. Ideally, these should have very little effect. Secondly, the stability of the applied numerical algorithms has to be guaranteed.

The inverse problem where one wants to estimate a continuous model with infinitely many degrees of freedom from a finite data set (i.e. conditions 2 and 3 are violated) is referred to as an ill-posed inverse problem. In order to obtain a problem which satisfies the conditions of (limited) uniqueness and stability, regularisation is applied.

#### 3.2.2 Inverse methodology

Knowing  $\mathbf{m} = \{g_l^m(t); h_l^m(t)\}$  allows the evaluation of the model at any particular time in  $[t_s, t_e]$  and therefore calculation of the desired components of the geomagnetic field, using equation (3.7). The Gauss coefficients are obtained by iteratively fitting the coefficients to the observations by a regularised non-linear least-squares parameter estimation, since  $H$ ,  $F$ ,  $D$  and  $I$  are non-linearly related to the Gauss coefficients (see section 3.1.3).

Generally, the data is related to the model parameters by the following relation:

$$\mathbf{d} = \mathbf{f}(\mathbf{m}) + \mathbf{e}, \quad (3.27)$$

where  $\mathbf{d}$  is the data vector ( $\dim(\mathbf{d}) = M$ ),  $\mathbf{m}$  is the model vector,  $\mathbf{f}$  is a non-linear unknown functional of  $\mathbf{m}$  ( $\dim(\mathbf{m}) = N \cdot L(L + 2) = 63 \cdot 14 \cdot 16 = 14,112$ ) and the independent geodetic variables  $(\theta, \phi, r, t)$ , and  $\mathbf{e}$  is the vector associated with the uncertainties in the data, assumed to follow a normal distribution.

The smoothest model for a given fit to the data is found by seeking a model vector  $\mathbf{m}$  that minimises the misfit to the data as well as minimising two (regularising) norms,  $\Psi_s$  and  $\Psi_t$  that measure the spatial and temporal complexity of the solution.

Regularisation is required due to the inhomogeneous distribution of data as well as different geomagnetic data types, both in space and time. Furthermore, downward continuation is insidious for two reasons. Firstly, fields close to the source region have more detailed physical

content because shorter wavelengths of the field do not reach larger distances, i.e. short wavelengths are amplified. Secondly, the factor  $(a/r)^{l+1}$  in equation (3.7) increases with increasing  $l$ , destabilising the entire process (see, for example, [Bloxham *et al.*, 1989]).

The spatial norm  $\Psi_s$  is chosen to be

$$\Psi_s(\mathbf{m}) = \frac{\lambda_s}{t_e - t_s} \int_{t_s}^{t_e} \iint_{\partial V} (B_r)^2 \, d\Omega \, dt = \frac{\lambda_s}{t_e - t_s} \int_{t_s}^{t_e} \frac{(l+1)^2}{2l+1} \left(\frac{a}{r}\right)^{(2l+4)} \, dt, \quad (3.28)$$

and the temporal norm

$$\Psi_t(\mathbf{m}) = \frac{\lambda_t}{t_e - t_s} \int_{t_s}^{t_e} \iint_{\partial V} \left( \frac{\partial^2 B_r}{\partial t^2} \right)^2 \, d\Omega \, dt. \quad (3.29)$$

These two norms combined yield the regularisation matrix

$$\mathbf{R}_m = \lambda_s \Psi_s + \lambda_t \Psi_t, \quad (3.30)$$

where  $\lambda_s$  and  $\lambda_t$  are the spatial and temporal damping parameters (Lagrange multipliers), respectively.

The model estimate  $\mathbf{m}$  is the model which minimises the objective function

$$\Theta(\mathbf{m}) = [\mathbf{d} - \mathbf{f}(\mathbf{m})]^T \mathbf{C}_e^{-1} [\mathbf{d} - \mathbf{f}(\mathbf{m})] + \mathbf{m}^T \mathbf{R}_m^{-1} \mathbf{m}, \quad (3.31)$$

in which  $\mathbf{C}_e^{-1}$  is the data covariance matrix, a diagonal weighting matrix with elements  $(1/\sigma_i^2)$  where  $\sigma_i$  is the data uncertainty estimate.

The solution to equation (3.31) is found iteratively using a quasi-Newton scheme:

$$\mathbf{m}_{i+1} = \mathbf{m}_i + \left( \mathbf{A}^T \mathbf{C}_e^{-1} \mathbf{A} + \mathbf{R}_m^{-1} \right)^{-1} \left( \mathbf{A}^T \mathbf{C}_e^{-1} [\mathbf{d} - \mathbf{f}(\mathbf{m}_i)] - \mathbf{R}_m^{-1} \mathbf{m}_i \right), \quad (3.32)$$

with  $\mathbf{m}_i$  denoting the model at the  $i$ th iterate,  $\mathbf{m}_{i+1}$  its successor, and

$$\mathbf{A} = \left. \frac{\partial \mathbf{f}(\mathbf{m})}{\partial \mathbf{m}} \right|_{\mathbf{m}=\mathbf{m}_i} \quad (3.33)$$

the sensitivity matrix containing the Fréchet derivatives of the geomagnetic observables with respect to each model parameter.

The procedure is terminated when the convergence criterion

$$|\Theta(\mathbf{m}_i) - \Theta(\mathbf{m}_{i-1})| < \epsilon \quad (3.34)$$

is met, giving the final model by assuming

$$\mathbf{m} = \mathbf{m}_i. \quad (3.35)$$

### 3.3 Extension of the standard formalism

#### 3.3.1 Implementation of relative intensity observations

The main advance reported in this thesis is the incorporation of relative intensity observations in the modelling formalism. As shown in section 1.3, any relative intensity observation (in units of  $k$ ) is related to a corresponding absolute observable by a product of the form

$$F_i^{r,k}(\theta, \phi, r, t) = \alpha_k \cdot F_i(\theta, \phi, r, t) \quad (3.36)$$

for relative total intensity or

$$H_i^{r,k}(\theta, \phi, r, t) = \alpha_k \cdot H_i(\theta, \phi, r, t) \quad (3.37)$$

for relative horizontal intensity, where  $k$  denotes the unit the observation is made in. Note that the proportionality constant  $\alpha_k$  is assumed time-independent but different for each class of units of the relative intensity observations.

Since the relative intensity data in this study are delivered in six different units, the model vector  $\mathbf{m}$  must be augmented by six additional relative intensity model parameters  $\alpha_{RHF}$ ,  $\alpha_{RTF}$ ,  $\alpha_{RTE}$ ,  $\alpha_{RTL}$ ,  $\alpha_{RTR}$ , and  $\alpha_{RTH}$  (for abbreviations see sections 2.1.2.2 – 2.1.2.7), each corresponding to a different relative intensity unit:

$$\mathbf{m} = \left( g_1^0(t), g_1^1(t), h_1^1(t), \dots, h_{14}^{14}(t), \alpha_{RHF}, \alpha_{RTF}, \alpha_{RTE}, \alpha_{RTL}, \alpha_{RTR}, \alpha_{RTH} \right). \quad (3.38)$$

Thus, the total number of model parameter is now  $P = N \cdot L(L + 2) + 6 = 14118$ .

A second change is a modification of kernel matrix  $\mathbf{A}$ , given in equation (3.33), to include the relative intensities. The following derivation demonstrates the calculation of  $\mathbf{A}$  for the example of relative horizontal intensity given in French units. Then, recalling that  $H_i^{r,RHF} = \alpha_{RHF} H_i$ , the corresponding kernel matrix then reads

$$\mathbf{A}^{RHF} = \frac{\partial \mathbf{f}(\mathbf{m})}{\partial \mathbf{m}} \quad (3.39)$$

$$= \left(\frac{a}{r}\right)^{l+2} \begin{pmatrix} \frac{\partial H_i^{r,RHF}}{\partial g_1^0(t)} & \frac{\partial H_i^{r,RHF}}{\partial g_1^1(t)} & \frac{\partial H_i^{r,RHF}}{\partial h_1^1(t)} & \cdots & \frac{\partial H_i^{r,RHF}}{\partial \alpha_{RHF}} & \cdots & \frac{\partial H_i^{r,RHF}}{\partial \alpha_{RTH}} \end{pmatrix} \quad (3.40)$$

$$= \alpha_{RHF} \left(\frac{a}{r}\right)^{l+2} \begin{pmatrix} \frac{\partial H_i}{\partial g_1^0(t)} & \frac{\partial H_i}{\partial g_1^1(t)} & \frac{\partial H_i}{\partial h_1^1(t)} & \cdots & \frac{\partial H_i}{\partial \alpha_{RHF}} & \cdots & \frac{\partial H_i}{\partial \alpha_{RTH}} \end{pmatrix} \quad (3.41)$$

$$= \alpha_{RHF} \left(\frac{a}{r}\right)^{l+2} \begin{pmatrix} \frac{\partial H_i}{\partial g_1^0(t)} & \frac{\partial H_i}{\partial g_1^1(t)} & \frac{\partial H_i}{\partial h_1^1(t)} & \cdots & \frac{H_i}{\alpha_{RHF}} & 0 & 0 & 0 & 0 & 0 \end{pmatrix}, \quad (3.42)$$

and accordingly for the remaining relative intensities.

### 3.4 Modelling assumptions

Several assumptions are introduced in formulation of sections 3.1 – 3.3: Firstly, equation (3.7) is assumed to hold everywhere outside the core. This postulate assumes the effects mantle conductivity on periods of year and longer studied here to be negligible. Due to the fact that little is known about the conductivity of the deep mantle, the mantle is effectively assumed to be an electrical insulator. Secondly, the contribution of externally generated fields are neglected. It is believed that external field, which mainly on very short time scales, has little influence on the core-generated magnetic field. However, the observations of the magnetic elements at the Earth's surface, for example at observatories, are indeed influenced by the external fields. Finally, the crustal field, is not explicitly accounted for. In this thesis, the crustal field is treated as a further source of noise in the data and the approach of Holme & Jackson [1997] anisotropy crustal errors is adopted. The theory developed for the use of relative intensity data assumes the proportionality factor  $\alpha_k$ , relating relative to absolute intensity (see equations (3.36) and (3.36)), to be time-independent.

# Chapter 4

## Results

This chapter presents the results concerning the questions posed in Chapter 1, obtained using the non-linear regularised inversion scheme introduced in Chapter 3.

Eight different models, spanning the period 1790 – 1910, have been constructed. Two models (*bg19-1a* and *bg19-2b*) were constructed not including the relative intensity data sets, to explore the impact of the Maury Collection (MC) on time-dependent field models. Six further models (*bg19-2a* to *bg19-2f*) include the relative intensity data and explore the influence of regularisation and different constraints of the axial dipole in presence of direct pre-1840 intensity data. Rejecting data with deviation greater than  $5\sigma$  from the current model predictions was found to produce the best quality models. The characteristics of the models are summarised in Table 4.1. Note that spatial and temporal damping parameters  $\lambda_s$  and  $\lambda_t$  are found by inspection. Converged solutions were calculated for a range of choices of the damping parameters. The smoothest model in space and time to a given fit for the data is sought.

For the purposes of comparisons between models a non-dimensional RMS misfit value  $\Delta_{RMS}$  is defined as

$$\Delta_{RMS} = \sqrt{\frac{[\mathbf{d} - \mathbf{g}(\mathbf{m})]^T \mathbf{C}_e^{-1} [\mathbf{d} - \mathbf{g}(\mathbf{m})]}{N}}. \quad (4.1)$$

The normal equations are solved using a quasi-Newton algorithm, thereby assuming that the objective function can be locally approximated as a quadratic in the region around the optimum. As the squared difference between successive model iterates is minimised, a initial model  $\mathbf{m}_0$  is required. In order to obtain a solution and reduce the number of iterations,  $\mathbf{m}_0$  should optimally be sufficiently close to the result. An initial model was constructed by taking the times and positions from all data sets presented in Chapter 2, and replacing the observations by the corresponding predictions by *gufm1*, assigning an uncertainty estimate of 10 nT to the synthetic data.

Model	MC	Relative intensities	axial dipole constraint
<i>bg19-1a</i>	not included	not included	decay fixed at 15 nT/yr
<i>bg19-1b</i>	included	not included	decay fixed at 15 nT/yr
<i>bg19-2a</i>	not included	included	decay fixed at 15 nT/yr
<i>bg19-2b</i>	not included	included	decay fixed at 0 nT/yr
<i>bg19-3a</i>	not included	included	not constrained, $g_1^0(t)$ damped in space and time
<i>bg19-3b</i>	not included	included	not constrained, $g_1^0(t)$ only damped in time
<i>bg19-3c</i>	not included	included	not constrained, $g_1^0(t)$ only damped in space
<i>bg19-3d</i>	not included	included	not constrained, $g_1^0(t)$ undamped

Table 4.1: Summary of the 19th century time-dependent field models constructed in this thesis

## 4.1 19th century models not including relative intensity observations in inversions

General statistical diagnostics are given in Table 4.2.

Parameter	<i>bg19-1a</i>	<i>bg19-1b</i>
Time span	1790–1910	1790–1910
Number of data retained	105,101	180,026
Number of data rejected at $5\sigma$	3,467	6,856
Number of data total	108,568	186,882
Misfit $\Delta_{RMS}$	1.618	1.756
Spatial damping parameter $\lambda_s$ [nT <sup>-2</sup> ]	$4.0 \cdot 10^{-11}$	$4.0 \cdot 10^{-11}$
Temporal damping parameter $\lambda_t$ [nT <sup>-2</sup> yr <sup>4</sup> ]	$5.0 \cdot 10^{-4}$	$5.0 \cdot 10^{-4}$
Spatial norm $\Psi_s$ [nT <sup>2</sup> ]	$1.01 \cdot 10^{12}$	$1.02 \cdot 10^{12}$
Temporal norm $\Psi_t$ [nT <sup>2</sup> yr <sup>-4</sup> ]	$5.28 \cdot 10^4$	$8.56 \cdot 10^4$

Table 4.2: Statistics of the final models *bg19-1a* and *bg19-1b*

### 4.1.1 Basic model without Maury Collection

Figure 4.1 illustrates the change of spatial and temporal complexity with time. It is found that the spatial norm increases very slightly with time (Figure 4.1 (a)), which is probably closely linked to the increasing number of high quality data (see Figure 2.2) proving a higher information content that is expressed as increased model complexity. The temporal complexity, shown in Figure 1.2 (b), exhibits an unphysical decrease at the model endpoints as it tends to zero. Such problems (i.e. increase in spatial complexity with time and decrease of temporal complexity at endpoints) arise from the limited amount of data at certain times. This phenomenon has already been observed in previous studies, see for example Jackson *et al.* [2000].

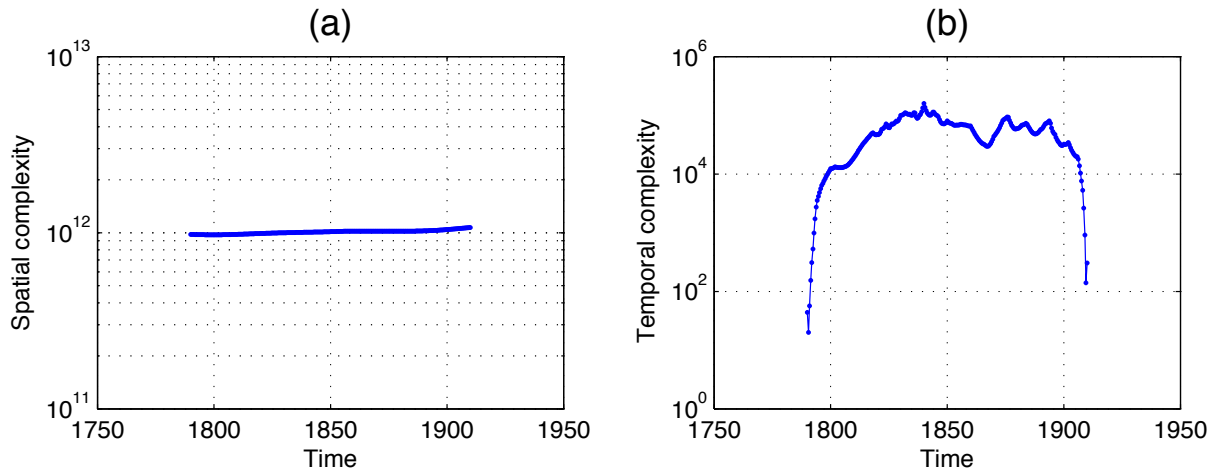


Figure 4.1: (a) Spatial complexity (equation (3.28)) as a function of time, (b) temporal complexity ((3.29)) as a function of time for model *bg19-1b*

Figure 4.3 presents maps of the radial component of the geomagnetic field at the core surface for model *bg19-1b* for the epochs 1790, 1830, 1870 and 1910. The results are in good agreement with those of previous studies, such as Bloxham *et al.* [1989], Bloxham & Jackson [1989], Bloxham & Jackson [1992], Jackson *et al.* [2000] or Jackson *et al.* [2003]. For comparisons a similar nomenclature of the main morphological features of the field is adopted as in Bloxham *et al.* [1989]. Patches marked as N (Normal) refer to such having the same polarity as their vicinity, whereas those marked as R (Reversed) patches have inverted polarity with respect to the surrounding field. These reversed patches are bounded by a null-flux curve. See Figure 4.2 for locations of these features.

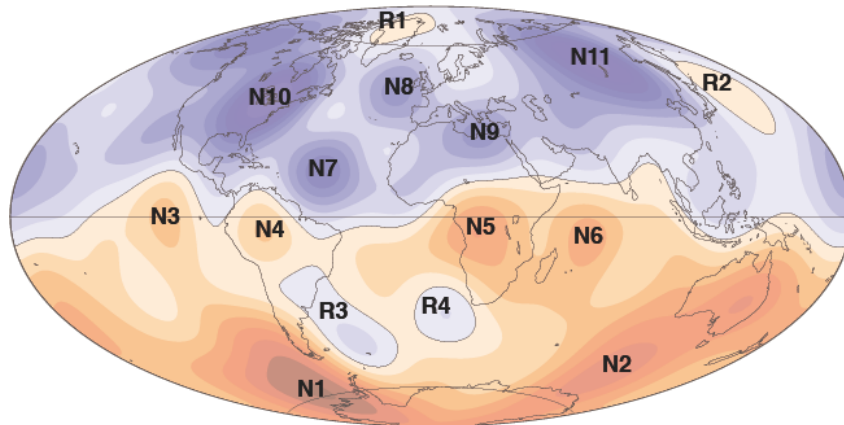


Figure 4.2: Radial geomagnetic field at the core-mantle boundary in 1830 from model *bg19-1b*, with key features of the field: reverse flux patches are labelled R1 – R4, normal flux patches as N1 – N11. Note the colour scheme has been altered to enhance visibility of the labels

(i) *High latitude flux patches*

Four persistent high flux patches are visible throughout the model time span (see Figure 4.3): two patches of high positive flux (N1 and N2) under Antarctica, and two of high negative flux (N10 and N11) under Canada and Siberia. All four patches show high intensity of  $\pm 800$  to

950  $\mu\text{T}$ . These four patches lie nearly symmetrically about the equator. Jackson *et al.* [2000] found these high latitude flux lobes to be mostly unaffected by westward drift over the last 400 years, and a more recent study by Korte & Holme [2010] showed that the flux patches even tend to remain steady over the last 7000 years. These findings strongly suggest these features being linked to underlying dynamo process involving convection columns at 120° W and 120° E [Kono & Roberts, 2002].

(ii) *Dynamic low latitude flux patches*

Highly dynamic flux patches (N3, N4, N5 and N6), which involve strong westward drift, are predominantly confined to an equatorial band ranging from approximately 15° N and 15° S. Average drift rates between  $0.1^\circ\text{yr}^{-1}$  (N4) and  $0.19^\circ\text{yr}^{-1}$  (N6) are observed.

Patch	Long. 1790	Long. 1910	Mean drift rate
N3	115°	120 °	$0.040^\circ\text{yr}^{-1}$
N4	60°	72°	$0.10^\circ\text{yr}^{-1}$
N5	-20°	-3°	$0.14^\circ\text{yr}^{-1}$
N6	-70°	-47°	$0.19^\circ\text{yr}^{-1}$
N7	37°	44°	$0.06^\circ\text{yr}^{-1}$

Table 4.3: Longitudes (negative in western hemisphere) and drift rates of the dynamic secular variation features marked in Figure 4.3. The estimate of the drift rates was obtained by determining the longitude of the point with maximum intensity of each patch

Bloxham *et al.* [1989] found drift rates of up to  $0.22^\circ\text{yr}^{-1}$  (i.e. a westward drift of up to 60° in 265 years), which is in accordance to the drift rates found (see Table 4.4). Westward drift of the patches N7 – N9 appears to be reduced compared N4 – N6. During the model time span, the intensity of N5 and N6 increases continuously, initially 300  $\mu\text{T}$  reaching 600 – 700  $\mu\text{T}$  in 1910. In addition, from 1790 patch N7 drifts slightly westward (with approximately  $0.06^\circ\text{yr}^{-1}$ ) and begins to merge with the high intensity patch N10 in 1850. N8 vanishes in 1880 and patch N9 is rather stationary until in 1860 it begins to take on an elongated form (seen in 1910), which is the onset of a partition of the patch. Generally the westward drift rate in the northern hemisphere appears lower than that in the southern hemisphere.

(iii) *Reversed flux patches*

Reversed flux patches (i.e. reversed with respect to the dominant polarity of the surrounding field) are rather persistent in time: R1, R3 and R4 are present throughout the entire model time, R2 appears in 1797 for the first time. In 1881 patch R3 merges with a minor patch R4 underneath St. Helena with combination complete by 1885, forming the prominent dog-bone shaped patch of reversed flux beneath the southern Atlantic. Note that the change in intensity of patches R1 and R2 is less than 100  $\mu\text{T}$  over the entire period.

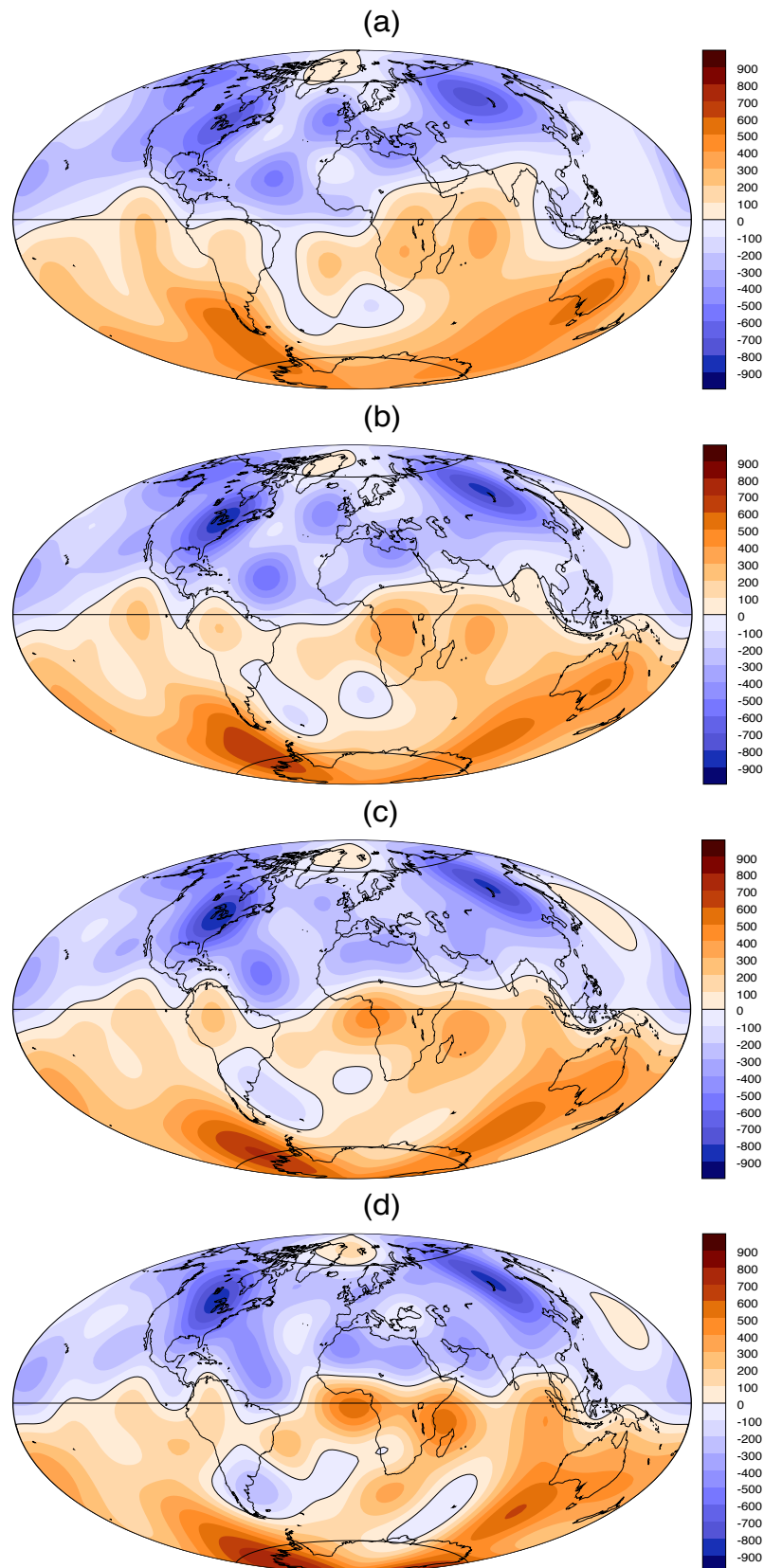


Figure 4.3: Radial geomagnetic field at the core-mantle boundary CMB (Colour interval: 100  $\mu\text{T}$ ) of model *bg19-1b* in Aitoff equal-area map projection, showing also the equator and the tangent cylinder; *red shades*: radial flux out of the core, *blue shades*: radial flux into the core for epochs (c) 1790, (c) 1830, (c) 1870, and (d) 1910

$bg-1a$  also displays a good representation of secular variation over the time period considered. Figure 4.4 illustrates the model compared to the London declination and inclination (Figures 4.4 (a) and (b)) as well as Paris declination and inclination (Figures 4.4 (c) and (d)). Slight deviations from the data occur in particular at the beginning of the time series, which is probably associated with a model endpoint problem during the early period. The overall fit to the inclination data is better than that to the declination, and the overall fit to the Paris data sets is better than that to the London data sets.

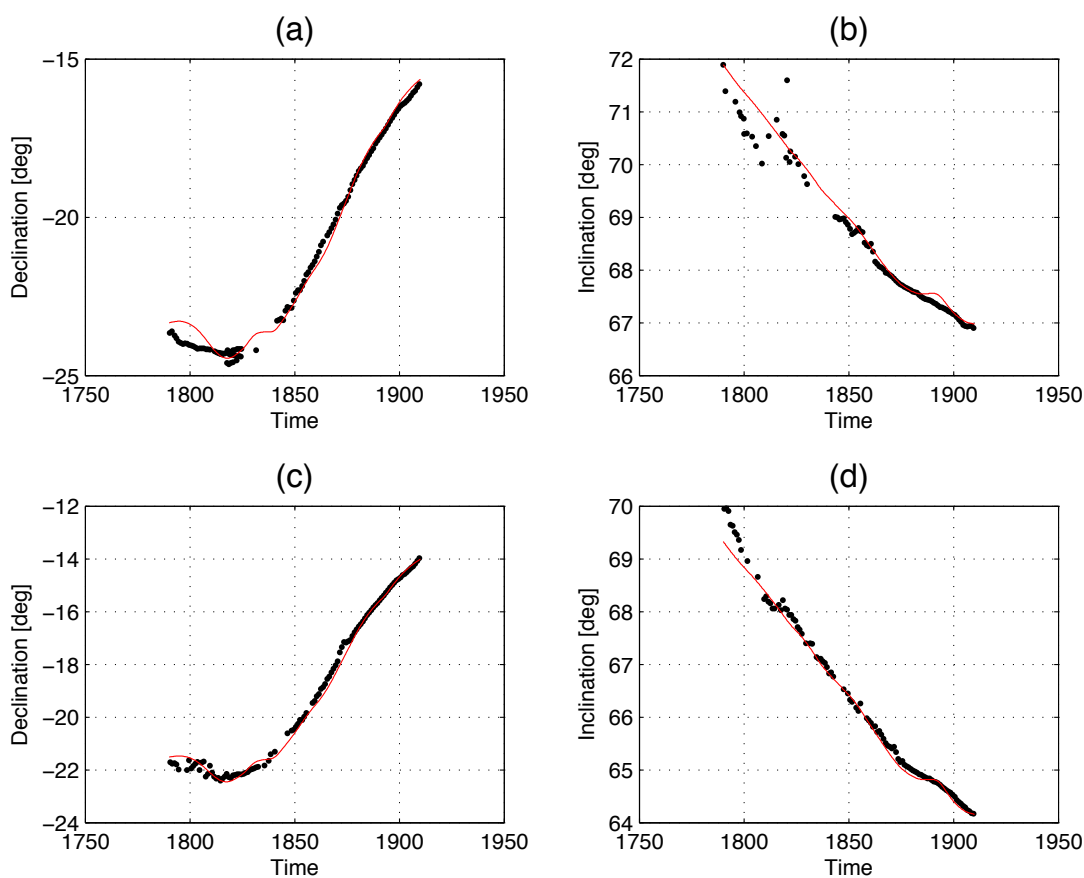


Figure 4.4: Fit of  $bg-1a$  to the London/Paris declination/inclination data sets: (a) London declination, (b) London inclination, (c) Paris declination, and (d) Paris inclination

### 4.1.2 Basic model with Maury Collection

The influence of the Maury Collection (see section 2.1.1.1) on the model is most evident in the representation of secular variation. Data rejection at  $5\sigma$  was applied to all data sets. A comparison of the fits of both *bg19-1a* (not including the MC; red line) and *bg19-1b* (including the MC; green line) to the London and Paris data sets is given in Figure 4.5.

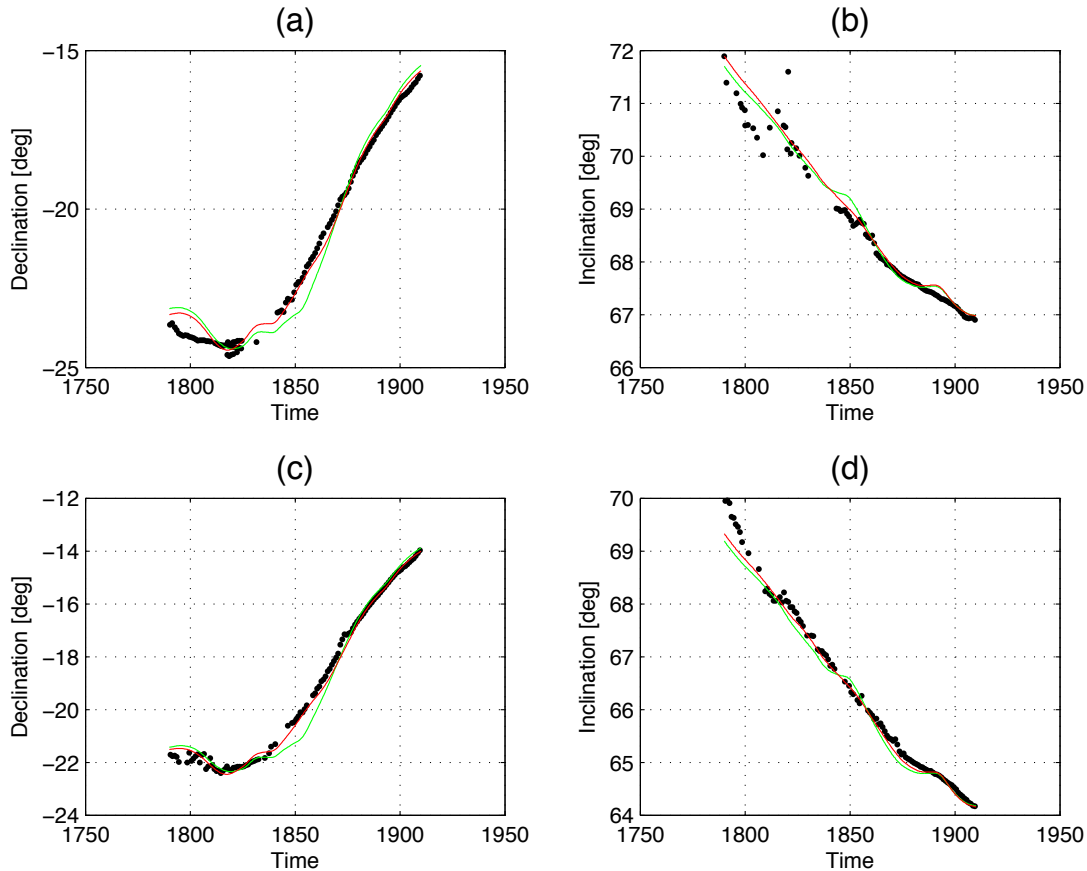


Figure 4.5: Fit of models to the London/Paris declination/inclination data sets: *red*: *bg-1a*, *green*: *bg-1b*. (a) London declination, (b) London inclination, (c) Paris declination, and (d) Paris inclination

Model *bg19-1b* shows a systematic shift of approximately  $0.25^\circ$  in declination (in period 1790 – 1830; Figures 4.5 (a) and (b)) compared to *bg19-1a*. The shift increases gradually, reaching its maximum of 2 degrees around 1855. From 1875 on both models show very similar secular variation. Tests varying the damping parameters were unable to resolve the deviation away from the London and Paris data. This leads to the conclusion that it is a consequence of the Maury data. A comprehensive analysis of the MC is given in section 4.2.

Both models show satisfactory recovery of the temporal variation of inclination in London and Paris (Figures 4.5 (c) and (d)). However, the Maury Collection causes slight aberrance of  $0.25^\circ$  around 1850.

## 4.2 Further analysis of the Maury Collection

### 4.2.1 Comparisons with *gufm1*

The previous findings suggested there may be systematic problems with the Maury Collection so further investigations of this data set were undertaken.

The Maury Collection (MC) is a huge data set spanning the time period 1792 – 1906 and holding 78409 declination observations (for more details concerning data provenance see section 2.1.1.1 (c)). As it has never previously been used in time-dependent geomagnetic field models, thorough analysis will now test its credibility.

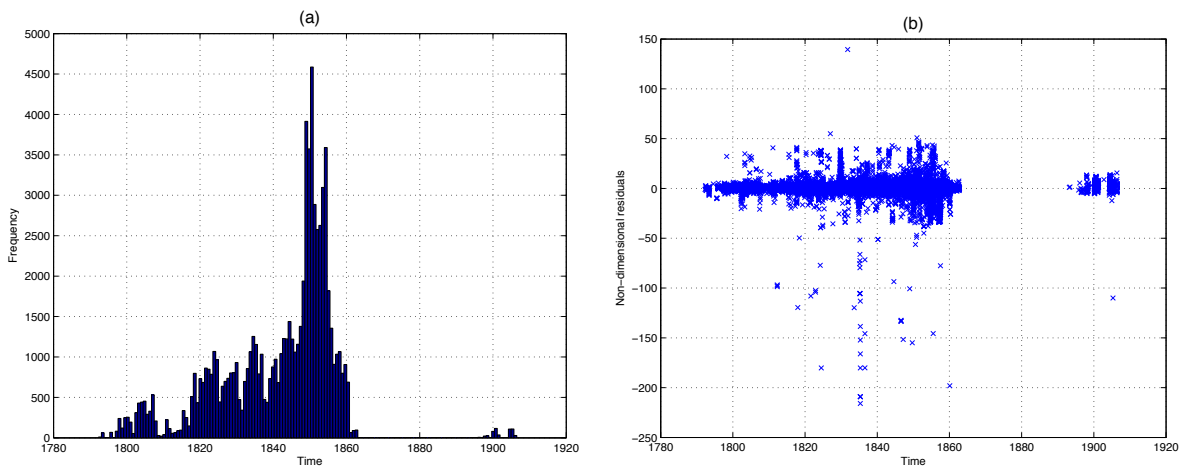


Figure 4.6: Plots showing (a) the temporal data distribution of the complete MC, and (b) the temporal distribution of normalised residuals

The majority of data in the MC originates from the period around 1850 (see Figure 4.6 (a)). Little data is available from 1810 - 1820 and from 1860 on, at the onset of the American civil war, no data are available until 1900. Insight into the underlying statistical data distribution can be gained using residual analysis. The normalised residuals  $r$  are obtained by calculating the difference between an observation  $\gamma^o$  and its corresponding prediction  $\gamma^g$  by *gufm1* (Jackson *et al.* [2000]), normalised by the data error estimate  $\sigma$

$$r = \frac{1}{\sigma}(\gamma^o - \gamma^g), \quad \text{where } \sigma = 2^\circ \quad (4.2)$$

The temporal distribution of normalised residuals (Figure 4.6 (b) and Figures 4.7 (a) – (d)) shows many large residuals (up to  $-220^\circ$  departure from the prediction of *gufm1*). Splitting the residual data up into sub-intervals (Figures 4.7 (a) – (d)) reveals no systematic time-dependent errors. The increasing amount of higher residuals in time of, for example for  $|r| \leq 5$  (Figure 4.7 (a)), is mainly due to the increasing number of data at that time. An other possible explanation could be the usage of iron in shipbuilding, already present in the early 19th century. In fact, many

data originate from American and British warships and are thus likely to produce faulty data, due to the large amount of iron within the construction and weaponry of the ships. Also, the amount of positive and negative residuals are approximately equal, suggesting an overall residual distribution symmetric about  $r = 0$ , which is verified in Figure 4.8 (a). The residual distribution is slightly right-skewed and distinctly non-Gaussian (Figures 4.8 (a) – (d)), suggesting rather a double-exponential probability distribution as the number of data increases.

If the spatial distribution of residuals is split up into subintervals (Figures 4.9 (a) – (d)), it becomes evident that extremely outlying data originate from a few specific voyages. This phenomenon is especially well observed for data with residuals  $|r| < 50$  and  $|r| > 50$  (Figures 4.9 (c) and (d)).

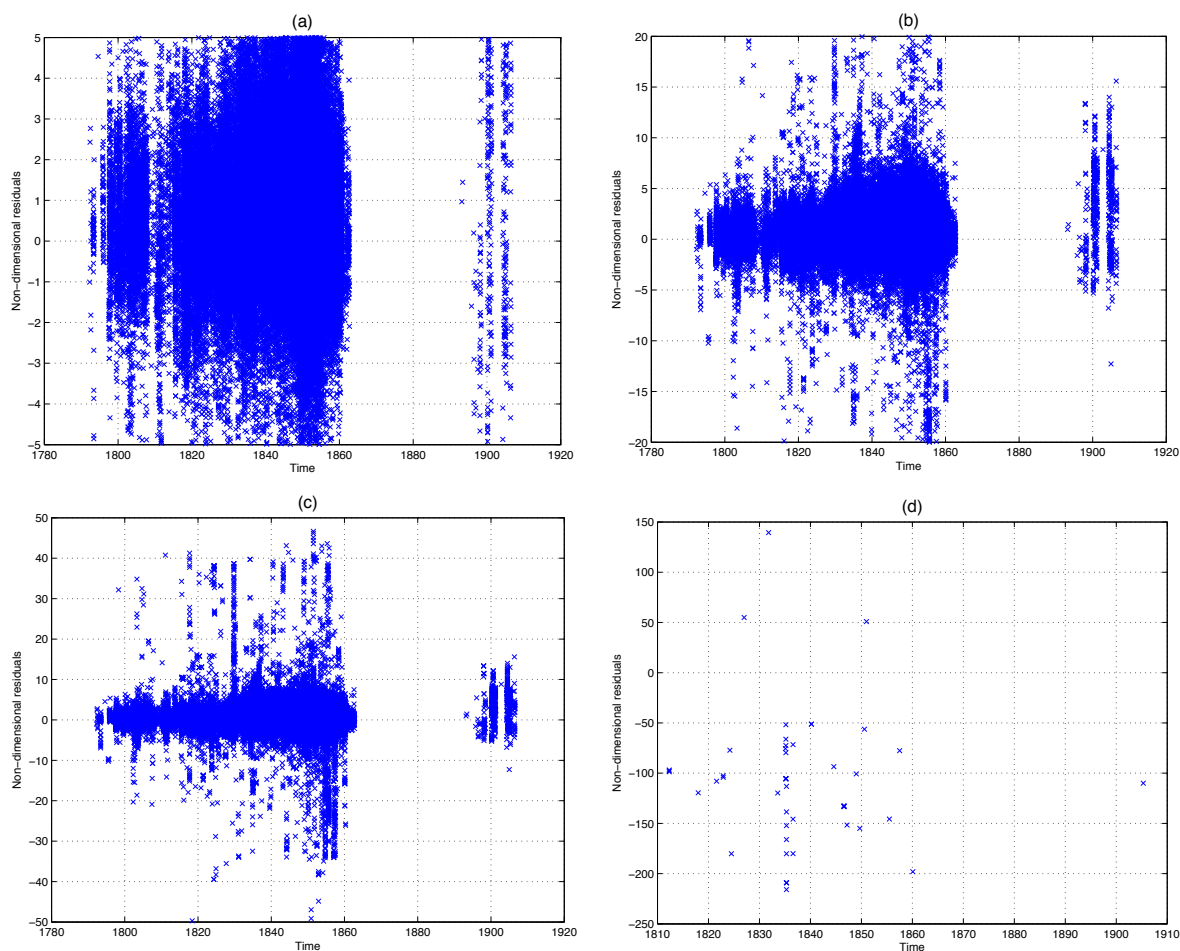


Figure 4.7: Plots showing the temporal distribution of normalised residuals for (a)  $|r| < 5$ , (b)  $|r| < 20$ , (c)  $|r| < 50$ , and (d)  $|r| > 50$

### 4.2.2 Effect of Maury Collection on secular variation time series

Figures 4.5 (a) and (b) show the London declination data, (c) and (d) the London inclination data, compared to the model predictions of *bg19-1a* (not including the MC) and *bg19-1b* (including the MC, rejected at  $5\sigma$ ). Through direct comparison of the two models, the MC is found to be the cause of the considerable deviation from the London declination data, especially between 1840 and 1870 (the most data rich time span in the MC) (Figures 4.6 (a) and (b)). From analysis of residual distribution in space (Figures 4.9 (a) – (d)) it is evident why the MC causes distortions in the model: Great Britain is surrounded by a huge amount of high residual data (most of it of  $|r| < 5$ , but also a considerable amount of data with normalised residuals of up to  $\pm 49$ ). These inaccuracies of the MC declination data around Great Britain adversely effect model predictions for London, apparently reducing the overall quality of the model.

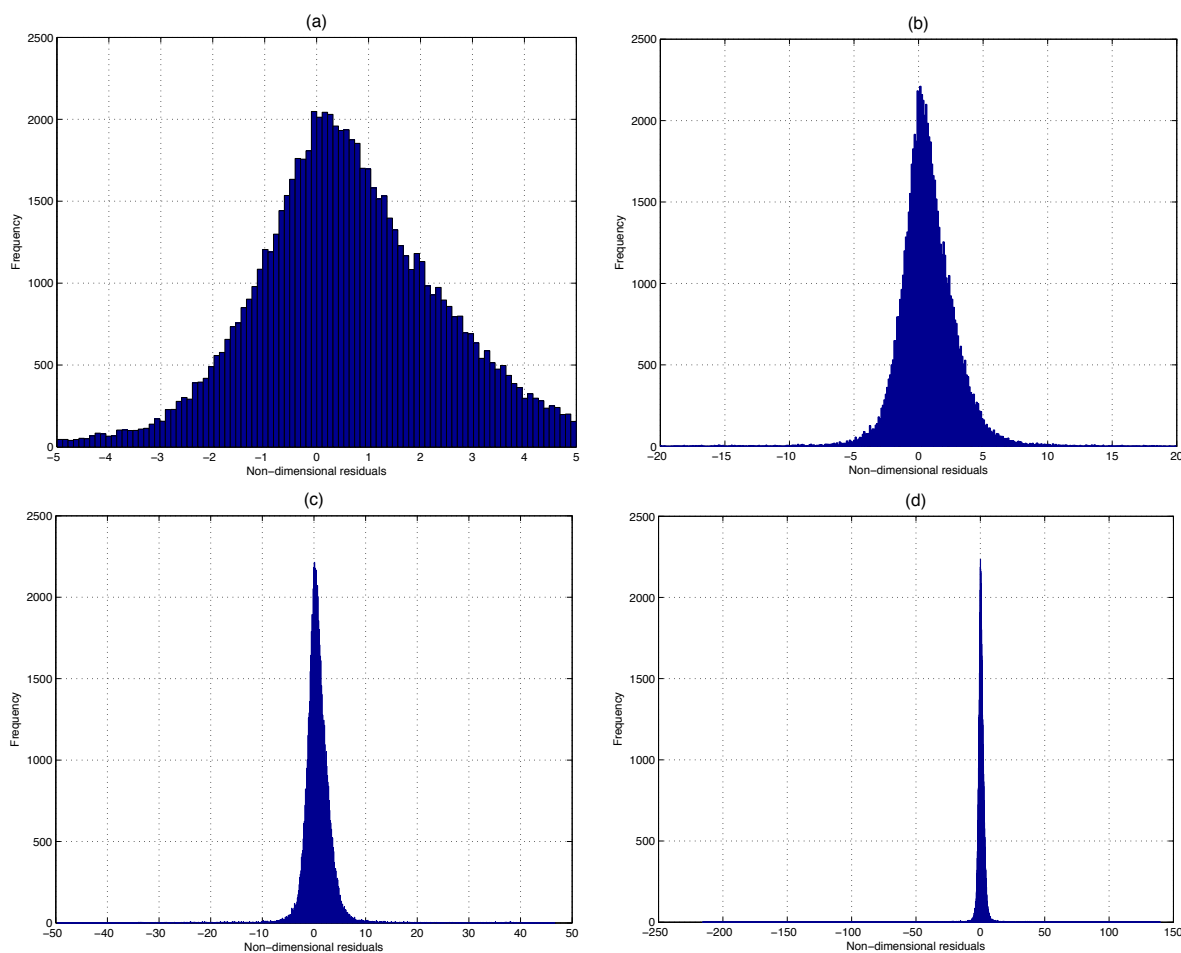


Figure 4.8: Histograms of normalised residuals for (a)  $|r| \leq 5$ , (b)  $|r| \leq 20$ , (c)  $|r| \leq 50$ , and (d) the complete MC

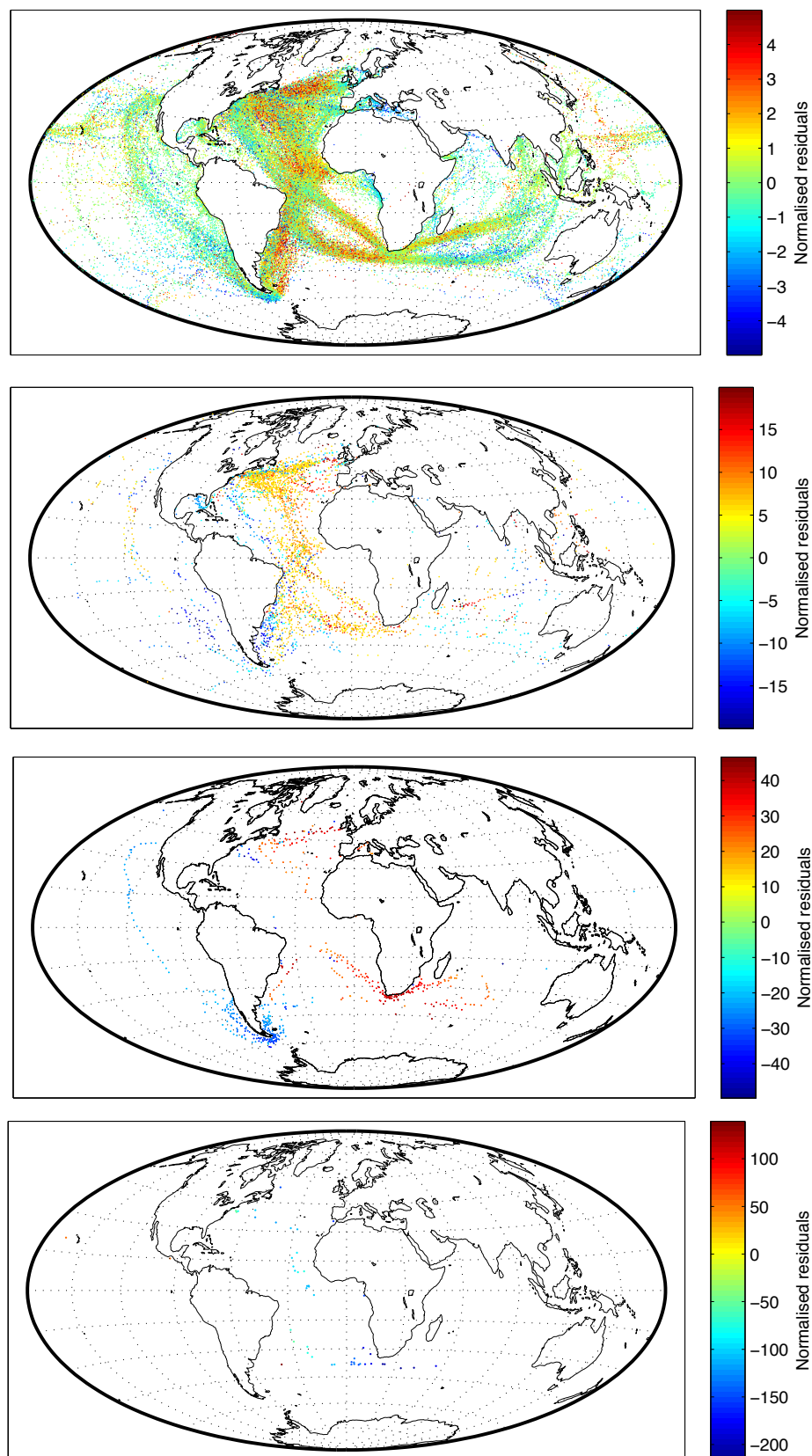


Figure 4.9: Plots showing the spatial distribution of normalised residuals for (a)  $|r| \leq 5$ , (b)  $|r| \leq 20$ , (c)  $|r| \leq 50$  and (d)  $|r| > 50$ . Note that the errors in (c) appear very systematic. An accumulation of negative residuals is found in the Pacific and around South America. In contrast residuals in the Atlantic and around South Africa are mostly positive

### 4.3 19th century models including relative intensity observations in inversions

The new revised modelling code developed as part of this thesis to handle relative intensity data was first tested using synthetic data (i.e.  $H$ ,  $F$ ,  $I$ ,  $D$  and all six relative intensity data types) derived from *gufm1*. In order to ensure optimal spatial and temporal coverage, the data was distributed on a regular  $10^\circ \times 10^\circ$  grid, having a data point every half year. Models with spherical harmonic degrees ranging from 1 to 14, knot spacing of two years and for the short time span 1790 – 1794 derived from model *bg19-1a* have been tested. Results are summarised in Table 4.4. Synthetic truth is well recovered in all test cases, even by only considering a simple spherical harmonic degree one model. In general the obtained model parameters are rather similar for all spherical harmonic degree models, and from degree six model on the differences are marginal.

Degree	CRHF	CRTF	CRTE	CRTL	CRTR	CRTH
1	$0.6252886 \cdot 10^{-4}$	$0.2101046 \cdot 10^{-4}$	$0.2626352 \cdot 10^{-4}$	$0.2836423 \cdot 10^{-4}$	$0.2521269 \cdot 10^{-4}$	$0.2416231 \cdot 10^{-4}$
2	$0.6257983 \cdot 10^{-4}$	$0.2102369 \cdot 10^{-4}$	$0.2628006 \cdot 10^{-4}$	$0.2838206 \cdot 10^{-4}$	$0.2522856 \cdot 10^{-4}$	$0.2417751 \cdot 10^{-4}$
6	$0.6269476 \cdot 10^{-4}$	$0.2107199 \cdot 10^{-4}$	$0.2634043 \cdot 10^{-4}$	$0.2844727 \cdot 10^{-4}$	$0.2528651 \cdot 10^{-4}$	$0.2423305 \cdot 10^{-4}$
10	$0.6269580 \cdot 10^{-4}$	$0.2107190 \cdot 10^{-4}$	$0.2634032 \cdot 10^{-4}$	$0.2844715 \cdot 10^{-4}$	$0.2528640 \cdot 10^{-4}$	$0.2423295 \cdot 10^{-4}$
14	$0.6269581 \cdot 10^{-4}$	$0.2107190 \cdot 10^{-4}$	$0.2634032 \cdot 10^{-4}$	$0.2844715 \cdot 10^{-4}$	$0.2528640 \cdot 10^{-4}$	$0.2423295 \cdot 10^{-4}$
Starting value	$0.5500000 \cdot 10^{-4}$	$0.2200000 \cdot 10^{-4}$	$0.2500000 \cdot 10^{-4}$	$0.2500000 \cdot 10^{-4}$	$0.2500000 \cdot 10^{-4}$	$0.2500000 \cdot 10^{-4}$
Synthetic truth	$0.6270000 \cdot 10^{-4}$	$0.2100000 \cdot 10^{-4}$	$0.2630000 \cdot 10^{-4}$	$0.2840000 \cdot 10^{-4}$	$0.2520000 \cdot 10^{-4}$	$0.2420000 \cdot 10^{-4}$

Table 4.4: Results of synthetic tests exploring difference in obtained model parameters while increasing the spherical harmonic degree of the model from 1 to 14 derived from model *bg19-1a*. Also listed are the starting values and synthetic truth for reasons of comparison

#### 4.3.1 Models with linear constraint on the evolution of $g_1^0(t)$

The axial dipole of the models constructed in this section are constrained to the linear decay given by equation

$$g_1^0(t) = g_1^0(t) + \beta(t - 1840). \quad (4.3)$$

Figure 4.10 presents the evolution of  $g_1^0(t)$  for the field models *bg19-2a* ( $\beta = 15$  nT/yr) and *bg19-2b* ( $\beta = 0$  nT/yr). For reasons of comparison the axial dipole from *gufm1* ( $\beta = 15$  nT/yr, Jackson *et al.* [2000]) and *gufm1-g10c* ( $\beta = 0$  nT/yr, Finlay [2008]) are also shown. The models show good agreement with the models from previous studies (e.g. *gufm1* or *gufm1-g10c*), slightly deviating from *gufm1* in 1875 and 1860.

A rather prominent feature showing up in both *bg19-2a* and *bg19-2b* is the bump around 1845, more pronounced in *bg19-2a*. This characteristic is very weakly present and is not so obvious in the models by Jackson *et al.* [2000] or Finlay [2008].

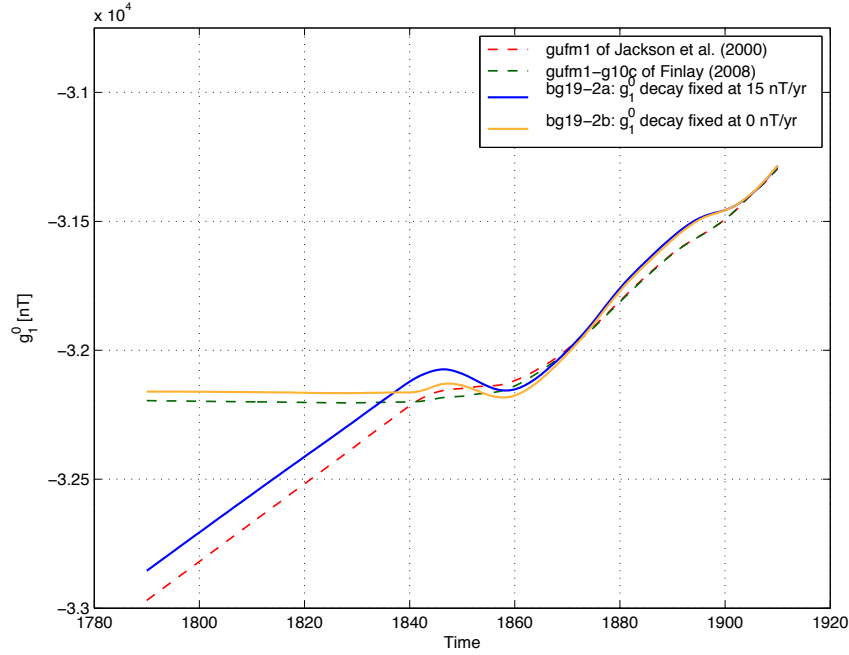


Figure 4.10: Examples of  $g_1^0(t)$  from two field models ( $bg19-2a$  and  $bg19-2b$ ) constructed with the linear constraint given by equation (4.3). For reference  $gufm1$  ( $\beta = 15$  nT/yr, Jackson *et al.* [2000]) and  $gufm1-g10c$  ( $\beta = 0$  nT/yr, Finlay [2008]) are presented

In both models  $bg19-2a$  and  $bg19-2b$  a systematic shift to a less intense axial dipole is observed starting from the bump in 1845 (compare  $bg19-2a$  and  $gufm1$ , and  $bg19-2a$  and  $gufm1-g10c$ , respectively). This effect is more evident in the relative intensity model with  $\beta = 15$  nT/yr.

### 4.3.2 Models without linear constraint on the evolution of $g_1^0(t)$

In a next step models were constructed without constraining the pre-1840 history of  $g_1^0(t)$  by equation (4.3), i.e. allowing the axial dipole to evolve freely. These models were constructed in order to answer the question to what extent physically plausible models can be obtained from relative intensity data pre-1840 and various types of regularisation (see section 3.2.2).

Four models with differently regularised dipole moments  $g_1^0(t)$  are built (model setups are summarised in Table 4.1). Using the possibilities of either spatial and/or temporal regularisation result in four model scenarios:

- (i) spatial and temporal regularisation applied to  $g_1^0(t)$  (model  $bg19-3a$ )
- (ii) no spatial regularisation of  $g_1^0(t)$  but including temporal regularisation (model  $bg19-3b$ )
- (iii) no temporal regularisation of  $g_1^0(t)$  but including spatial regularisation (model  $bg19-3c$ )
- (iv) applying no regularisation to  $g_1^0(t)$  at all (model  $bg19-3d$ ).

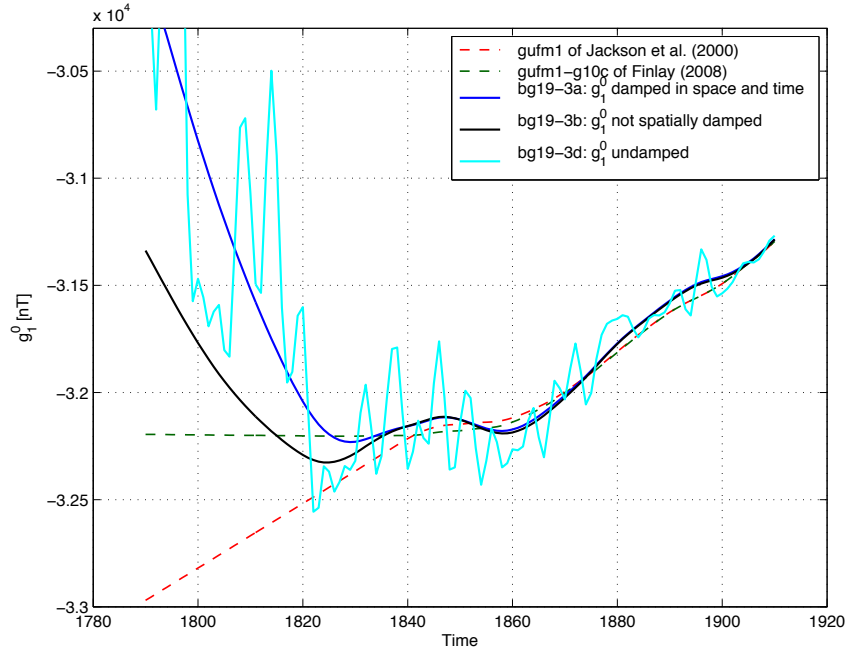


Figure 4.11: Examples of  $g_1^0(t)$  from four field models ( $bg19-2a$ ,  $bg19-2b$ ,  $bg19-2c$  and  $bg19-2d$ ) constructed without the linear constraint. For reference  $gufm1$  ( $\beta = 15$  nT/yr, Jackson *et al.* [2000]) and  $gufm1-g10c$  ( $\beta = 0$  nT/yr, Finlay [2008]) are presented

The results for  $g_1^0(t)$  obtained from the inversions together with  $gufm1$  ( $\beta = 15$  nT/yr) as a reference are illustrated in Figure 4.11. A feature all four models have in common is an unphysical decrease starting between 1825 and 1830. This behaviour points directly to the difficulty leaving  $g_1^0(t)$  unconstrained: it arises from the fact that the model is only weakly constrained by the relative intensity data due to their large error estimates and limited number of data. Thus these models are almost completely controlled by spatial and temporal regularisation before 1820.

Model  $bg19-3d$ , having no damping of  $g_1^0(t)$  in space and time, shows many short timescale oscillations between 1840 and 1910, probably due to unmodelled external field variations. Approaching the start of the model, the oscillation's amplitudes increase eventually reaching finally unrealistically high values. Excluding temporal damping (model  $bg19-3c$ ) causes nearly identical short timescale oscillations between 1840 and 1910 as found in the undamped model. However, the dipole moment values in  $bg19-3c$  is also systematically shifted upwards if compared to the undamped model. The post-1840 period for a temporally undamped model yields physically more plausible models, but the rapid decay remains.

Models  $bg19-3a$  and  $bg19-3b$  show good agreement with the pre-1840 dipole history of  $gufm1$ . A prominent decrease for times prior to 1825/30 is present in both models, but reduced in  $bg19-3b$  for which there was no spatial damping of  $g_1^0(t)$ . Furthermore, decadal oscillations about  $gufm1-g10c$  as well as the bump at 1845, also previously identified in the dipole constrained models  $bg19-3a$  and  $bg19-3b$ , are also observed in these new models, corroborating the supposition of them being a feature required by the data rather than an artifact.

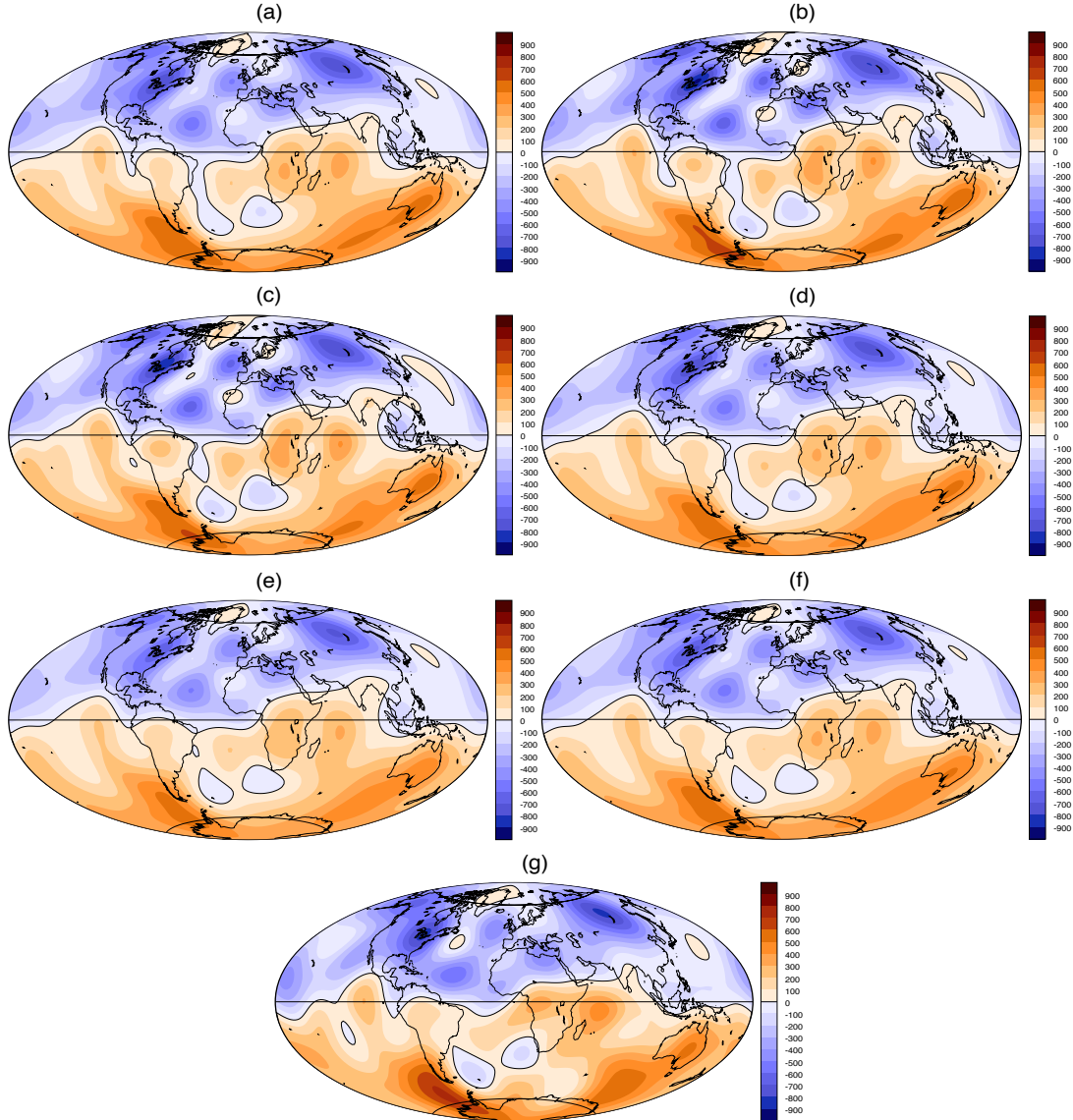


Figure 4.12: Radial geomagnetic field at the core-mantle boundary CMB in 1800 (Colour interval:  $100 \mu\text{T}$ ) in Aitoff equal-area map projection of (a) *bg19-2a* ( $g_1^0(t)$ ) linearly constrained with  $\beta = 15 \text{ nT/yr}$ , (b) *bg19-2b* ( $g_1^0(t)$ ) linearly constrained with  $\beta = 0 \text{ nT/yr}$ , (c) *bg19-3a* ( $g_1^0(t)$ ) not constrained and damped in space and time, (d) *bg19-3b* ( $g_1^0(t)$ ) not constrained and undamped in space), (e) *bg19-3c* ( $g_1^0(t)$ ) not constrained and undamped in time), (f) *bg19-3d* ( $g_1^0(t)$ ) not constrained and undamped in space and time), (g) *gufm1* ( $g_1^0(t)$ ) linearly constrained with  $\beta = 15 \text{ nT/yr}$ )

In Figure 4.12 the field morphology at the core-mantle boundary in 1800 for the models presented in sections 4.3.1 and 4.3.2 are shown along with *gufm1* for comparison. The differences between the different models are rather small. Forcing the axial dipole to remain constant between 1790 and 1840 leads to a generally higher model complexity, apparent in the increased number of reversed flux patches and amplitudes of the field features, especially in the northern hemisphere and the flux lobe under Antarctica (cf. Figures 4.12 (a) and (b)). Not constraining

the axial dipole moment, however, decreases the amplitude and gradient of the non-dipole features (cf. Figures 4.12 (c) and (f)) in the equatorial region. This is a consequence of the rapid decay of  $g_1^0(t)$  prior to 1840 observed in Figure 4.11. In addition, reduction of damping of  $g_1^0(t)$  leads to a decreased number of reversed flux patches, due to reduced model complexity.

### 4.3.3 Comparison of models to data sets included in inversions

In Table 4.5 the misfit of the models presented in the two previous sections to the relative intensity data sets involved in the inversions are presented. No data rejection was applied to the relative intensity data. The historical data sets, however, were rejected at  $5\sigma$ . The misfits obtained from the inversions using *gufm1* together with the relative intensity model parameters (cf. equations (1.5) and (3.38)) given in Jonkers *et al.* [2003] are listed for reference.

Model	Misfit global	Misfit pre-1840	Misfit RHF	Misfit RTF	Misfit RTE	Misfit RTL	Misfit RTR	Misfit RTH
<i>bg19-2a</i>	1.5832	2.8916	11.8693	1.6191	2.0834	3.9358	1.9285	1.7254
<i>bg19-2b</i>	1.4868	2.8678	11.8301	1.5625	2.1227	3.8431	1.6963	1.7289
<i>bg19-3a</i>	1.5373	2.8758	11.8505	1.4969	2.1178	3.9392	1.4161	1.6860
<i>bg19-3b</i>	1.4576	2.8603	11.8544	1.5377	2.0807	3.9373	1.7006	1.7296
<i>bg19-3c</i>	1.4148	2.8245	11.7733	1.5588	2.0921	3.7728	0.8616	1.7184
<i>bg19-3d</i>	1.4304	2.8003	11.7930	1.4967	2.0974	3.7727	1.0612	1.6638
<i>gufm1</i>	1.253	3.7528	12.6087	1.9854	4.5046	4.0645	20.1092	2.8017

Table 4.5:  $L_2$  misfits between the model predictions and data sets: Global misfits, misfits to all relative intensity data sets take together (denoted pre-1840 above) and misfits to each relative intensity data set. The misfits obtained from *gufm1* with additional model parameters as given in Jonkers *et al.* [2003] are listed for comparison. Note that no data rejection was applied to the relative intensity data sets

The RHF data set shows a systematically high misfit in all models and the misfits to the RTL data set are also somewhat elevated compared to the other data sets.

*bg19-3d* shows the best fit to the pre-1840 data and *bg19-2b* fits both the historical as well as the relative intensity data sets better than *bg19-2a*. Considering models *bg19-3b* and *bg19-3c* it is evident that excluding temporal damping yields smaller misfits than excluding spatial damping. However, model *bg19-3c* suffers from unrealistic short timescale oscillations over the entire modelling period. Not constraining but damping the axial dipole component in space and time yields misfits similar to those of the linearly constrained model with  $\beta = 15$  nT (*bg19-2a*).

## Chapter 5

# Discussion and Conclusions

In this concluding chapter the findings of the thesis are discussed and interpretations offered. Conclusions will be drawn with respect to the thesis aims presented in the introduction. Perspectives for future work are also given.

### 5.1 New 19th century field models

The construction of new dedicated models *bg19-1a* and *bg19-1b* of geomagnetic secular variation for the interval 1790 – 1910 involved five data sets not previously been used in any published study. These data sets are the long declination and inclination time series from London and Paris (see section 2.1.1.2), as well as the Maury Collection (MC) (see section 2.1.1.1, a large data set comprising over 78000 declination observations not yet used in any published study on geomagnetic field modelling.

Model	Misfit
<i>bg19-1a</i>	1.618
<i>bg19-1b</i>	1.756
<i>gufm1</i> (Jackson <i>et al.</i> [2000])	1.255

Table 5.1: Comparison of misfits of models *bg19-1a* and *bg19-1b* with the previous *gufm1* model of Jackson *et al.* [2000]

*bg19-1a* and *bg19-1b* show good agreement with previous models (see Table 5.1). Nevertheless, it was not found possible to decrease the misfit to unity. This is at least partly due to overly

optimistic error assignments and to the fact that the models obtained in this study are rather smoother in space than e.g. *gufm1*, yielding a slightly higher misfit.

Unfortunately the MC causes to declination predictions of *bg19-1b* to deviate by up to 2 degrees in London (Figure 4.5). In addition, the core-surface morphology reveals a higher number of reversed flux patches than found in models such as *bg19-1a* or *gufm1*. This is a result of increased model complexity apparently necessary to fit the Maury data sufficiently. The origin of the problems lies in the provenance of the data, originating from brigs, schooners, steamers, warships and whalers (listed in the order of the number of observations reported). All of these ships carried a great amount iron on board, which is known to lead to problems related to biased declination readings. An additional source of inaccurate data may be declination data reported in ‘points’ instead of degrees and minutes. These readings were typically taken at the ship’s main (not portable) compass, which had the full circle divided into 32 points, thus one point is corresponding to  $11.25^\circ$ . The precision is given up to tenths of a point, corresponding to  $1.125^\circ$  [NOAA, 1998]. As a consequence of such limitations, one output of this thesis is the recommendation not to include the full MC in future field models. Thus the preferred 19th century model derived in this thesis (before use of relative intensity data sets) is model *bg19-1a*.

Could anything be done to avoid discarding the entire MC data set? One possibility would be not to include the entire data set, but to select data according to their location filling only areas with hitherto poor data coverage (e.g. the Pacific). Figure 4.8 also shows a distinct departure from the assumed normal distribution towards to a double exponential distribution of errors. This observation coincides with the findings of Jackson *et al.* [2000] and Walker & Jackson [2000]; Minimisation of an  $L_1$ -norm measure of misfit should thus be considered rather than the use of the  $L_2$ -norm for handling this data set.

Alexandrescu *et al.* [1997] previously demonstrated that the London and Paris data sets are of high quality and resolution. This is confirmed by independent tests against *gufm1*, making them ideal sources for time-dependent modelling as they accurately capture secular variation. The London data sets have been used previously as a diagnostic in Jackson *et al.* [2000], but did not enter the inversion because of the possibility of error correlation due to the crustal magnetic field (cf. Jackson *et al.* [2000]). Due to the fact that the 19th century observations do not originate from one observatory only but, for example in case of London, from over 15 different sites (all within a radius of 36 km) [Malin & Bullard, 1982], the problem of correlated crustal errors may not be as crucial as previously thought. In this thesis, the data sets are simply

included without any further data processing accounting for the possibility of error correlation due to the crustal magnetic. As shown in Table 5.2, the London and Paris data are fit very well by both models *bg19-1a* and *gufm1*.

Data set	Misfit of model <i>bg19-1a</i>	Misfit of model <i>gufm1</i>
London declination	0.7329	0.3290
London inclination	0.7582	0.6853
Paris declination	0.6465	0.3051
Paris inclination	0.7432	0.4937

Table 5.2:  $L_2$  misfits between the London/Paris declination/inclination data sets and model predictions of *bg19-1a* and *gufm1* (Jackson *et al.* [2000])

A more elegant solution would be to rewrite the unbiased declination  $\tilde{D}$  as a sum of the observation  $D_o$  and an additional term  $D_c$  describing the influence of the crustal field:

$$\tilde{D} = D_o + D_c. \quad (5.1)$$

The free parameter  $D_c$  could then be obtained during the inversion using a technique very similar to that developed in this thesis for handling relative intensity data. Note that  $X$ ,  $Y$  and  $Z$  data obtained from the Greenwich observatory also appears in the data set `oams_2011.dif`. Unfortunately, this was only realised after carrying out the inversions. However, the impact on the field models of this double use of the data will likely be small. Future studies should use the approach discussed above for  $D$ ,  $I$  (and  $F$  - Barraclough *et al.* [2000]) and remove the duplicate  $X$ ,  $Y$ ,  $Z$  data set.

As mentioned previously in section 2.1.1.3, the original expedition data of the `Vaq_Af1880_jb.dat` data set is relative horizontal intensity. However, Vaquero & Trigo [2006] have converted the relative horizontal intensities to absolute horizontal intensities. Unfortunately, this was only realised as the inversion had already been carried out. A more accurate way would be to include the original (relative) data in the inversion using the theory developed in this thesis.

## 5.2 Inclusion of relative intensity observations

### 5.2.1 Data sets

In order to find the source of the systematic error biasing the RHF data set a test was performed, assuming the data given in the RHF data set is relative total rather than relative horizontal intensity (as stated in Jonkers *et al.* [2003]). A new set of ratios was calculated according to equations (2.4) and (2.5) and the intensity type of  $R_g$  was changed accordingly. The results of the test are shown in Figure 5.1. The linear trend of the new data obtained (green circles) strongly suggests that the RHF data set contains relative total rather than relative horizontal intensity data. This conclusion is corroborated by the histogram of the new residuals (green), showing a peak frequency around zero, and the misfits from models *bg19-2b* and *bg19-3b* (see Table 5.3).

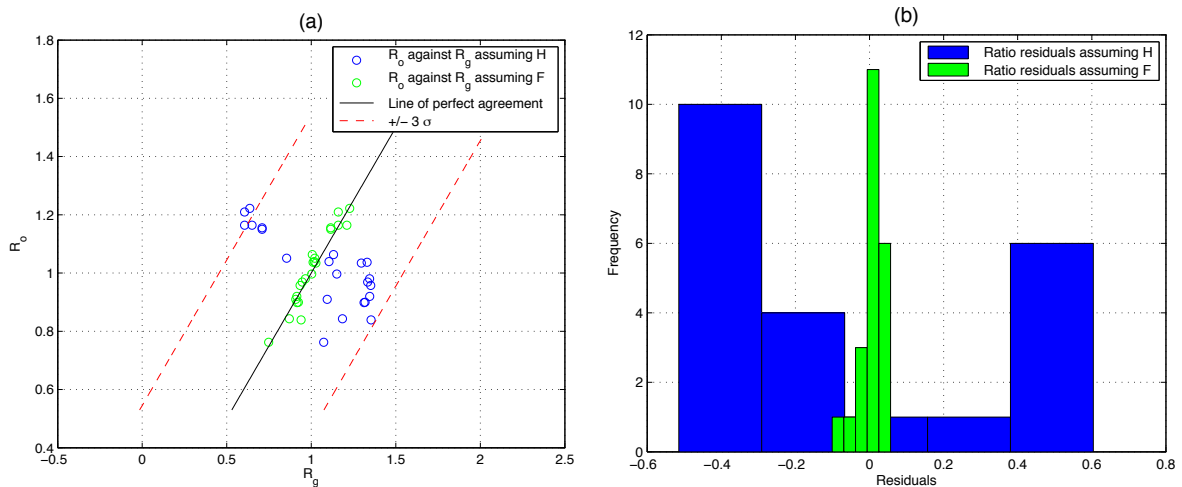


Figure 5.1: (a) Comparison of fits between the ratios obtained from the RHF data set and *gufm1* (i) assuming the data in the RHF data set is horizontal intensity (blue circles) and (ii) assuming the data in the RHF data set is total intensity (blue circles), (b) Histogram of residuals for both assumptions

Model	Misfit assuming relative $H$	Misfit assuming relative $F$
<i>bg19-2b</i>	11.8301	1.5064
<i>bg19-3b</i>	11.8511	1.5241

Table 5.3: Misfits between the model predictions of *bg19-2b* and *bg19-3b* and the RHF data set, making (i) the assumption of relative  $H$  and (ii) the assumption of relative  $F$  data

All models including relative intensity data show a misfit to the RTL data set which is approximately twice the misfit to the other relative intensity data sets (with exception of the

‘old’ RHF data set, assuming relative horizontal data). Partly the higher misfit of the RTL data set is the result of the measurement location in the Antarctic region where the intensity gradient increases rapidly, thereby exacerbating accurate measurements. Perhaps the higher misfits are also associated with a violation of the assumption according to which the proportionality factor  $\alpha_k$  (relating relative to absolute intensity) is time-independent. Sabine [1872] re-evaluated the British Unit (an absolute unit) on average every seven years (cf. Sabine [1872], p.354 or Jonkers *et al.* [2003]) and mentions that the reference location for the (relative) London unit was not constant throughout time. It is thus likely that a time-dependent scaling factor  $\alpha_k$  for the RTL data set yields smaller misfits.

### 5.2.2 Comparisons to previous models of $g_1^0(t)$

Based on the global and pre-1840 misfits (cf. Table 4.5) the favoured model with a linear constraint on the axial dipole component is model *bg19-2b*, involving no change of  $g_1^0(t)$  (i.e.  $\beta = 0$  nT/yr) prior to 1840. Although simpler than *bg19-2a* (i.e.  $\beta = 15$  nT/yr) it fits both the relative intensity as well as an independent archeointensity data set better. This finding is consistent with the results obtained by Finlay [2008] (model *gufm1-g10c*,  $\beta = 0$  nT/yr), who selected the preferred model on the basis of Bayesian model comparison analysis [Finlay, 2008]. However, there are some differences, e.g. a prominent decadal oscillation (1880 – 1890), the bump around 1845, as well as the rapid decay of the axial dipole starting in 1825. These features are most present in models *bg19-3a* ( $g_1^0(t)$  not constrained; spatial and temporal regularisation applied to  $g_1^0(t)$ ) and *bg19-3b* ( $g_1^0(t)$  not constrained; no spatial regularisation of  $g_1^0(t)$  but including temporal regularisation). As the models presented in this thesis have lower spatial and temporal norms (i.e. are smoother) than e.g. *gufm1* or *gufm1-g10c* this feature is believed to be required by the data.

Figure 5.2 presents a figure from section 4.3.2 together with a zoom-in of the period 1820 – 1860. It shows that models *bg19-3a* and *bg19-3b* coincide until 1840 and the decay in amplitude of model *bg19-3a* with  $g_1^0(t)$  damped in space and time already starts in 1830. The evolution of model *bg19-3b* appears trustworthy until perhaps 1825. Prior to this it shows an unrealistically rapid decay of the axial dipole that was previously found in similar a test without dipole constraint by Finlay [2008]. To some extent this decay is associated with an endpoint problem. In general there is always a problem at the end points because of the lack of data before and after the first and last knot points. Thus the second time derivative at those points cannot be

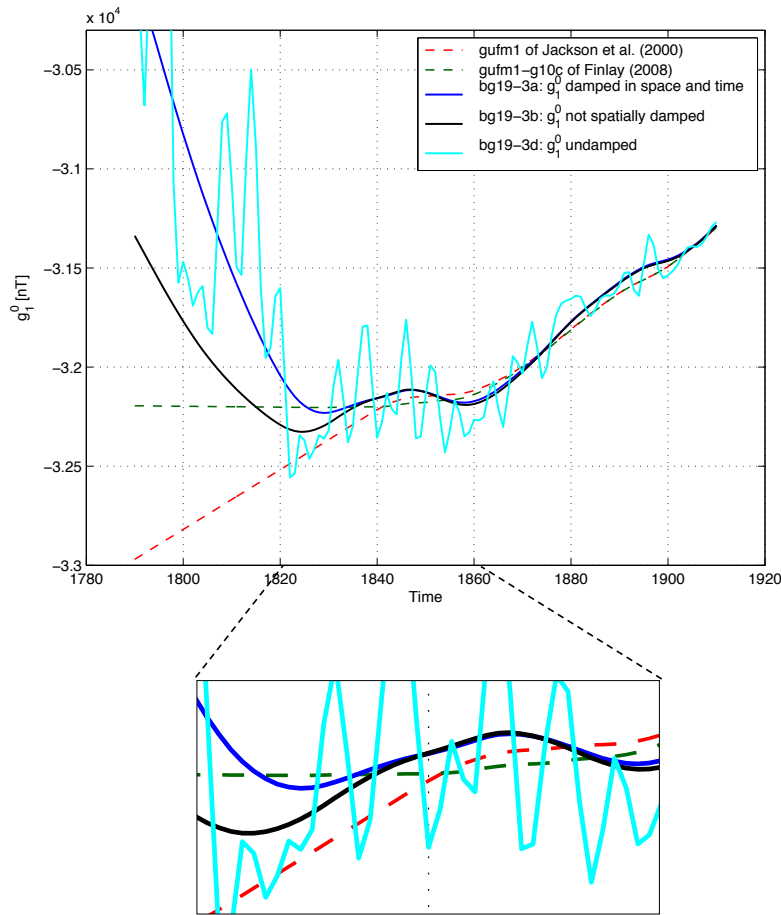


Figure 5.2: Evolution of  $g_1^0(t)$  shown for models *bg19-3a*, *bg19-3b* and *bg19-3d* along with *gufm1* and *gufm1-g10c*. Also is a zoom-in of the time span 1820 – 1860 presented, showing detailed  $g_1^0(t)$  evolutions in this critical period

well determined from the data alone. If (as is the case in 1790) there are also few data at this time, the problem is exacerbated. Model *bg19-3c* (no temporal damping of  $g_1^0(t)$ ) is unacceptable as it clearly exhibits short timescale oscillations and an unphysical temporal evolution of the model. As the differences in space between the models are rather minor (see Figure 4.12) it is concluded that the spatial damping of  $g_1^0(t)$  is not crucial for producing plausible models. Similar oscillatory behaviour was found by Finlay [2008] as the influence of artificially overweighted archeointensity data was examined.

The preferred derived in this thesis using relative intensity data without axial dipole constraint is thus *bg19-3b* (i.e. the model without spatial damping of  $g_1^0(t)$ ). A comparison of the axial dipole components obtained from the preferred models *bg19-2b* and *bg19-3b* is presented in Figure 5.3.

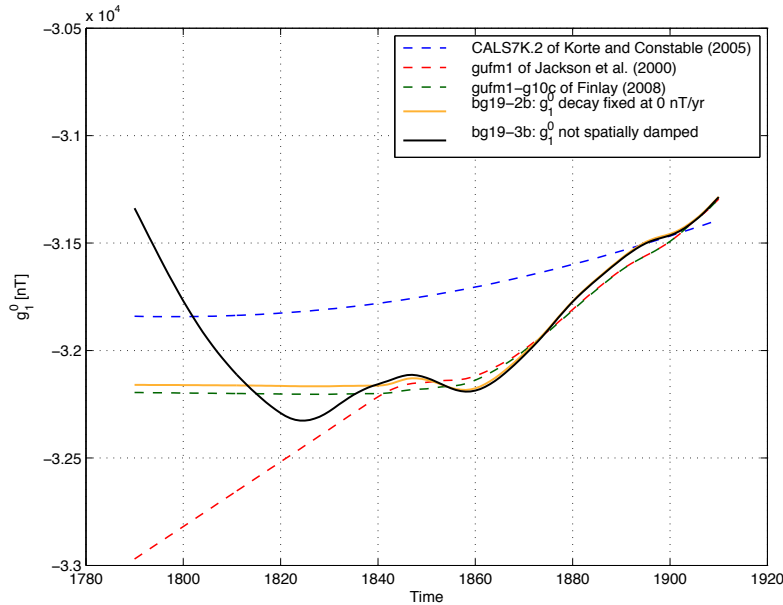


Figure 5.3: Summary showing the axial dipole evolution of the two preferred models in this thesis *bg19-2b* and *bg19-3b* together with examples of  $g_1^0(t)$  obtained from models by Jackson *et al.* [2000], Korte & Constable [2005a] and Finlay [2008]

### 5.2.3 Comparison with the independent archeomagnetic data set of Donadini *et al.* [2006]

The obtained models including the relative intensity data sets in the inversions were tested against an independent archeointensity data set from the database of Donadini *et al.* [2006], selecting only data with very accurate dating. Unfortunately only very few high quality archeointensity data are available in the time of interest (1790 – 1910). The data set form a time series spanning 1795 – 1836 comprising eleven observations located in Turkey. Despite these limitations, the data set provides a good and independent test of the relative success of the models. Note that all archeointensity data are included in the comparisons.

	<i>bg19-2a</i>	<i>bg19-2b</i>	<i>bg19-3a</i>	<i>bg19-3b</i>	<i>bg19-3c</i>	<i>bg19-3d</i>
Misfit:	3.5474	3.5195	3.4856	3.5330	3.5363	3.5588

Table 5.4:  $L_2$  misfits between the model predictions and the independent archeomagnetic data from Donadini *et al.* [2006]. Note that no data rejection was applied to the archeomagnetic intensity data

The misfits between the models presented and archeointensity data are listed in Table 5.4. An illustration of the model fit to the time series is given in Figure 5.4. The intensity evolution

of the linearly constrained models  $bg19-2a$  and  $bg19-2b$  is rather similar to that represented by  $gufm1$ . However, the model having  $\beta = 0$  nT fits the archeointensity data best.

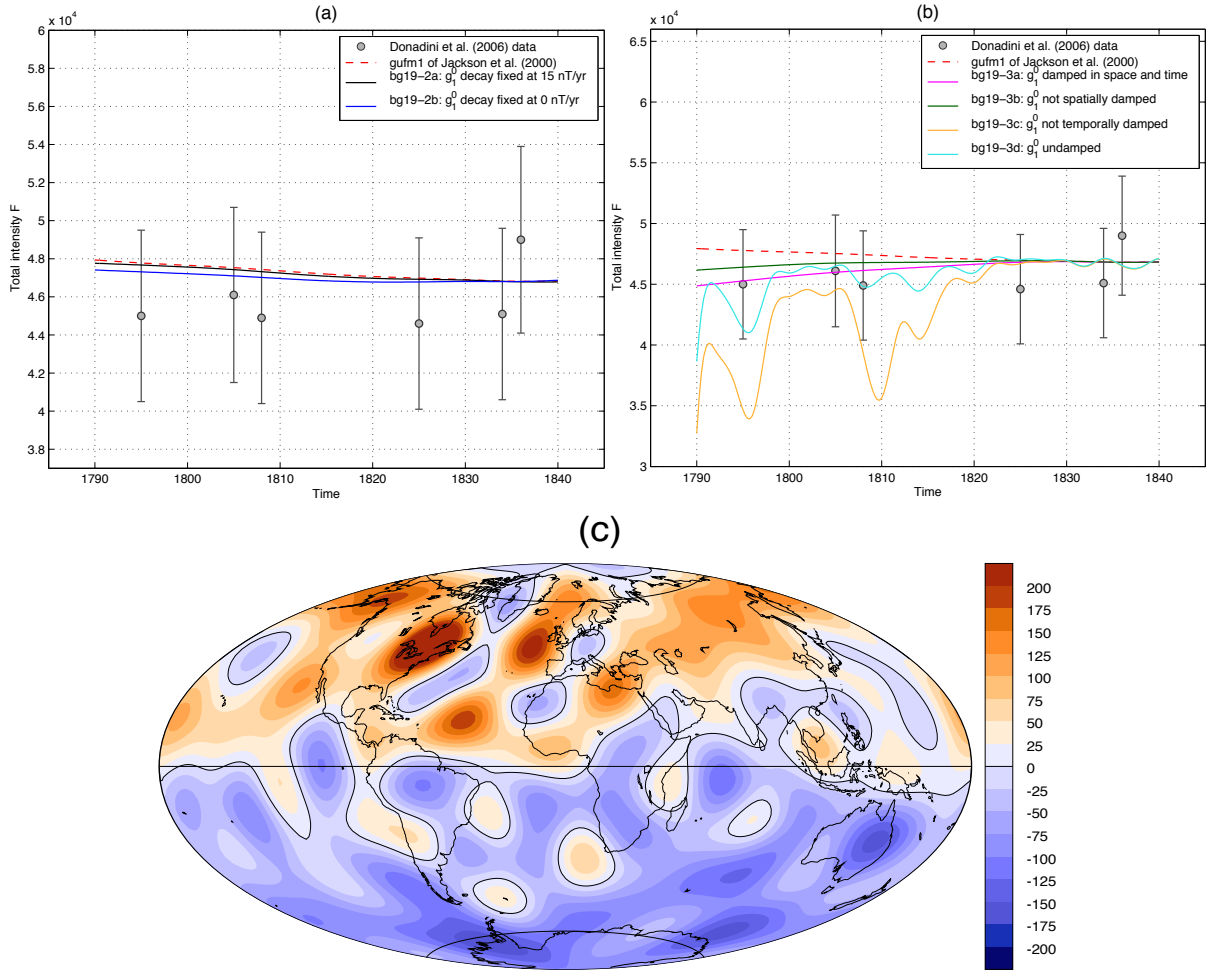


Figure 5.4: Fit of the models including relative intensity observations to the independent archeointensity data set derived from Donadini *et al.* [2006] (grey dots) together with  $gufm1$  (red dashed line), which is shown as a reference. (a) shows the intensity evolution of the linearly constrained models  $bg19-2a$  and  $bg19-2b$ , (b) shows the intensity evolution of the unconstrained models  $bg19-3a$ ,  $bg19-3b$ ,  $bg19-3c$  and  $bg19-3d$ , (c) Residual radial magnetic field at the core surface in 1795 of models  $bg19-3a$  and  $bg19-3c$  as calculated by equation (5.2)

The best fit among the models without linear constraint on the axial dipole is obtained from the model having  $g_1^0(t)$  damped in space and time. Surprisingly, the misfits of models  $bg19-3b$  and  $bg19-3c$  are almost identical, yet  $bg19-3c$  shows high amplitude oscillations throughout the modelling period. Omitting damping of  $g_1^0(t)$  (model  $bg19-3d$ ) yields an intensity evolution similar to that of  $bg19-3c$  but systematically shifted to higher intensities.

The model predictions for the 1795 archeointensity data point of the best-fitting ( $bg19-3a$ ) and least-fitting ( $bg19-3c$ ) model differ by more than 11,000 nT (see Figure 5.4 (b)). A contour

plot of the difference  $\Delta\mathbf{m}(t_i)$  between the models *bg19-3a* and *bg19-3c* is shown in Figure 5.4 (c). The residual geomagnetic field is calculated using the relation

$$\Delta\mathbf{m}(t_i) = \mathbf{m}^{bg19-3a}(t_i) - \mathbf{m}^{bg19-3c}(t_i) \quad (5.2)$$

where  $\mathbf{m}^{bg19-3a}$  and  $\mathbf{m}^{bg19-3c}$  are single epoch models evaluated at  $t_i$ . The plot of the residual field reveals a structural difference in the region of Turkey, indicated by the orange patch in Figure 5.4 (c) for the considered epoch. This patch, previously referred to as N9 (see Figure 4.2) shows positive residual indicating higher field intensity of the *bg19-3a* compared to *bg19-3c*.

### 5.3 Conclusions

With respect to the set aims of the thesis presented in the introductory chapter, the following conclusions are drawn:

**(i) Derivation of a time-dependent model of the 19th century of the geomagnetic field at the core surface**

Sensible models for the 19th century were obtained fitting the data satisfactorily and with reasonable spatial and temporal complexity.

**(ii) Assessment of the Maury Collection for time-dependent field modelling**

The full Maury Collection should not be used for time-dependent geomagnetic field modelling. Instead, a subset should be selected according to its location, filling areas of presently poor data coverage. Further, the distribution of normalised residuals shows a distinct double exponential distribution. Thus the minimisation of an  $L_1$ -norm should be considered rather than an  $L_2$ -norm.

**(iii) Collation and quality control of relative intensity data sets**

In total six relative intensity data sets (comprising a total of 777 data) have been collated and undertaken a thorough quality control. The data are of good quality with misfits comparable to those from previously collated historical data. It was found that the RHF data set contains relative total intensities instead of relative horizontal intensities (as stated in Jonkers *et al.* [2003]). Therefore the RHF data should be treated as relative total intensities.

**(iv) Development of a theory for using relative intensity data for time-dependent field modelling**

A simple theory for handling relative intensity involving an additional scaling factor for each

data set was developed. The time-dependent field modelling code and its matrix storage were modified accordingly and successfully tested.

**(v) Derivation of a time-dependent model of the 19th century of the geomagnetic field at the core surface including the relative intensity data sets**

Models were obtained with various types of constraints and damping of  $g_1^0(t)$ . Without the axial dipole constraint an unrealistically rapid decrease in  $g_1^0(t)$  between 1790 and 1825.

**(vi) Assessment of the merits of the two hypothesis concerning the rate of change of the axial dipole prior to 1840: (i) 15 nT/yr, (ii) 0 nT/yr** The model involving no change of the axial dipole (i.e.  $\beta = 0$  nT/yr) fits the relative intensity data sets and archeointensity data between 1790 and 1840 better than the model with  $\beta = 15$  nT/yr, favouring the former hypothesis.

## 5.4 Recommendations for future historical field models

The inclusion of relative intensity observations is recommended upon the results obtained in this thesis. However, it was shown that the RHF data set comprises relative total intensity data and should thus be added to the RTF data set. The RTL data set shows signs of time-dependent errors, presumably to change(s) of reference location. The implementation of a time-dependent scaling factor, relating relative to absolute intensity, is recommended.

The data currently in the Vaq\_Af1880\_jb.dat data set (as given Vaquero & Trigo [2006]) should not be used. Instead it would be beneficial to use the original (relative) data together with the theory developed in this thesis.

Further analysis of the Maury Collection (preferably on a voyage-by-voyage basis) is required in order to identify systematic biases in the data. Residual analysis of declination data measured in ‘points’ is required as these are likely to be rather inaccurate. Perhaps a subset of the Maury Collection should be selected according to its location in order to fill areas of currently poor data coverage.

# Bibliography

- Alexandrescu, M., Courtillot, V. & Le Mouél, J.-L. (1996). Geo- magnetic field direction in paris since the mid-sixteenth century,. *Phys. of the Earth and Plan. Int.* **98**, 321–360.
- Alexandrescu, M., Courtillot, V. & Le Mouel, J.-L. (1997). High-resolution secular variation of the geomagnetic field in western europe over the last 4 centuries: Comparison and integration of the historical data from paris and london. *J. Geophys. Res.* **102**(B9), 20,245 – 20,258.
- Backus, G. & Gilbert, F. (1970). Uniqueness in the inversion of inaccurate gross Earth data. *Philos. Trans. R. Soc. London Ser. A* **266**, 123–192.
- Backus, G., Parker, R. & Constable, C. (1996). *Foundations of geomagnetism*. Cambridge Univeristy Press.
- Barraclough, D. (1974). Spherical harmonic analyses of the geomagnetic field in eight epochs between 1600 and 1910. *Geophys. J. R. astr. Soc.* **36**, 497–513.
- Barraclough, D., Carrigan, J. & Malin, S. (2000). Observed geomagnetic field intensity in London since 1820. *Geophys. J. Int.* **141**, 83–99.
- Becquerel, H. (1840). *Traité experimental de l’électricité et du magnétisme*, vol. 6. Fermin Didot Frères.
- Bloxham, J. (1986). Models of the magnetic field at the core-mantle boundary for 1715, 1777 and 1842. *J. Geophys. Rev.* **91**, 13954–13966.
- Bloxham, J. & Gubbins, D. (1985). The secular variation of Earth’s magnetic field. *Nature* **317**(777-781).
- Bloxham, J., Gubbins, D. & Jackson, A. (1989). Geomagnetic secular variation. *Philos. Trans. R. Soc. London Ser. A* **329**, 415–502.
- Bloxham, J. & Jackson, A. (1989). Simultaneous stochastic inversion for geomagnetic main field and secular variation II. 1820-1980. *J. Geophys. Res.* **94**, 15753–15769.
- Bloxham, J. & Jackson, A. (1992). Time-Dependent Mapping of the Magnetic Field at the Core-Mantle Boundary. *J. Geophys. Res.* **97**, 19537–19563.
- Brekke, A. & Egeland, A. (2000). *History of Geophysics*. American Geophysical Union, Washington.
- Campbell, R. (2009). The Voyage of HMS Erebus and HMS Terror to the Southern and Antarctic Regions. *The Journal of the Hakluyt Society* .
- De Boor, C. (1972). On Calculating with B-Splines. *Journal of Approximation Theory* **6**, 50–62.

- De Rossel, E. (1808). *Voyage de d'entrecasteaux, envoye à la recherche de La Pérouse*, vol. 2. de l'imprimerie imperiale, Paris.
- Donadini, F., Korhonen, K., Riisager, P. & Pesonen, L. (2006). Database for Holocene geomagnetic intensity information. *EOS. Trans. American Geophys. Union* **14**(87).
- Erman, G. A. (1835). *Reise um die Erde durch Nord-Asien und die beiden Oceane in den Jahren 1828, 1829 und 1830 ausgef"uhrt von A. Erman, Abteilung I: Historischer Bericht*, vol. 1-3. G. Reimer, Berlin.
- Erman, G. A. (1841). *Reise um die Erde durch Nord-Asien und die beiden Oceane in den Jahren 1828, 1829 und 1830 ausgef"uhrt von A. Erman, Abteilung 2: Physikalische Beobachtungen*. G. Reimer, Berlin.
- Finlay, C. (2008). Historical variation of the geomagnetic axial dipole. *Phys. of the Earth and Plan. Int.* **170**, 1–14.
- Fitzroy, R. (1839). *Narrative of the Surveying Voyages of HMS Adventure and Beagle, Between the Years 1826 and 1836, Describing Their Examination of the Southern Shores of South America, and the Beagle's Circumnavigation of the Globe*. Henry Colburn, London.
- Garland, G. (1979). The Contributions of Carl Friedrich Gauss to Gomagnetism. *Historia Mathematica* **6**, 5–29.
- Gellibrand, W. (1635). *A discourse mathematical of the variation of the magneticall needle together with its admirable diminution lately discovered*. London.
- Gubbins, D., Jones, A. L. & Finlay, C. (2006). Fall in Earth's Magnetic Field Is Erratic. *Science* **312**(12).
- Halley, E. (1693). An account of the cause of the change of the variation of the magnetic needle, with an hypothesis of the structure of the internal parts of the Earth. *Philos. Trans. R. Soc. London Ser. A* **29**, 406–428.
- Halley, E. (1701). *General Chart of the Variation of the Compass*. London.
- Hansteen, C. & Due, L. (1863). *Resultate magnetischer, astronomischer und meteorologischer Beobachtungen auf einer Reise nach dem östlichen Sibirien in den Jahren 1828 - 1830. Gleichzeitige Beobachtungen von Dr. Erman nach Kamtschatkan, v. Georg Fuss nach Peking, und v. Baron Ferd. Wangel und Lieut. Anjon in dem nordöstl. Sibirien und auf dem Eismeere in den Jahren 1821 - 1823 beigefügt*. Gesellschaft der Wissenschaften zu Christiania.
- Holme, R. & Jackson, A. (1997). The cause and treatment of anisotropic errors in geomagnetism. *Phys. of the Earth and Plan. Int.* **103**, 375–388.
- Hulot, G., Khokhlov, A. & Le Mouél, J.-L. (1997). Uniqueness of maily dipolar magnetic fields recovered from directional data. *Geophys. J. Int.* **129**, 347–354.
- Jackson, A., Jonkers, A., Mande, M. & Murray, A. (2003). Earth's magnetic field in the early 19th century from French sources. *Geochemistry, Geophysics, Geosystems* **4**(7), 1–12.
- Jackson, A., Jonkers, A. & Walker, M. (2000). Four centuries of geomagnetic secular variation from historical records. *Phil. Trans.: Math., Phys. and Eng. Sc.* **358**(1768), 957–990.
- Jonkers, A., Jackson, A. & Murray, A. (2003). Four centuries of geomagnetic secular variation from historical records. *Rev. Geophys.* **41**(2).

- King, E. K. (2010). *Variations in the intensity of the Geomagnetic field in the early 19th Century: Analysis of data and field modelling*. Master's thesis, University of Liverpool, Department of Earth and Ocean Sciences.
- Kono, M. & Roberts, P. (2002). Recent geodynamo simulations and observations of the geomagnetic field. *Rev. Geophys.* **40**(4).
- Korte, M. & Constable, C. (2005a). Continuous geomagnetic field models for the past 7 millennia. 2. cal5k. *Geochemistry, Geophysics, Geosystems* **6**.
- Korte, M. & Holme, R. (2010). On the persistence of geomagnetic flux lobes in global Holocene field models. *Phys. of the Earth and Plan. Int.* **182**, 179–186.
- Malin, S. (1982). Sesquicentenary of Gauss' first measurement of the absolute value of magnetic intensity. *Phil. Trans.: Math., Phys. and Eng. Sc.* **306**, 5–8.
- Malin, S. & Barraclough, D. (1991). Humboldt and the Earth's magnetic field. *Q. Jl. R. astr. Soc.* **32**, 279–293.
- Malin, S. & Bullard, E. (1982). The direction of the Earth's Magnetic Field at London, 1570–1975. *Philos. Trans. R. Soc. London Ser. A* **299**(1450), 357–423.
- Maus, S., Silva, L. & Hulot, G. (2008). Can core-surface flow models be used to improve the forecast of the Earth's main magnetic field. *J. Geophys. Res.* **113**.
- Needham, J. (1962). *Science and Civilisation in China*, vol. 4. Cambridge University Press.
- NOAA (1998). *The Maury Collection: Global Ship Observations 1792-1911*. NOAA (National Oceanic Atmospheric Administration), National Climate Data Center, Asheville, NC, USA.
- Parker, R. (1994). *Geophysical inverse Theory*. Princeton University Press.
- Press, W., Teukolsky, S., Vetterling, W. & Flannery, B. (2007). *Numerical Recipes - The Art of Scientific Computing*. Cambridge University Press.
- Roberts, P. & Scott, S. (1965). On the analysis of the secular variation — 1 : A hydromagnetic constraint. *J. Geomagn. Geoelectr.* **17**(2), 137–151.
- Sabine, E. (1827). Experiments to ascertain the ratio of the magnetic forces acting on a needle suspended horizontally, in Paris and in London. *Philos. Trans. R. Soc. London* **1**(118), 1–14.
- Sabine, E. (1838). Contributions to terrestrial magnetism. *Philos. Trans. R. Soc. London* , 43–62.
- Sabine, E. (1840). Contributions to terrestrial magnetism. *Philos. Trans. R. Soc. London* **1**, 129–155.
- Sabine, E. (1843). Contributions to terrestrial magnetism. *Philos. Trans. R. Soc. London* **5**, 145–231.
- Sabine, E. (1846). Contributions to terrestrial magnetism. *Philos. Trans. R. Soc. London* **8**, 337–432.
- Sabine, E. (1849). Contributions to terrestrial magnetism. *Philos. Trans. R. Soc. London* **9**, 173–249.

- Sabine, E. (1872). Contributions to terrestrial magnetism. *Philos. Trans. R. Soc. London* **13**, 353–433.
- Sabine, E. (1875). Contributions to terrestrial magnetism. *Philos. Trans. R. Soc. London* **14**, 161–203.
- Sabine, E. (1877). Contributions to terrestrial magnetism. *Philos. Trans. R. Soc. London* **15**, 461–508.
- Vaillant, A. N. (1840 - 1852). *Voyage autour du monde exécuté pendant les années 1836 et 1837 sur la corvette La Bonite (commandée par M. Vaillant)*. A. Bertrand, Paris.
- Vaquero, J. & Trigo, R. (2006). Results of geomagnetic observations in Central Africa by Portuguese explorers during 1877–1885. *Phys. of the Earth and Plan. Int.* **157**, 8–15.
- von Humboldt, A. (1850). *Relation historique du voyage aux régions équinoxiales du Nouveau Continent - Wuellen und Forschungen zur Geschichte der Geographie und der Reisen*, vol. 1,2 of pp. 259, 516, 613 (Vol. 1), pp. 619-614 (Vol. 2). H. Beck.
- von Humboldt, A. (1858). *Kosmos - Entwurf einer physischen Weltbeschreibung*, vol. 4. I. G. Gotta'scher Verlag, Stuttgart/Augsburg.
- Walker, E. (1866). *Terrestrial and Cosmical Magnetism: The Adams Prize Essay for 1865*. Deighton and Bell, London.
- Walker, E. & Jackson, A. (2000). Robust modelling of the earth's magnetic field. *Geophys. J. Int.* **143**, 799–808.